Respiratory Self-Navigation for Whole-Heart Coronary Magnetic Resonance Imaging

Atmungs-Selbstnavigation für die koronare Magnetresonanzbildgebung des gesamten Herzens

Der Technischen Fakultät
der Friedrich-Alexander-Universität
Erlangen-Nürnberg

zur

Erlangung des Doktorgrades Dr.-Ing.

vorgelegt von

Davide Piccini
aus
Thiene (Vicenza, Italy)

Als Dissertation genehmigt
von der Technischen Fakultät
der Friedrich-Alexander-Universität Erlangen-Nürnberg

Tag der mündlichen Prüfung:	23.06.2014
Vorsitzende des Promotionsorgans:	Prof. Dr.-Ing. habil. M. Merklein
Gutachter:	Prof. Dr.-Ing. J. Hornegger
	Prof. Dr. M. Stuber

A Paula, con amore.

Abstract

As the average life span of the world population increases, cardiovascular diseases firmly establish themselves as the most frequent cause of death in many of the developed countries. Coronary artery disease (CAD) is responsible for more than half of these cases and there is, hence, a strong need for a non-invasive and radiation-free test that could be reliably adopted for its assessment in clinical routine. Although coronary magnetic resonance imaging (MRI) has always been regarded with high expectations, it is still not considered for clinical assessment of CAD. This is mainly due to several limitations of current coronary MRI examinations. The complex anatomy of the coronary arteries requires extensive scout-scanning to precisely plan the actual data acquisition. The current speed limitations of the MRI scanners and the contribution of cardiac and respiratory motion do not allow the high resolution acquisitions to be performed within the fraction of a single heartbeat. Consequently, data acquisition must be split into multiple heartbeats and usually performed during free-breathing. At the same time, gating with respect to a consistent respiratory position is applied using an interleaved navigated scan which monitors the position of the subject's diaphragm.

Major improvements in standard navigator-gated free-breathing coronary MRI have been achieved in recent years, but a number of important intrinsic limitations, such as the prolonged and unknown acquisition times, the non-linearity of the motion compensation, and the complexity of the examination setup have so far hindered the clinical usage of this technique. In contrast, a technique known as self-navigation, which performs motion detection and correction solely based on imaging data of the heart, promises a priori knowledge of the duration of the acquisition with improved accuracy of the motion compensation and requires minimal expertise for the planning of the examination.

In this work, a novel acquisition and motion correction strategy for free-breathing self-navigated whole-heart coronary MRA was introduced, analyzed and implemented to be entirely integrated in a clinical MR scanner. The proposed acquisition method consists of a novel interleaved 3D radial trajectory, mathematically constructed on the basis of a spiral phyllotaxis pattern, which intrinsically minimizes the eddy currents artifacts of the balanced steady state free-precessing acquisition, while ensuring a complete and uniform coverage of k-space. The self-navigated respiratory motion detection is performed on imaging readouts oriented along the superior-inferior axes and is based on a method for the isolation and automatic segmentation of the bright signal of the blood pool. Motion detection of the segmented blood pool is then performed using a cross-correlation technique. This fully automated respiratory self-navigated method offers an easy and robust solution for coronary MR imaging that can also be integrated into a regular clinical routine examination. The technique was tested in volunteers, compared to the standard navigator-gating approach, and, for the first time to the author's knowledge, allowed self-navigation to be positively applied to a large patient study in an advanced clinical setting.

Kurzfassung

Im Zuge des Anstiegs der durchschnittlichen Lebenserwartung der Weltbevölkerung sind kardiovaskuläre Krankenheiten heute in vielen der entwickelten Länder zur häufigsten Todesursache geworden. Koronare Gefäßerkrankungen sind dabei die Ursache für mehr als die Hälfte dieser Todesfälle. Es besteht deshalb ein großer Bedarf an Diagnosetechniken, die nichtinvasiv und ohne Einsatz ionisierender Strahlung zuverlässig in die klinische Routine eingebunden werden können. Obwohl der koronaren Magnetresonanztomographie (MRT) seit langem hohe Erwartungen entgegengebracht werden, wird sie nach wie vor nicht zur klinischen Bewertung koronarer Gefäßerkrankungen eingesetzt. Die Gründe dafür sind vielfältig, rühren jedoch vor allem von verschiedenen technischen Unzulänglichkeiten derzeitiger koronarer MRT-Untersuchungen. Die komplexe Anatomie der Koronararterien bedarf vieler Voraufnahmen zur präzisen Planung der eigentlichen Untersuchung. Zudem behindern die Bildgebungsgeschwindigkeit heutiger MRT-Scanner in Verbindung mit den Herz- und Atmungsbewegungen die Aufnahme hochaufgelöster Bilder innerhalb eines Herzschlags. Deshalb mußdie Datenakquisition über mehrere Herzschläge verteilt und typischerweise wegen ihrer Dauer auch bei freier Atmung durchgeführt werden. Während der eigentlichen Bildaufnahme wird immer wieder ein sehr schnelles Navigatorbild akquiriert, aus dem die Position des Diaphragmas und damit die Atmungsphase bestimmt werden kann. Im Zuge eines nachgeordneten "Gatings" werden dann nur die Bildinformationen einer bestimmten Atemposition zur Weiterverarbeitung genutzt.
Die Techniken zur navigatorgestützten Aufnahme koronarer MRT-Bilder bei freiem Atmen haben in den letzten Jahren wesentliche Verbesserungen erfahren. Allerdings haben die ihnen immanenten Einschränkungen wie die wesentlich erhöhte und zudem im Vorhinein unbekannte Aufnahmezeit, die Nichtlinearität der Bewegungskompensation, sowie die Komplexität der Untersuchung eine klinische Nutzung bisher verhindert. Im Gegensatz dazu versprechen die sogenannten Selbstnavigations-Methoden, die Bewegungsdetektion und -korrektur ausschließlich anhand der aufgenommenen Herzbilddaten ausführen, eine im Vorhinein bekannte Aufnahmezeit mit verbesserter Genauigkeit der Bewegungskompensation sowie wesentlich weniger benötigte Expertise bei der Akquisitionsplanung.
In der vorliegenden Arbeit wird eine neuartige Aufnahmetechnik und Bewegungskorrektur für selbstnavigierte koronare Magnetresonanz-Angiographie des ganzen Herzens bei freier Atmung vorgestellt, analysiert und auf einem klinischen Kernspintomographen implementiert. Die vorgeschlagene Methode basiert auf einer neuartigen geschachtelten dreidimensionalen Radialtrajektorie, die mathematisch aus einem spiralen phylotaktischem Muster konstruiert wird. Ihre spezifischen Charakteristika garantieren eine intrinsische Minimierung von Wirbelstromartefakten der verwendeten Balanced-SSFP-Akquisition (Aufnahme bei symmetrisch ausgeglichener freier Präzession im stationären Zustand) bei gleichzeitig stets uniformer Abdeckung des K-Raumes. Die selfnavigierte Atembewegungsdetektion wird anhand von Bildauslesezügen in superiorer-inferiorer Richtung durchgeführt und basiert auf einer Methode zur Isolierung und automatischen Segmentierung des hellen Blutsignales. Die eigentliche Bewegungskorrektur des segementierten Blutreservoirs wird dann mittels Kreuzkorrelation durchgeführt. Diese vollautomatische selbstnavigierte Methode bietet eine

einfache und robuste Lösung für die koronare MRT-Bildgebung, die auch in klinische Routineuntersuchungen integriert werdne kann. Die Technik wurde an Freiwilligen getestet und mit dem Gatingansatz als Referenz verglichen. Sie erlaubte, nach bestem Wissen des Autors, das erste Mal die Anwendung solcher Selbstnavigations-Techniken in einer großen Patientenstudie in einer erweiterten klinischen Umgebung.

Acknowledgments

I have always thought that the main problem of the Acknowledgements section is: one is always afraid to skip somebody important. Now, while I am in the process of writing this page, I know there are a lot of important people I really want to thank. To try not to miss anybody, I thought of inverting the usual order: and start from the beginning towards the end.

The first, warm, "thank you" goes to my parents, Manrico and Veliana, my brother Tommaso and my whole family in general. Without them, without their love and their constant support, none of the goals I achieved would have been possible. The second of these initial thanks goes to my lifelong friends in Italy: Matteo (Defra), Massimo (Maestro), Michele (Riss), Gino, Marco, Emanuele, Alessandro (il visconte), Alessandro (Bebo), Nicola (Panoz), and Paolo, with whom I shared and share some of the best moments, laughs and jokes of my life. I hope that these good times will continue always, regardless where we are in the world or what we are doing. At this point, I owe a double special acknowledgement to Andrea "Capitan" Tiso. First, because Princeton was originally his idea (and everything started from there), and second, because he has demonstrated that he is one of the best friends that somebody can have.

"Vielen vielen dank" to Dr. Jens Guehring, not only for his very good supervision during my time in the US, but also for his friendship, for his invaluable advices and for being always there (and with there, I mean both Princeton and Erlangen) for any constructive discussion. Thanks to all the friends with whom I shared the SCR experience and with whom I wish to always keep a special bound. Thanks to Philipp Wolber, who for me represented, at the beginning, the transition from Princeton to Erlangen. In these years, he has never failed to help me when I was in need and his friendship is for me of really great value.

I want to thank Prof. Dr.-Ing. Joachim Hornegger for giving me the opportunity of joining his highly qualified group of PhD students, for his advices and for all the things I could learn at the LME. A big thank you goes to Edgar Mueller, who gave me the possibility to be part of the Cardio team in Erlangen for these intense three years of my PhD. Thank you very very much to Arne Littmann and Michael Zenge, not only for the constant, highly qualified supervision, but also for their friendship and for all the things (and they are really a lot of things) that they have taught me about my job, as well as about life. Warm thanks for the rest of the cardio team at Siemens MR in Erlangen: Michaela, Manuela, Peter, Andreas, Peter, Carmel, Aurelien, Katrin and Sonia. The amount of things I learned with them is countless and the good times we shared, at work or in front of a Franconian beer, will always stay in my memory. Thanks to Tom Galewski, who always booked the Avanto (volunteer release) for me even when there was apparently no place in the schedule. Thanks to Eva Rothgang, who is certainly one of the most kind and helpful people I have ever met, to the "French" Philip Mewes, with whom I shared many laughs and a certain

kind of sense of humor, to Christoph Forman, with whom I enjoyed sharing both serious work and laughs, to Robert Grimm and to Jana Hutter with whom I shared tales of weird old German bedtime stories, unforgettable jokes involving half-pigs and, yes, also work stuff. A big thank you is for the two Brazilian Andre: Andre Linarth (and of course Carol and Leo), that helped me all along and gave me the possibility to beat him at basketball, and Andre de Oliveira (and of course to Kristin), who was always available for a coffee and a long discussion, and always eager to give me help and good advices. Last, but not least, I want thank all the professors and PhD students at the LME for the wonderful time at work and outside.

My work in Erlangen, finally, gave me the great chance to get in contact with Prof. Matthias Stuber, Dr. Gunnar Krueger, and Dr. Juerg Schwitter with whom I have the privilege to work today. I really want to thank them for all the opportunities they gave me and for all the challenges with which they confront me everyday. I enjoy working with them every single day, while I can do a job I truly like and which never fails to stimulate my curiosity and my interests. Thanks to all the people of the Siemens team in Lausanne (especially Tobi, for the translation of the abstract and Kieran for the corrections), to all the members of the CVMR group, to all the clinicians of the Cardiac MR center, and all the technologists at the CHUV, with whom, every week, I am happy to share work, discussions, and laughs.

Davide Piccini

Contents

Chapter 1

Introduction

1.1 Coronary Artery Disease

As the average life span of the world population increases, cardiovascular diseases (CVDs) firmly establish themselves as the most frequent cause of death in many of the most developed countries (Fig. 1.1). Coronary artery disease (CAD) represents alone more than 50% of the total CVDs [Roge 11] (Fig. 1.2), and there is a strong need for a non-invasive test that could be adopted reliably for the assessment of CAD without the use of ionizing radiation. Coronary artery disease is a pathology that involves a gradual deposition of atherosclerotic plaques of lipids, macrophages and lymphocytes within the walls of the coronary arteries that supply the cardiac muscle with oxygenated blood (Fig. 1.3). These plaques can cause the narrowing of the vessel lumen, thus resulting in a reduced perfusion of the cardiac tissue. As the human body normally tries to compensate any physiological imbalance and maintain homoeostasis, this disease might not display obvious symptoms and remain unnoticed for a long time. Nevertheless, in more severe cases, CAD manifests itself as angina pectoris, difficulty in breathing and pain or discomfort in areas of the upper body. Significant reduction in perfusion of the cardiac muscle can cause local ischemia and myocardial infarctions. Acute myocardial infarction is also very likely to occur if the atherosclerotic plaque ruptures, such that its fibrous cap causes a thrombotic stenosis of the coronary lumen.
Coronary heart disease is the leading cause of death in the western world. It is estimated that approximately every 25 seconds, an American has a coronary event and, approximately every minute, someone dies of one. Myocardial infarctions in individuals that did not present warning symptoms are estimated to be approximately

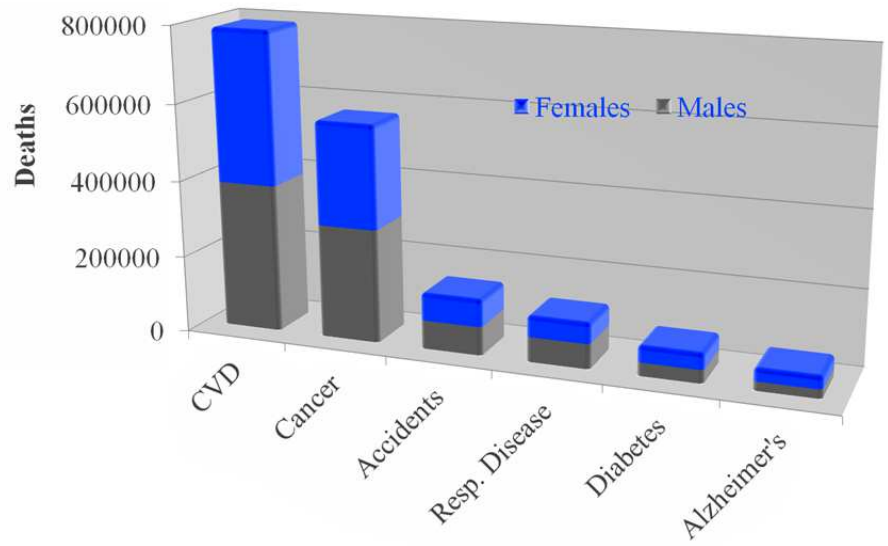

Figure 1.1: Chart representing the leading causes of death in the United States of America in 2011 [Roge 11]. Cardiovascular diseases are by far established as the most frequent cause. This image is courtesy of Prof. Matthias Stuber.

two hundred thousand per year [Roge 11].
Screening and early diagnosis of CAD are highly desirable goals for modern medicine. In the recent years, medical imaging has established itself as a very powerful tool for the assessment of the coronary vessels and daily examinations are performed everyday all over the word.

1.2 Coronary Imaging and Motion: A Challenge

A fast and precise assessment of the coronary tree is certainly one of the great challenges for any medical imaging modality. First, high contrast between the coronary lumen and the surrounding tissue is essential for adequate visualization of the coro-

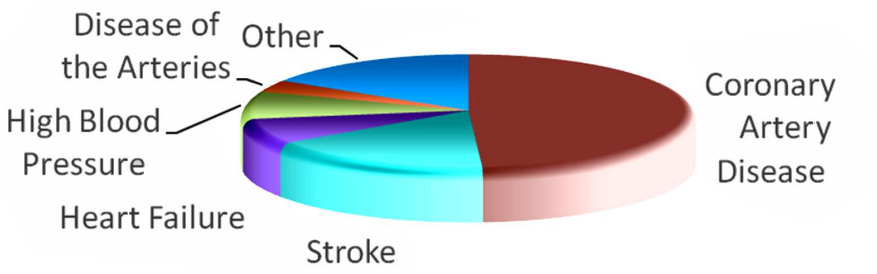

Figure 1.2: As displayed in this pie chart, CAD represents more than half of the total amount of cardiovascular diseases in the USA. This image is courtesy of Prof. Matthias Stuber.

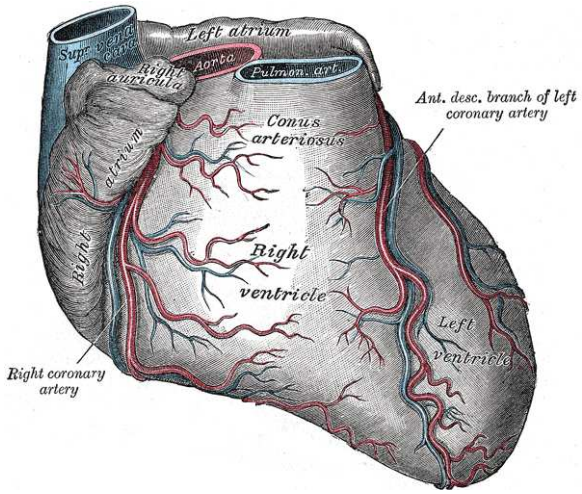

Figure 1.3: Reproduction of a lithograph plate from Gray's Anatomy [Gray 18]. The figure shows an anterior view of the heart: the right coronary artery and the anterior descending branch of the left coronary artery are highlighted in red.

nary arteries. Second, the coronaries are generally tortuous and small in diameter (3 to 6 mm) [Mann 07, Dodg 92] and, therefore, high isotropic spatial resolution of the order of 1 mm or less is required. Last, but not least, coronary arteries are constantly subjected to both cardiac and respiratory motion. The displacements due to such motion are typically larger than the actual size of the coronary vessels and, therefore, need to be compensated for.

1.2.1 Cardiac Motion and ECG Triggering

The heart is the organ responsible for providing the entire body with constant oxygenated blood supply. It is divided into four hollow chambers, two atria and two ventricles, surrounded by an involuntary striated muscle named myocardium. The heart basically behaves like a double pump: the ventricles periodically press the blood into the aorta (left ventricle) and the pulmonary trunk (right ventricle) synchronously. The periodic motion of the heart can be subdivided into a phase of contraction, called systole, and one of relaxation, the diastole. The contraction of the myocardium is regulated by an electrical signal, triggered by the cells of the sinoatrial node.
The electrical activity of the heart provides an indirect information on the cardiac motion. This information can be recorded using an electrocardiograph (ECG or EKG), by means of electrodes attached to the outer surface of the skin. The recording produced by the ECG is called electrocardiogram. Three main events can be identified within an electrocardiogram: the P-wave, the QRS-complex and the T-wave. As shown in Fig. 1.4, the systole starts in correspondence with the falling edge of the R-wave: the ventricular muscles start to contract. The volume of the ventricles remains constant (A) until the pressure becomes bigger than the pressure in the aorta and the pulmonary trunk. Then, the ventricles contract and the blood is quickly ejected (B). At the end of the T-wave, during the diastolic phase, first the ventricles start to relax without increasing in volume (C), and then, during the so-called mid-diastole

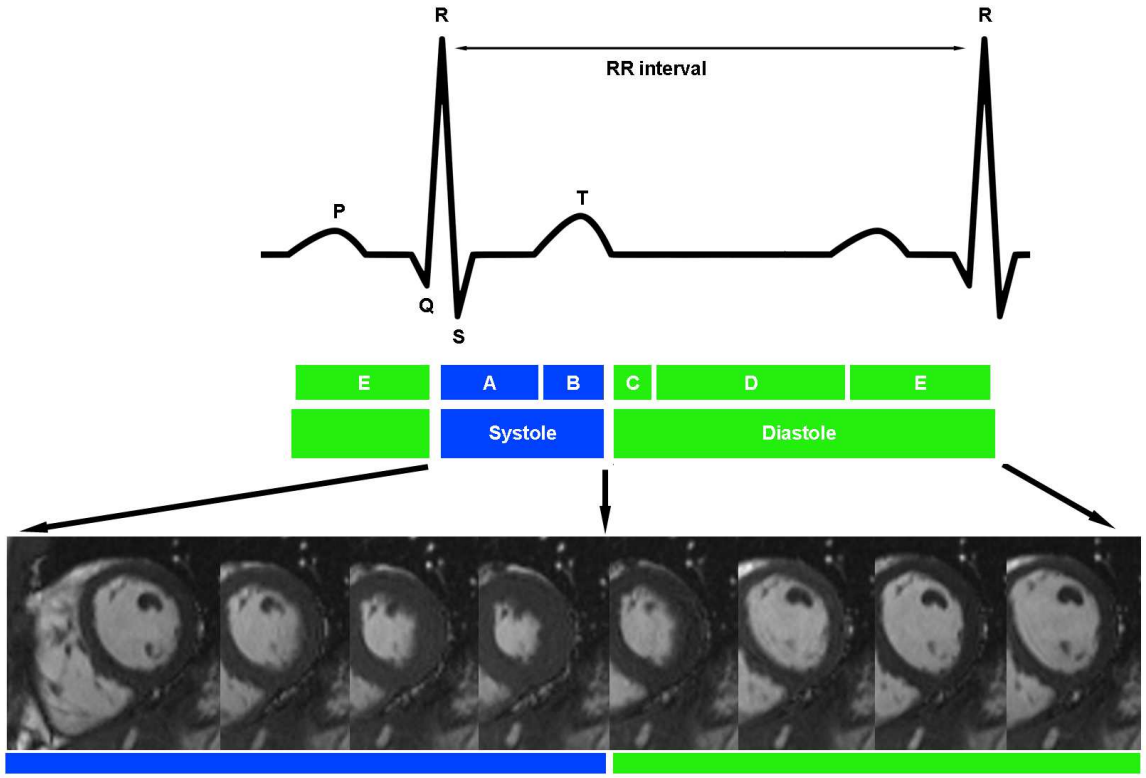

Figure 1.4: An example of a typical ECG signal is coupled with a temporal series of magnetic resonance (MR) images to show the contraction (systole: A, and B) - relaxation (diastole: C, D, and E) process of the left ventricle over a complete cardiac cycle. The duration of a cardiac cycle is defined by the time delay between two consecutive R-waves and it is often referred to as R-R interval. A more specific description of the motion within the R-R interval can be found in the text.

(D), are passively refilled. In end-diastole, the atria contract and actively complete the filling of the ventricles (E). The difference in volume of the ventricles between diastole and systole, over the total diastolic ventricular volume, is called ejection fraction (EF). The measurement of the EF is routinely performed in almost all cardiac examinations and is considered one of the most important predictors of prognosis.
The motion pattern of the coronary arteries is determined by the motion of the ventricles for which they provide blood supply. Hence, in the process of imaging the coronaries, cardiac induced vessel motion needs to be carefully taken into account [Wang 99].

1.2.2 Respiratory Motion

The topic of heart motion due to respiration has been and is still widely discussed. Exploring the possible use of computer tomography (CT) for thoracic imaging, an image-based study on the respiratory motion of the heart was conducted in 1977 by Bogren et al., using 2D cineangiography [Bogr 77]. In this study it was observed that the heart moved with respiration approximatively half as much as the diaphragm (which, on average, moves of about 15 mm) along the superior-inferior direction (SI

direction), during shallow or normal respiration. In 1995, driven this time by the need to address the limitations of cardiac MR imaging (MRI), Wang et al. published a study based on 2D MR images, acquired at multiple breath-hold levels [Wang 95]. They too concluded that the primary motion of the heart due to respiration is a translation in the SI direction (Fig. 1.5). The reported SI displacement of the heart, in ten healthy volunteer, was, on average, about 0.6 times the corresponding SI displacement of the diaphragm. In 2002, a successive study, based on rigid registration

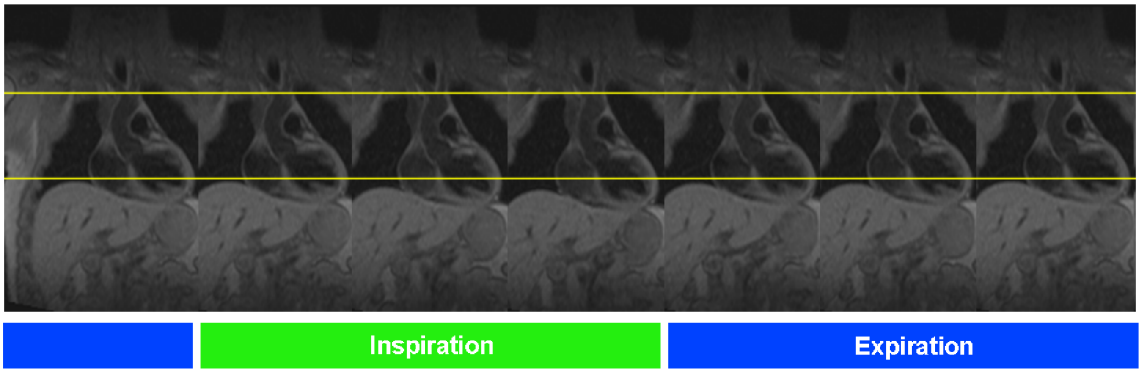

Figure 1.5: Series of six coronal MR images showing the effect of respiratory motion on both the diaphragm and the heart, along the SI direction. The displacement of the diaphragm can be inferred from the position of the liver (the bright structure on the left, under the lower yellow line). The two yellow lines were added to facilitate the visualization of the displacement: while almost no motion occurs at the level of the upper line, the lower line shows how both diaphragm and heart shift downwards during inspiration.

of 3D MR images and, again, using multiple breath-hold levels, reported also minor translations in antero-posterior (AP) and right-left (RL) direction as well as minor rotational components [McLe 02]. In the same year, Manke et al. used a landmark based approach to compare different motion models of respiratory motion of the heart [Mank 02]. This study was based on 3D coronary MR images acquired with a guided breath-hold technique. In this case, the best model to describe heart motion due to respiration was found to be a 3D affine transformation. Less accurate results could be achieved by simple 1D or 3D translation.
With the aim to overcome the intrinsic limitations in spatial and temporal resolution of MRI, Shechter et al. tried to quantify the respiratory motion using coronary artery X-ray angiography [Shec 04b, Shec 04a]. Over ten analysed patients, the mean SI translation detected was 4.9 ± 1.9 mm. An average cranio-dorsal rotation of $1.5° \pm 0.9°$ was observed during inspiration. Furthermore, an average AP translation of 1.3 ± 1.8 mm as well as a caudo-dextral rotation of $1.2° \pm 1.3°$ was reported in eight patients. Beside what could be considered as minor differences, all these studies concluded that the major displacement of the heart, due to respiratory motion, occurs along the SI direction. Nevertheless, the overall motion pattern is certainly more complex and a very high inter-subject variability was always observed [Dani 97].

1.2.3 Patient Motion

As the patient usually is subjected to stress during the examination and might have to lay down in the same position for a prolonged amount of time, the motion of the whole body must be taken into account. For cardiac examinations, in general, this problem is addressed by asking the patient to remain as still as possible during data acquisition. As a lengthy acquisition naturally increases the probability of patient motion, keeping the acquisition time as short as possible is, in general, one of the goals of all cardiac imaging techniques.

1.3 Clinical Imaging of the Coronaries

In most cases, 2D X-ray coronary angiography [Scan 99] is still the current clinical gold standard for imaging the coronaries. This modality offers high spatial (1.0-3.3 line pairs/mm) and temporal (15-30 frames/second) resolution and it is widely used to assess the anatomy of the coronary tree as well as to judge the degree of lumen obstruction [Shec 04a]. The examination with X-ray angiography, although classified as minimally invasive, requires the use of a catheter. Furthermore, an intra-arterial bolus of iodinated contrast agent is directly injected during the procedure and both the patient and the physician are exposed to potentially harmful ionizing radiations during the whole examination. Although the patient is awake and constantly monitored during the entire procedure, the risk of severe complications is always present. Furthermore, X-ray coronary angiography is a very expensive procedure [Desa 03] and, on average, up to 40% of the examined patients are found to have no significant coronary artery stenosis [Diss 02].

After considering all the shortcomings intrinsically associated with X-ray coronary angiography, the necessity of a cheaper, non-invasive, patient friendly and low-radiation or radiation-free technique is evident [Faya 02]. Low dose computerized tomography [Hoff 05, Stei 08], flat-panel detector C-arm system [Stro 09, Rohk 10] and magnetic resonance imaging [Stub 07, Haus 08] are nowadays the main candidates for this task. With the first two modalities, high spatial resolution and short acquisition times are already possible. The flat-detector C-arm systems, for example, can achieve ~ 0.3 mm isotropic resolution in a total imaging time of 5 s. Nevertheless, injections of contrast agent are still needed and the two techniques still expose patients and doctors to some amount of X-ray radiations.
MRI, on the other hand, is a completely non-invasive and non-harmful technique that can provide true 3D imaging in all arbitrary orientations and excellent soft-tissue contrast without the use of any contrast agent. Furthermore, MRI has the potential to combine both morphological and functional imaging, e.g. perfusion imaging of the myocardium, such that a complete picture of CAD can be provided during a single examination.

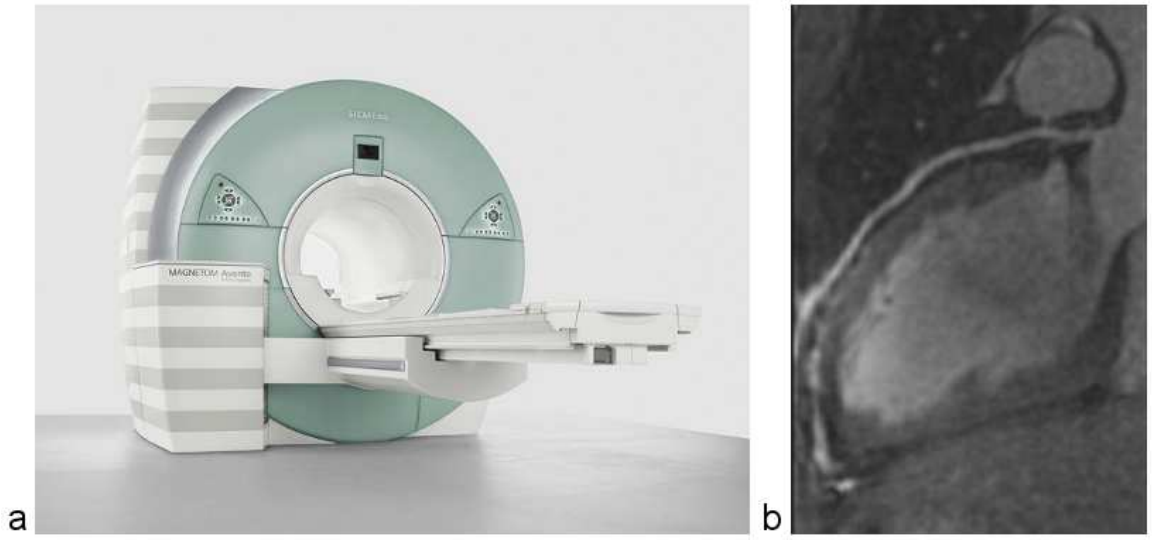

Figure 1.6: (a) Example of clinical MR scanner. This image is courtesy of Siemens AG, Healthcare Sector, Erlangen, Germany. (b) Example of coronary MRI angiogram.

1.4 Scientific Focus and Research Contributions

Despite the large improvements obtained over the last twenty years, coronary MRI still remains a very challenging task. First, the complex anatomy of the coronary tree requires extensive scout scanning to precisely plan the actual data acquisition. Second, the amount of data needed to cover the coronary tree with sufficient resolution and the current speed limitations of the MR scanners do not allow acquiring the data within a fraction of a heartbeat. Data acquisition must be split into multiple heartbeats, i.e. using an interleaved (or segmented) acquisition. In this context, examinations performed during free-breathing are preferable over breath-hold acquisitions for a number of reasons. First, this setup is much more comfortable for the patient. Patients with cardiac problems, as well as paediatric patients, have difficulties in maintaining even a short breath-hold. Second, the acquisition time does not need to be constrained to a breath-hold window and can therefore be noticeably increased. Finally, free-breathing acquisitions are commonly considered to be more clinically relevant than extended breath-holds, as the latter can lead to poorly understood changes in the blood flow and pressure in the region of the heart. In a free-breathing scenario, compensation techniques for both cardiac and respiratory motion must be applied.
Monitoring of the cardiac activity by means of an MR compatible ECG is a well established practice that allows triggering the acquisitions always in the phase where the myocardial motion is minimal (Fig 1.4 (D): mid-diastole). Heart motion due to respiration can be tracked either indirectly, i.e. using state of the art navigator-gated techniques, or directly, i.e. with self-navigation. An extensive description of the state of the art of coronary MR imaging and its limitations will be given in Section 2.4.
Improving the ease of use, the speed and the efficiency of coronary MR imaging is essential for this technique to become clinically viable. In particular, methods for

precise evaluation and compensation of the respiratory motion are proposed in this work, which allow the acquisitions to be performed reliably without the use of a navigator. Complete integration of the proposed algorithms into the existing image acquisition and reconstruction frameworks was considered an essential feature. The following research contributions were achieved:

- A novel 3D radial k-space trajectory, optimized for whole-heart coronary MRI with minimal imaging artifacts, was developed, implemented and experimentally analysed. The 3D acquisition of the whole heart allows to bypass the scout scanning for the localization of the coronaries and allows easy and fast acquisition planning. The novel trajectory was implemented such that evaluation and correction of the respiratory motion could be straightforwardly integrated into the existing framework of our industry partner.
- A robust method to reliably determine the respiratory position of the heart at every heartbeat, i.e. respiratory self-navigation, is described. This method allows to isolate and segment the blood pool along the SI direction, within the very same data acquired for imaging. At every heartbeat, the position of the blood pool is detected and used to compute its displacement with respect to a reference. Hence, motion correction along the direction of major displacement can be performed inline. Not only this technique improves previously proposed approaches with respect to precision and robustness, but is also fully integrated into the online reconstruction framework. Datasets corrected for respiratory motion can be acquired and visualized directly at the MR scanner.
- The novel self-navigated MR acquisition and reconstruction strategy, described in the first part of the thesis, was inserted as an optional examination in routine cardiac MR examination in a clinical environment. Several patient datasets were acquired and image quality was qualitatively and quantitatively assessed by experts in the field. The diagnostic performances of this novel technique were evaluated for the detection of coronary artery stenoses as well as for the identification of congenital anomalies of the coronary arteries.

1.5 Organization of the Thesis

In the following section, a chapter-wise overview of the structure of this thesis is presented. The organizational structure is also depicted in Fig. 1.7.

Chapter 2

In the second chapter a brief, but comprehensive introduction to the basics of MRI is provided. The elementary principles of nuclear magnetic resonance (NMR) and the concepts of spatial encoding, k-space and imaging sequences are described. Non-Cartesian MR imaging techniques are introduced and, in particular, the theory of 3D radial imaging is explained with respect to both the specific imaging sequence structure and reconstruction algorithms. Eddy current artifacts and motion artifacts

are introduced and will be addressed respectively in Chapter 3 and 4. Last, but not least, a review on the current state of the art of coronary MR imaging is provided.

Chapter 3

In this chapter, a novel 3D radial trajectory based on a spiral phyllotaxis pattern is introduced, which integrates both an overall uniform distribution of the acquired readouts and minimal eddy currents. Furthermore, this trajectory is intrinsically prepared for self-navigated cardiac MRI. These features are theoretically assessed in comparison with two alternative 3D radial trajectories based on two different implementations of an Archimedean spiral pattern. The image quality achieved with the novel approach in phantoms is compared with that of images acquired with one of the Archimedean trajectories. Finally, the improvements obtained with the new trajectory are evaluated for navigator-gated whole-heart coronary MRI acquisitions in 6 healthy volunteers. Major parts of this chapter are published in [Picc 11].

Chapter 4

In the fourth chapter, a new approach for improved performance of self-navigated whole heart coronary MRI is described. An innovative technique to isolate the blood pool is presented. This technique is based on the combination of the output signals from a phased-array surface receiver coil, placed on the chest. Furthermore, an algorithm for the automatic segmentation of the blood pool is proposed. Signal suppression, automatic segmentation, motion detection and compensation are fully integrated in the data acquisition and reconstruction framework to allow a fast and easy workflow for coronary MR imaging. The results of the self-navigation are compared with the navigator-gated technique in 10 healthy volunteers. Major parts of this chapter are published in [Picc 12].

Chapter 5

The aim of this chapter is to evaluate the image quality and diagnostic performance of the self-navigated acquisitions described in the previous chapter for the detection of coronary artery stenoses as well as for the identification of congenital anomalies of the coronary arteries. To enable initial testing of this sequence in patients, the time gap between perfusion imaging and 2D late gadolinium enhancement (LGE) in routine clinical scans was exploited for high-resolution self-navigated, 3D whole-heart imaging without affecting overall scan time. Major parts of this chapter are submitted as a full paper for peer review.

Chapter 6

In chapter six, a comprehensive overview of the thesis is provided. The scientific contributions of the present work are summarized.

Chapter 7

In this last chapter, future improvements of the proposed technique and open points are broadly discussed. Further possible applications of the described self-navigated approach are listed.

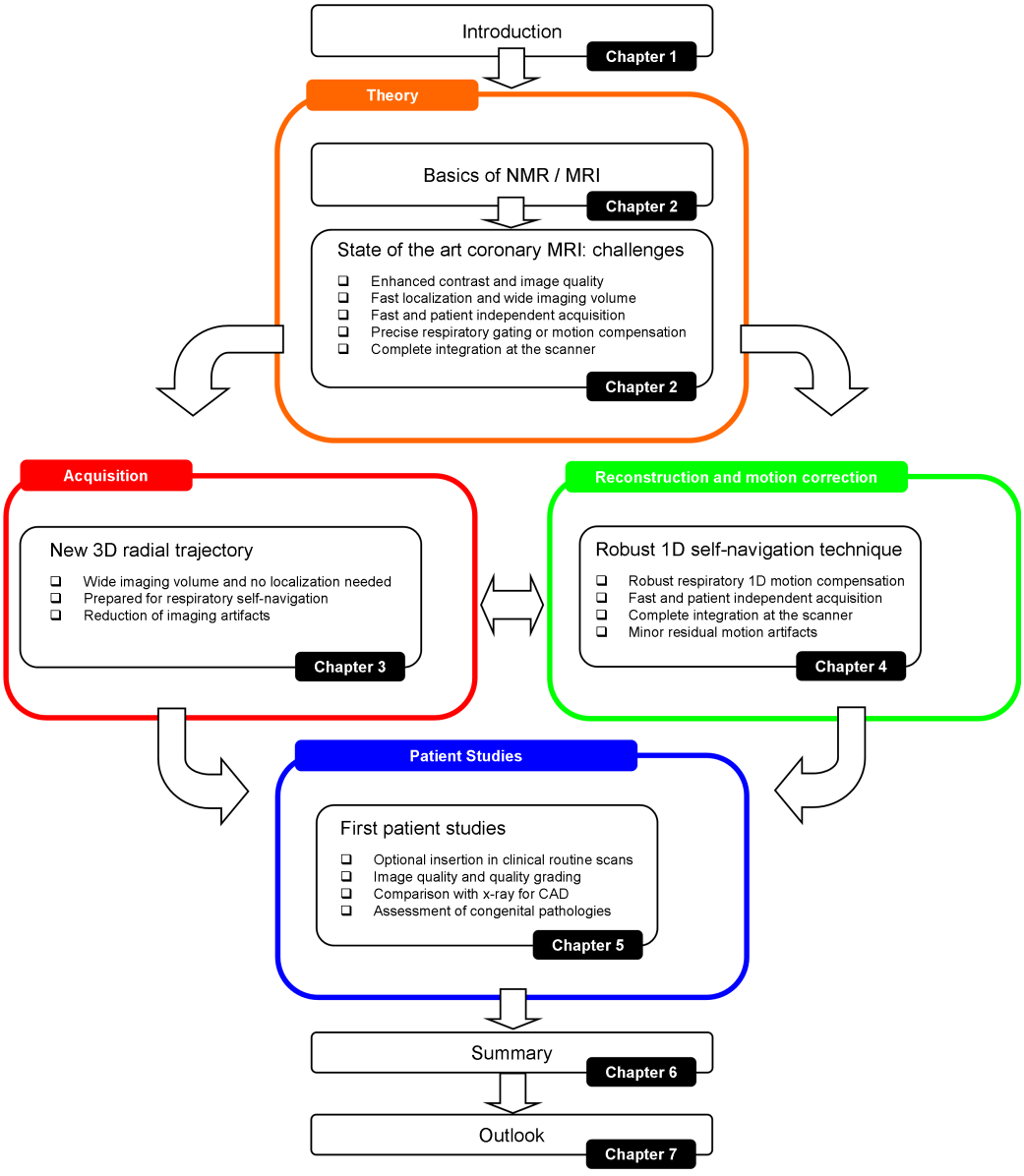

Figure 1.7: Organizational structure of the thesis.

Chapter 2

Theoretical Background on Coronary MRI

2.1 Basics of NMR

Nuclear magnetic resonance (NMR) is a physical phenomenon by which certain nuclei, interacting with an external magnetic field, can absorb and re-emit electromagnetic radiation at a specific resonance frequency. The basic physical principle of nuclear magnetic resonance was first described about 60 years ago, in 1946, by Felix Bloch [Bloc 46] and Edward Mills Purcell [Purc 46]. The two physicists were awarded the Nobel prize in physics in 1952.

This section provides a brief introduction of the basics of NMR. First, the concepts of nuclear magnetic moment and macroscopic magnetization will be explained, then, the principles of radio frequency (RF) excitation, relaxation and NMR signal will be introduced. A much more detailed introduction to NMR can be found in many textbooks on these topics, such as [Haac 99].

2.1.1 Spin Behaviour in a Magnetic Field

The angular momentum, or spin, is a fundamental property of elementary particles, such as protons, neutrons and electrons. From a classical physics prospective, protons can be seen as rotating particles with a positive electrical charge and can be represented by a magnetic dipole moment (Fig. 2.1). As proton spins tend to pair up as much as possible, the total magnetic moment of atomic nuclei with an even number of protons is zero. On the other hand, a nucleus containing an odd number

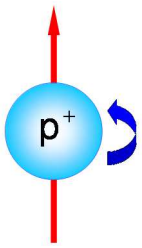

Figure 2.1: Schematic representation of a proton as a magnetic dipole moment.

of protons is always associated with a net nuclear magnetic moment and, therefore, can interact with external magnetic fields. The nucleus of the hydrogen atom (^{1}H) is constituted by a single proton and is that of most prominent interest for clinical NMR imaging, as it is abundantly present in all biological tissues. The amount of water (H_2O) in the human body, for example, is in average higher than 60% of the total volume.

When no external magnetic field is applied to a probe, the magnetic moments of all hydrogen nuclei are arbitrarily oriented and the net magnetic moment of the probe equals zero. When the ^{1}H atoms are placed in an external magnetic field $\boldsymbol{B_0}$, the magnetic dipoles align along $\boldsymbol{B_0}$ and can be either parallel or anti-parallel to it. Furthermore, the dipoles start to precess around the direction of the magnetic field at a constant resonant frequency, proportional to the intensity of $\boldsymbol{B_0}$: the Larmor frequency (ν_L)

$$\nu_L = \gamma B_0 \tag{2.1}$$

The gyromagnetic ratio γ is a constant characteristic of every nucleus. In the case of hydrogen:

$$\gamma = 2\pi \cdot 42.577 \text{ MHz/T} \tag{2.2}$$

The parallel and anti-parallel states are associated with two different energy levels:

$$E = -m\hbar\gamma B_0 \tag{2.3}$$

where $\hbar$ denotes the Planck's constant and m is the spin magnetic quantum number that can only assume values of $+1/2$, i.e. parallel or *spin up* state, or $-1/2$, i.e. anti-parallel or *spin down* state (Fig. 2.2). The difference between the two energy levels is given by:

$$\Delta E = \hbar\gamma B_0 \tag{2.4}$$

and, therefore, directly depends on the strength of the external field B_0. A hydrogen nucleus can go from the lower to the higher energy state by absorption of a photon,

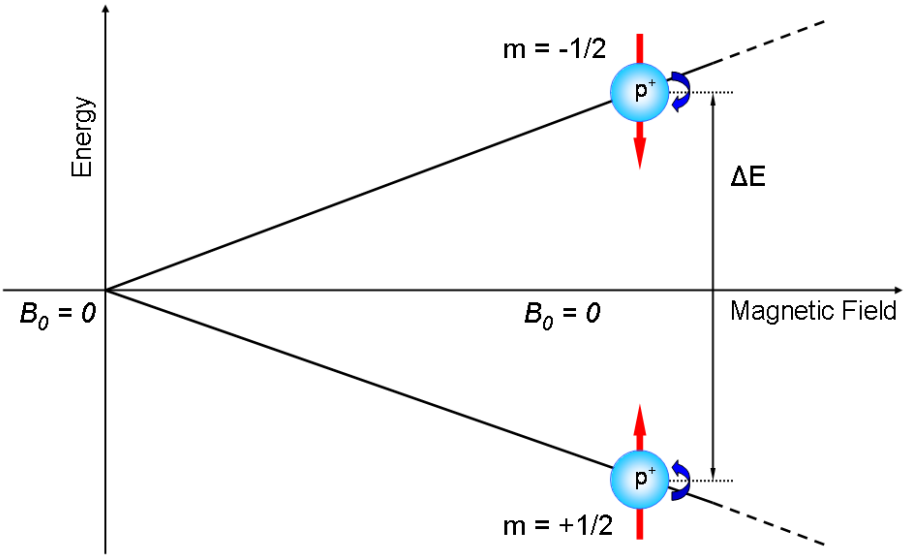

Figure 2.2: Schematic representation of the linear dependence between the strength of the external magnetic field B_0 and the energy level difference characterizing the aligned *spin up* and *spin down* nuclei.

but only if the energy of the photon is exactly equal to ΔE. The energy of a photon E_p is:

$$E_p = \hbar\nu \tag{2.5}$$

with ν being the frequency of the photon. This means that a transition to the upper energy level can occur only if $\nu = \gamma B_0 = \nu_L$. With a B_0 field of 1.5 T, a frequency of $\nu_L = 63.6$ Mhz, i.e. in the RF range, is required.

2.1.2 Macroscopic Magnetization

If the magnetic moments of all dipoles in a unit volume are added up and considered as a whole, their behaviour can be described in a macroscopic setting. The net magnetic moment of the unit volume can be represented by a magnetization vector $\boldsymbol{M}$. In the presence of the external magnetic field $\boldsymbol{B_0}$, $\boldsymbol{M}$ is proportional to the difference between the two possible energy levels and can be described by the electric dipole momentum equation:

$$\frac{d\boldsymbol{M}}{dt} = \gamma \boldsymbol{M} \times \boldsymbol{B_0} \tag{2.6}$$

As described for the single nuclei, at equilibrium, the net magnetization $\boldsymbol{M}(0)$ is aligned with $\boldsymbol{B_0}$. Its transversal component equals zero and its precession frequency is ν_L. If energy is added to the system at the time t_0 by applying an RF pulse at the resonant frequency ν_L, the vector $\boldsymbol{M}(t_0)$ is flipped by an angle α (also known as the nutation angle). All magnetic moments start to precess in phase and a non-zero

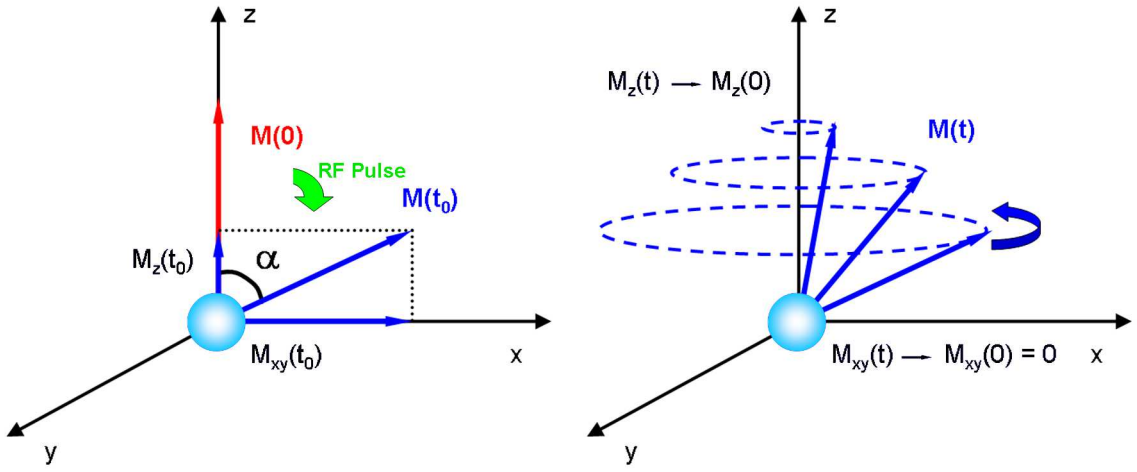

Figure 2.3: Schematic representation of the excitation-relaxation process of the magnetic moment $\boldsymbol{M}(0)$ initially oriented along the direction of $\boldsymbol{B_0}$ on the z axis. (a) If RF energy is added to the system at t_0, the magnetic moment is flipped towards the transversal plane xy with a flip angle α and $\boldsymbol{M}(t_0)$ can be decomposed into a transversal $M_{xy}(t_0)$ and a longitudinal $M_z(t_0)$ component. For convenience $\boldsymbol{M}(t_0)$ is represented, here, on the xz plane. (b) Once the RF pulse is switched off, the magnetic moments relax back to the original orientation, such that the transversal component $M_{xy}(t) \rightarrow 0$ and the parallel component $M_z(t) \rightarrow M_z(0)$.

transversal component is formed (Fig. 2.3a). The so-called flip angle α is the angle between the current orientation of the magnetization and the direction of the static magnetic field. Its value depends on the duration and on the strength of the RF pulse. Because the magnetization vector precesses for the whole time around the axis of $\boldsymbol{B_0}$, its behaviour is usually described using a non-static frame of reference, which rotates with a constant angular velocity, at the Larmor frequency.

2.1.3 Relaxation and NMR Signal

When the RF excitation is switched off, the magnetization $\boldsymbol{M}$ relaxes towards the original equilibrium orientation $\boldsymbol{M}(0)$. At every point in time t, the magnetization vector $\boldsymbol{M}(t)$ can be decomposed into a transversal and a longitudinal (parallel to $\boldsymbol{B_0}$) component, as shown in Fig. 2.3. In the usual MR conventions in notation, the longitudinal component is considered to be parallel to the z axis ($M_z(t)$), whereas the transversal component lays on the xy plane ($M_{xy}(t)$). The relaxation process of $\boldsymbol{M}(t)$ is described using the solution of the Bloch equations [Bloc 46]:

$$M_z(t) = M_z(0) - [M_z(0) - M_z(t_0)] \cdot e^{-t/T_1} \tag{2.7}$$

$$M_{xy}(t) = M_{xy}(t_0) e^{-t/T_2} \tag{2.8}$$

The longitudinal magnetization M_z rebuilds to $M_z(0) = |\boldsymbol{M}(0)|$ with the relaxation constant T_1, due to the interaction of the proton spins with the neighbouring

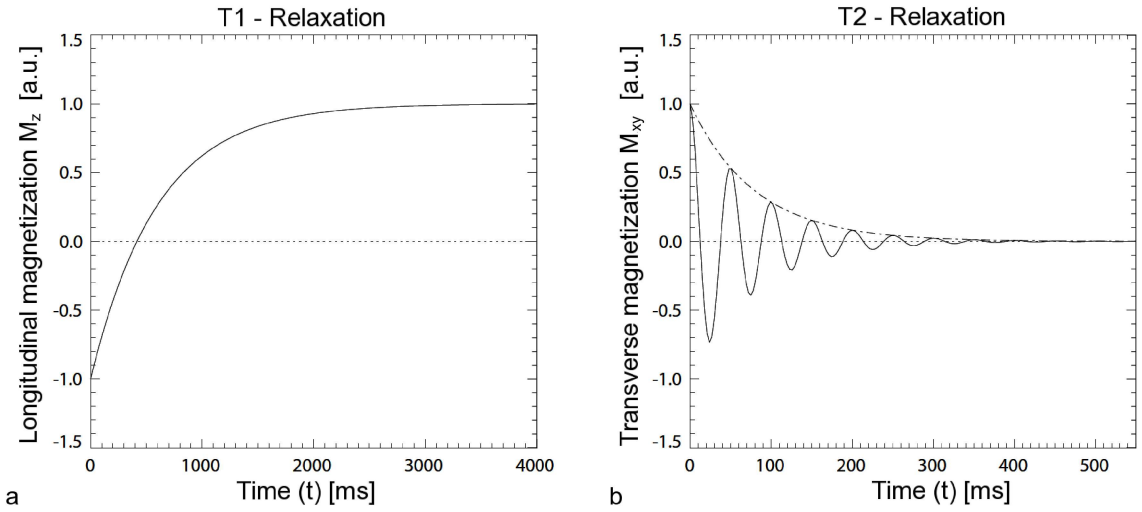

Figure 2.4: T_1 and T_2 relaxation. (a) The longitudinal component of the magnetization, $M_z(t)$, recovers to the initial value with the time constant T_1. (b) The transversal component of the magnetization, M_{xy}, decays with the time constant T_2. This image is courtesy of Dr. Sonia Nielles-Vallespin and was adapted from [Niel 04]
.

molecules, i.e. the spin-lattice relaxation (Fig. 2.4a and Eq. 2.7). At the same time, the interaction of neighbouring proton spins causes the dephasing of the transverse component, i.e. the spin-spin relaxation, such that the transverse magnetization vanishes with the relaxation constant T_2 (Fig. 2.4b and Eq. 2.8). The relaxation constants T_1 and T_2 are tissue-specific parameters and eventually define the final image contrast. Table 2.1 shows values of the relaxation constants for different tissues.

Tissue	$\boldsymbol{T_1}$ **[ms]**	$\boldsymbol{T_2}$ **[ms]**
Grey matter	950	100
White matter	600	80
Muscle	900	50
Cerebrospinal fluid	4500	2200
Fat	250	60
Deoxygenated blood	1200	100
Oxygenated blood	1200	200

Table 2.1: Approximative values of the relaxation times T_1 and T_2 of different tissues of the human body, for ^{1}H components at 1.5 T [Haac 99].

The rotating transverse magnetization can be detected as an inductive voltage, using RF receive coils. The time evolution of such voltage is the measured NMR signal and is referred to as the free induction decay signal (FID).

2.2 Basics of MR Imaging

Magnetic resonance imaging is nowadays one of the main and most used non-invasive medical imaging techniques. In 1973, Paul Lauterbur [Laut 73] and Peter Mansfield [Mans 73] introduced the use of gradient magnetic fields to allow spatial encoding, thus extending the NMR principle to an actual imaging modality. Although Lauterbur's and Mansfield's contribution is undisputable, it was Raymond V. Damadian who first discovered the potential of NMR for diagnostic purposes [Dama 71].

The principles of spatial encoding, which allows 3D imaging in all arbitrary orientations, will be shortly described. Afterwards, a brief introduction on the concept of k-space will be given, followed by a basic explanation of the standard Cartesian imaging sequences. Eventually, a description of the concept of 3D radial imaging will be provided, which represents an essential part of this thesis. A much more detailed introduction to MR imaging can be found in many textbooks on these topics, such as [Haac 99, Bern 04].

2.2.1 Spatial Encoding

Three sets of hardware gradient coils, G_x, G_y and G_z, are normally integrated into the MRI systems. These gradient coils can produce independent magnetic field gradients superimposed on the static magnetic field $\boldsymbol{B_0}$. A combination of these gradients can produce local variations in the strength of the magnetic field along any given direction, such that spatial encoding of the measured signal in all arbitrary orientations becomes possible. Depending on the timings with which the physical gradients are switched on and off, the gradient coils can produce three independent gradient fields, referred to as: G_S, G_P and G_F. The first gradient G_S, or slice selective gradient, is applied simultaneously with the RF excitation and is used to localize the volume excited by the RF pulse along a specific orientation. The rectangular profile of the excitation pulse in the frequency domain defines the thickness of the excited slice of proton spins, whereas its frequency determines the position of the slice (Fig. 2.5). Right after RF excitation, all the spins of the excited slice precess in-phase, with the Larmor frequency (Fig. 2.6a). The phase encoding (G_P) and the frequency encoding (G_F) gradients are used to create a correlation between the different components measured by the receiver coil with their spatial origin within the excited slice. Before the actual acquisition of the FID signal, G_P is applied orthogonal to G_S for a pre-defined period of time. The phase encoding gradient causes the proton spins to precess with frequencies that depend on their spatial location along the direction of G_P. When the phase encoding gradient is switched off, all proton spins start precessing again with the Larmor frequency, but have now different phases (Fig. 2.6b). During signal reception, the last of the gradient fields, G_F, is applied perpendicularly to both G_S and G_P (Fig. 2.6c). As a final result, at signal reception, all the excited proton spins precess with different frequencies and different phases and, therefore, induce corresponding voltages with different frequencies and phases in the receive coils.

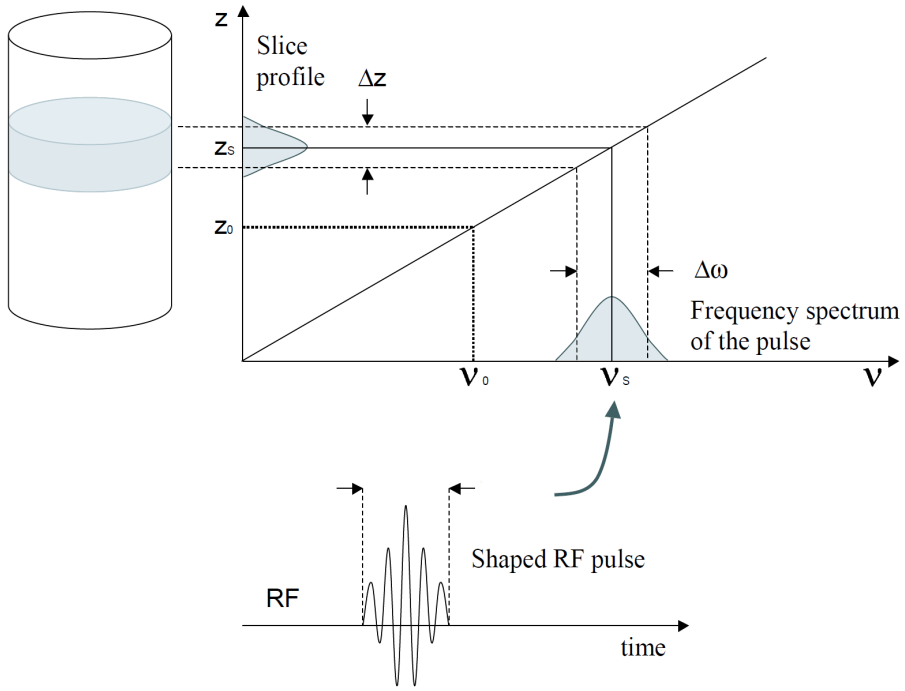

Figure 2.5: Example of slice selection with $G_S = G_Z$. The bandwidth of the RF excitation pulse determines the slice thickness Δz, while the central frequency ν_S determines the slice position Z_S. This image is courtesy of Dr. Sonia Nielles-Vallespin and was adapted from [Niel 04].

2.2.2 Frequency Domain

In the classical mathematical description, the time signal of the FID that is induced in the RF receive coils can be interpreted as a signal in the frequency domain. In MRI, such frequency domain is universally referred to as k-space. In order to obtain the actual image data, the measured MRI signal needs to be transformed by means of the inverse Fourier transformation. The image space $\rho(x, y, z)$ and k-space $S(k_x, k_y, k_z)$ are linked via the MR image equation:

$$S(k_x, k_y, k_z) = \int_x \int_y \int_z \rho(x, y, z) \cdot e^{-j(k_x x + k_y y + k_z z)} dx dy dz \tag{2.9}$$

In particular:

$$\begin{aligned} k_x &:= k_x(t) = \gamma \textstyle\int_t G_x(\tau) d\tau \\ k_y &:= k_y(t) = \gamma \textstyle\int_t G_y(\tau) d\tau \\ k_z &:= k_z(t) = \gamma \textstyle\int_t G_z(\tau) d\tau \end{aligned} \tag{2.10}$$

Slice orientation, as well as phase and frequency encoding directions, can be arbitrarily chosen by appropriate combinations of the physical gradients G_x, G_y and G_z and are varied until the target k-space is completely acquired. It is very important to note

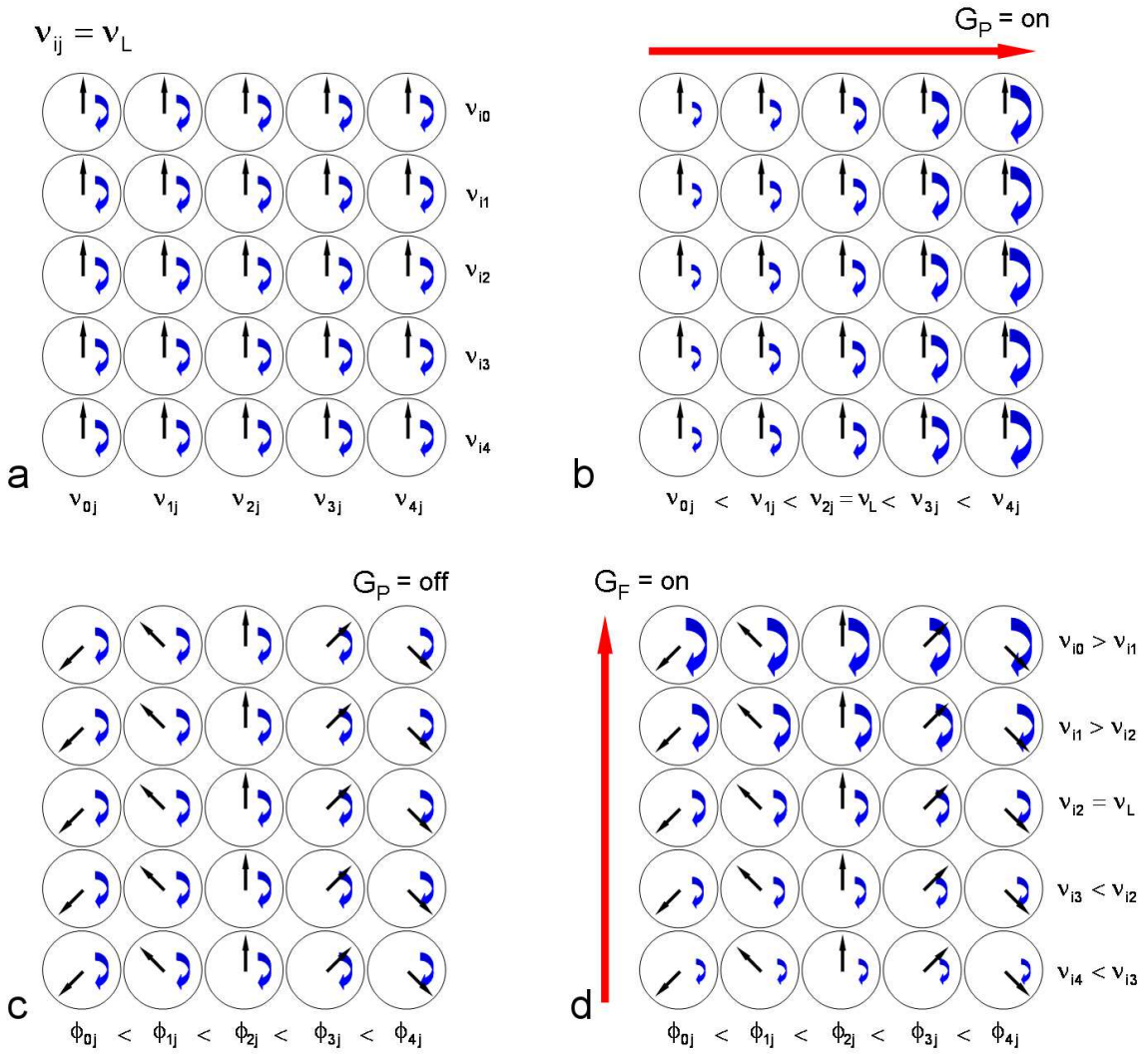

Figure 2.6: Graphical representation of the phase and frequency encoding within the excited slice. Each circle represents a proton spin after RF excitation. The small black arrows represent the individual phase of the precessing proton spins, whereas the blue curved arrow indicate their precession frequency. (a) All the spins, after slice excitation, rotate with the Larmor frequency ν_L. (b) The phase encoding gradient G_P, is applied for a limited amount of time before signal reception. (c) This has the net effect of producing a linear phase offset along the phase encoding direction, when G_P is switched off and all spins precess again with ν_L. (c) During signal reception, the frequency encoding gradient G_F is applied perpendicular to G_P. The resulting effect is that each individual proton spin precesses with an individual frequency and phase, which are directly connected to its spatial position within the excited slice.

how each single point of k-space contributes to form the entire image (Fig. 2.7a). In particular, while the central samples contain the information about the coarse structure of the imaged object and contribute to the contrast of the image (Fig. 2.7b), the peripheral samples encode the information of the fine details (Fig. 2.7c). The

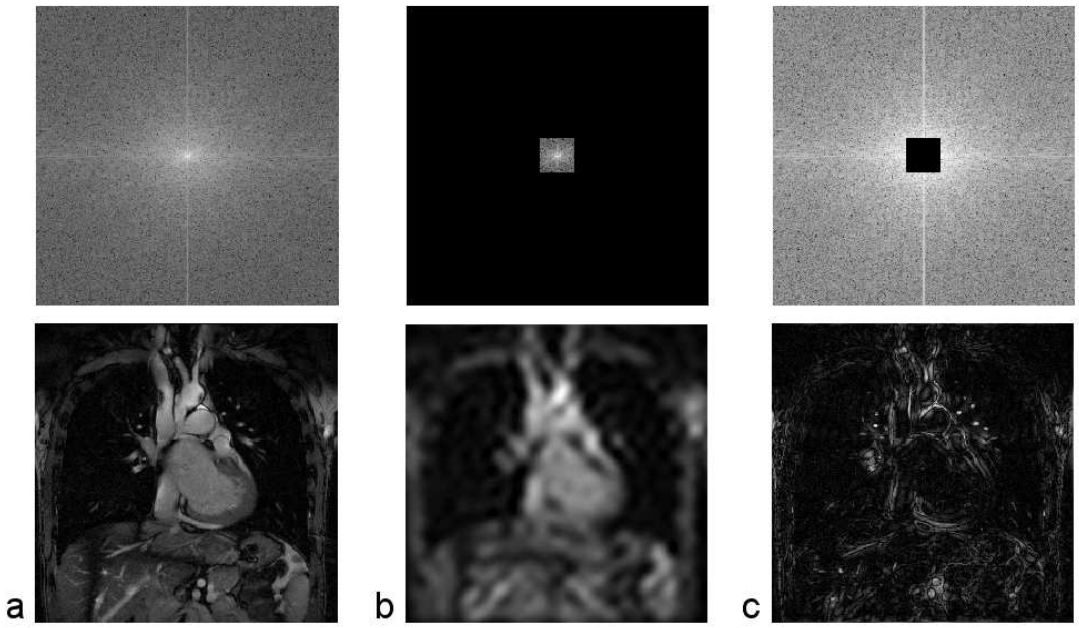

Figure 2.7: Example of 2D k-space data (first row, in logarithmic scale) and corresponding Fourier transformation (second row) of a coronal cross-section of the heart, acquired in a healthy volunteer. (a) Each point in k-space contributes to the entire image. (b) By excluding the periphery of k-space before the Fourier transformation, it is evident that the samples in the central area mainly contribute to the contrast of the image. (c) On the contrary, the peripheral samples provide the information on the edges, defining the fine detail of the image.

acquisition speed of an MR imaging technique depends both on how quickly the spatial encoding is performed and how fast the k-space data can be acquired. The signal amplitude of every voxel, after Fourier transformation, is encoded onto a grey scale to form the final MR image.

2.2.3 Imaging Sequences

The MR imaging sequences are nothing else but preselected sets of RF and gradient pulses which are precisely synchronized with predefined time spacing. The control of the RF and gradient pulses by means of a programmed sequence practically allows the user to indirectly interact with the hardware of the MRI scanner and thus to perform the spatial encoding and influence the tissue magnetization. Different choices of imaging sequences allow to obtain different soft tissue contrasts of the same imaged object and, therefore, to extract the specific information needed to perform a particular diagnosis. An example showing three of the most commonly used tissue

contrasts is displayed in Fig. 2.8.

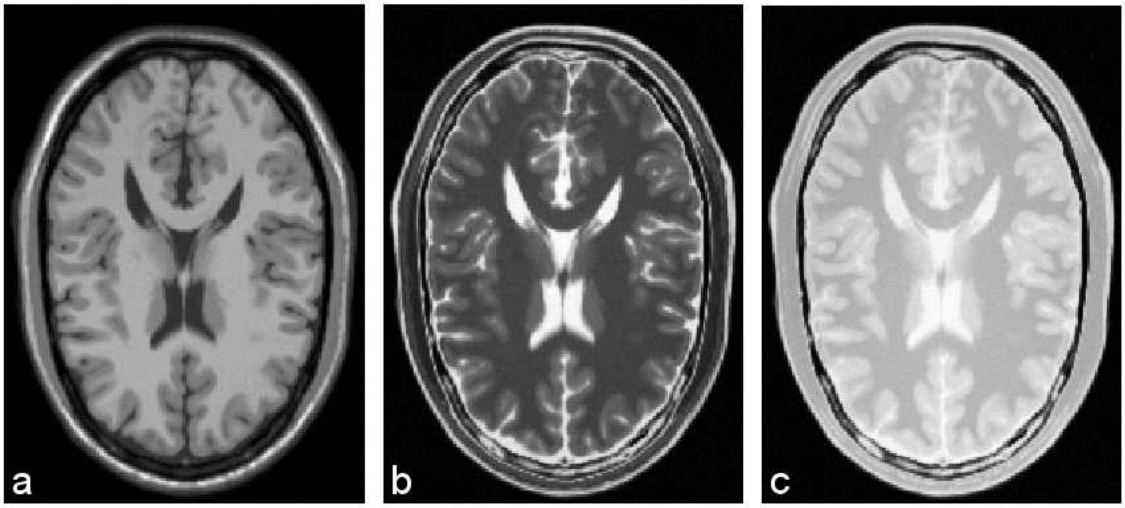

Figure 2.8: Simple example of how the soft tissue contrast can be varied with the choice of a specific imaging sequence and set of parameters. An axial cross section of the brain of a normal volunteer was acquired with: (a) a T_1-weighted contrast, (b) a T_2-weighted contrast and (c) a proton-density-weighted contrast.

Two basic families of sequences have been developed to induce an echo of the FID signal such that it can be sampled by the MR system after phase encoding: the spin echo sequence [Hahn 50], and the gradient echo sequence [Erns 66]. While the former is more robust to susceptibility artifacts and magnetic field inhomogeneities, the latter is generally much faster. In the 2D gradient echo sequence (Fig. 2.9), first a slice selective gradient, $G_S = G_z$ in the figure, is switched on during RF excitation to spatially define the acquired slice (A). Then, the phase and frequency encoding gradients, $G_P = G_y$ and $G_F = G_x$, respectively, in the figure, are used to dephase the magnetization, and to encode the position of a specific k-space line (B). Eventually, during the rephasing of the magnetization, the MR signal of the selected k-space line is measured (C). The timing of signal acquisition is physically controlled by switching on and off an analog-to-digital converter (ADC). The echo occurs when the center of k-space is acquired and the echo time is conventionally referred to as TE. This process is repeated until the whole selected slice is sampled and the amount of time between successive RF excitation pulses is the so called repetition time (TR).
An evolution of the basic gradient echo sequence are the so-called steady state sequences, as FLASH (Fast Low Angle SHot) [Haas 86] and bSSFP (balanced Steady State Free Precession) [Oppe 86, Duer 98]. These sequences allow an extreme acceleration of the acquisition, without substantial loss of image quality, and are now widely used in many different fields in common clinical practice. In particular, bSSFP is widely used in many cardiac MRI applications, both for its speed and relative motion insensitivity, as well as for the optimal blood-myocardium contrast.

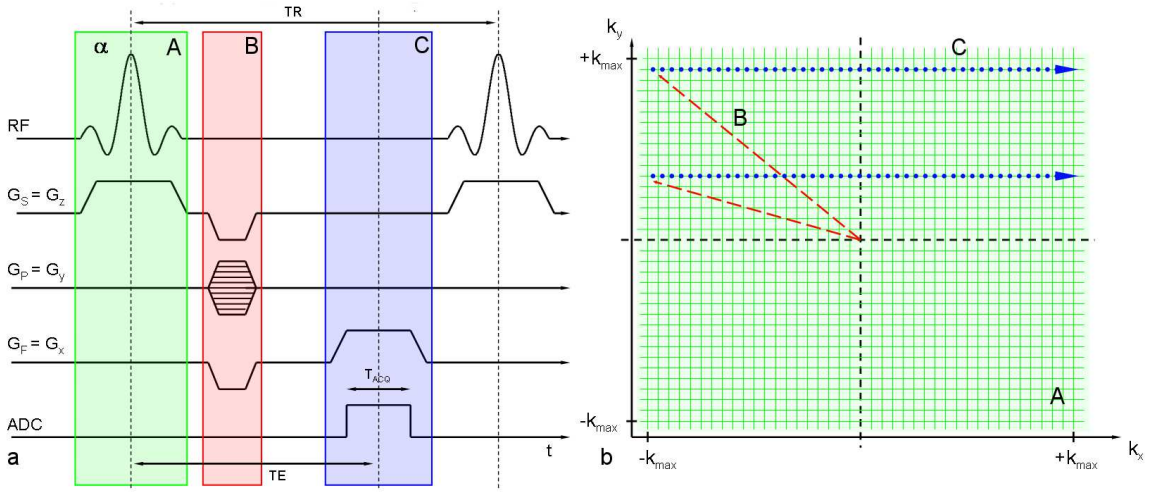

Figure 2.9: Example of pulse sequence timing diagram of a Cartesian gradient echo sequence (a) and correspondent k-space path (b). (A) First, 2D slice excitation takes place along the z axis as the slice selective gradient G_S is switched on during RF excitation. (B) Then, phase encoding and frequency encoding gradients (G_P and G_F) are used to encode the position of a selected k-space line on the xy plane. (C) Finally, a k-space line is acquired (ADC on) while the frequency encoding gradient is switched on. The phase encoding gradient is represented in (a) by a series of horizontal lines to indicate that all k-space lines are sampled at different TRs.

2.2.4 An Example of Non-Cartesian Imaging: 3D Radial

Volumetric 3D datasets can be acquired with two different Cartesian approaches: (1) using a repeated slice by slice excitation until the desired volume is entirely covered or (2) exciting the whole image volume (slab selection) at once. In the latter case, no slice selective gradient is applied during the RF pulses and an independent phase encoding gradient is used to produce additional encoding in slice selection direction.

An alternative to 3D volumetric Cartesian sampling is represented by 3D radial sampling [Wong94]. In this scenario, the three physical gradients G_x, G_y and G_z are applied simultaneously as shown in Fig. 2.10a, thus resulting in a unique gradient vector $\boldsymbol{G}$, Fig. 2.10b.
The orientation of the gradient $\boldsymbol{G}$ in the 3D space can be represented, in spherical coordinates, by a pair of angles: the polar angle θ and the azimuthal angle ϕ. Henceforth, the group of k-space points sampled at each repetition along the direction of $\boldsymbol{G}$ will be referred to as readout and the group of readouts used to acquire the target volume will be referred to as the 3D trajectory. The values of the physical gradients needed to produce the desired $\boldsymbol{G}$ for each specific spherical angle (θ, ϕ) can be calculated as:

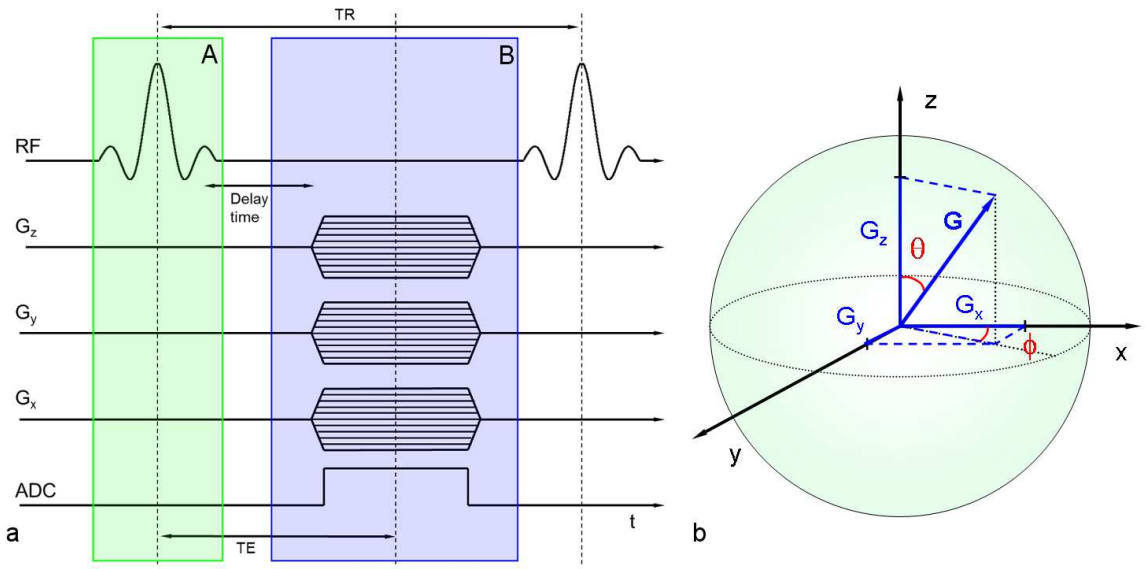

Figure 2.10: Example of a 3D radial sequence timing diagram (a) and spatial visualization of the resulting gradient vector $\boldsymbol{G}$ in the 3D space (b). (A) No slice selective gradients are applied during RF excitation, whereas (B) all three physical gradients are applied simultaneously during the signal sampling interval (ADC on). Each combination of the three gradients defines a specific orientation of $\boldsymbol{G}$ that can be represented with its spherical coordinates (θ, ϕ).

$$\begin{aligned} G_x &= \|\boldsymbol{G}\|_2 \cdot (\sin(\theta)\cos(\phi)) \\ G_y &= \|\boldsymbol{G}\|_2 \cdot (\sin(\theta)\sin(\phi)) \\ G_z &= \|\boldsymbol{G}\|_2 \cdot (\cos(\theta)) \end{aligned} \tag{2.11}$$

In general, 3D radial sampling offers two pronounced advantages compared to Cartesian sampling. This method is: (1) less sensitive to radial undersampling [Lauz 96, Barg 02, Shu 06], which manifests as streaking artifacts, smearing and increased pseudo-noise, rather than coherent aliasing artifacts [Lauz 98] and (2) intrinsically robust with respect to motion artifacts [Steh 04], for displacements oriented perpendicularly to the readout direction are not resolved. A common approach to quantify the effects of both radial undersampling and motion is to compute and analyse the point spread function (PSF) [Bush 11] of the 3D radial trajectory. Ideally, the PSF consists of a Dirac delta function [Dira 47] centered in the center of k-space. However, undersampling and motion artifacts result in the broadening of the central peak as well as in the formation of side lobes. While the former effect is visible as a blurring of the central region, the latter appears as low intensity smeared streaks distributed in radial directions. The analysis of the point spread functions of different radial 3D trajectories can be used to compare their robustness towards both undersampling and motion (Section 3.3.1).

Since the acquired data does not fall on a regular Cartesian grid in k-space, the reconstruction of a 3D radial dataset can not be directly performed with the fast Fourier transform (FFT) [Cool 65]. Even though a point-by-point demodulation using the discrete Fourier transform (DFT) is possible, this kind of approach is extremely slow and therefore of no practical use. The fast alternative method implements an interpolation of each sample onto a Cartesian grid before using the FFT to reconstruct the image and is therefore referred to as gridding [Osul 85, Scho 95, Rasc 99]. The basic idea underneath gridding is to convolve each acquired sample with an appropriate kernel such that the contribution of each sample is distributed among some of its neighbouring points [Jack 91], as shown in Fig. 2.11. One of the most used kernels is based on the Kaiser-Bessel function of the first kind (I_0) [Abra 64], where W defines the width of the kernel and β defines its shape:

$$KB(k) = \begin{cases} \frac{1}{W} I_0 \left[\beta \sqrt{1 - \left(\frac{2k}{W}\right)^2} \right] & \text{for } |k| \leq \frac{W}{2} \\ 0 & \text{otherwise} \end{cases} \tag{2.12}$$

Furthermore, 3D radial trajectories provide an intrinsic oversampling of the center of k-space, whereas the sample distribution in the periphery is much lower (Fig. 2.12a). For this reason, a weighting factor needs to be applied to the sampled points and a sampling density compensation function has to be computed [Pipe 99, Hoge 97] (Fig. 2.12b). The compensation is usually performed for each readout before the gridding

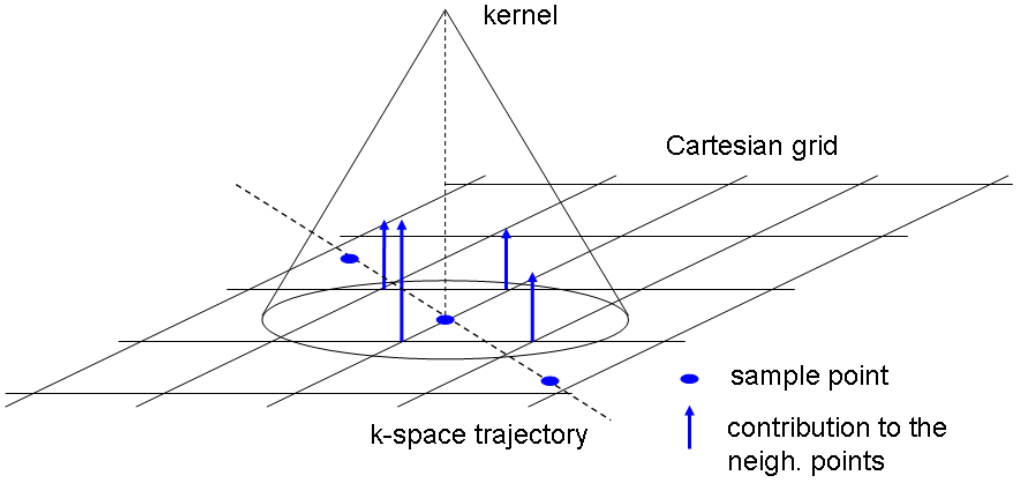

Figure 2.11: The gridding procedure (here depicted for the 2D case) implies the convolution of each sample point with a gridding kernel, such that its contribution to the Cartesian grid is distributed among its neighbouring points according to the width and shape of the kernel.

operation and the complexity of the density compensation algorithm can be highly reduced if the radial readouts are distributed uniformly.

If an isotropic base resolution of N^3 is specified for a Cartesian volumetric acquisition, a total number of N^2 readouts with N samples each is needed to obtain a

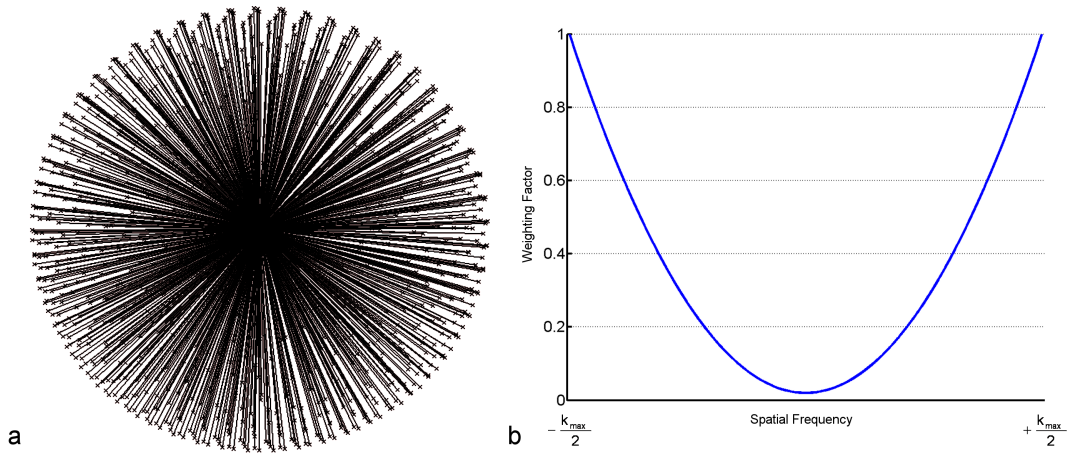

Figure 2.12: (a) Example of 3D radial coverage of k-space. The center of k-space is always oversampled and the density of the sample distribution decreases with the distance. For this reason, a weighting factor must be applied to each 3D radial readout by means of a density compensation function (b).

fully sampled dataset. In the 3D radial case, instead, the surface of the hypothetical sphere containing all readouts must be covered uniformly to satisfy the Nyquist limit and a bigger number of readouts, i.e. $\pi N^2/2$ is needed to ensure a sufficient sample density [Niel 04]. However, since the center of k-space, which contains the relevant information about the image contrast, is always more densely sampled and the undersampling is confined to the periphery, the undersampling does not affect radial acquisitions as much as in the Cartesian case. This particular characteristic makes 3D radial acquisitions intrinsically robust against undersampling, which manifests as streaking artifacts, smearing and increased pseudo-noise (Fig. 2.13b), rather than discrete aliasing artifacts (Fig. 2.13c). The adaptation of the density compensation function to the undersampled case has been extensively studied by Pipe and Menon [Pipe 99] and an iterative solution to calculate a filter for undersampled data was proposed. On the other hand, in a previous study [Niel 04], it was observed that the filter tends to have an asymptotic behaviour that depends on the percentage of undersampling. In this work a rho filter [Niel 04] was used for the density compensation and adapted to the undersampled case by forcing it to an asymptotic value at a specific distance from k-space center, precomputed in relation to the required undersampling ratio.

2.3 Artifacts in MRI

So far the principles of NMR and MRI were described for an ideal physical setup. However, as always, real applications need to deal with the intrinsic imperfections of the hardware used in the MR systems as well as with the natural behaviour of many of the imaged organs, one over all: motion (Section: 1.2).
In this section, a short description of the phenomenon of eddy currents will be given,

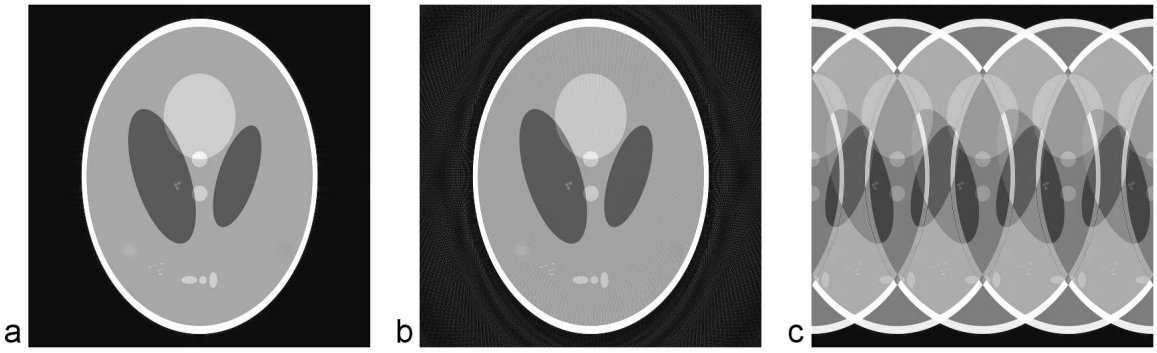

Figure 2.13: Example of undersampling artifacts for the 2D case. A standard Shepp-Logan phantom [Shep 74] (a) was used to compare the different undersampling artifacts for the radial (b) and the Cartesian (c) case. While the resolution of the original fully sampled k-space (a) was 512x512, only 128 readouts, i.e. an undersampling ratio of 0.25 with respect to the Cartesian Nyquist theorem, were used to reconstruct (b) and (c). The image quality obtained with the 2D undersampled radial trajectory is still very good and presents only minor streaking and smearing. On the other hand, the Cartesian case displays discrete aliasing artifacts that heavily compromise the quality of the final image. These images are courtesy of Robert Grimm.

followed by its practical implications with respect to the trajectory chosen for the acquisition and to the induced artifacts in the final image data. Eventually, a description of the motion-induced artifacts will be provided, both for the Cartesian and the 3D radial case.

2.3.1 Eddy Current Effects

Eddy currents are usually defined as currents that are induced in a conducting material, when this is exposed to a changing magnetic field. In turn, eddy currents that are induced in the conducting part of the magnet generate additional varying magnetic fields that can lead to imperfections in the applied gradient schemes.
In general, bSSFP sequences offer superior acquisition speed, signal-to-noise ratio (SNR) and contrast-to-noise ratio (CNR), but are very sensitive to any magnetic field imperfection that can perturb the balanced acquisition scheme. The time-varying magnetic fields of the phase encoding gradients induce eddy currents in the conductive components, and can have a direct impact on the image quality of data acquired with bSSFP [Bier 05]. While a limited amount of dephasing can be refocused during steady-state, abrupt gradient changes may produce sufficient deviations from the dynamic equilibrium to induce large signal fluctuations and, hence, image artifacts. In contrast to linear k-space trajectories, characterized by small variations between consecutive phase encoding steps (Fig. 2.14a), other acquisition schemes may display significant jumps between adjacent steps, thus inducing rapidly changing eddy currents (Fig. 2.14b). In the case of 3D radial trajectories, the evaluation of eddy current effects plays a fundamental role [Steh 04, Picc 11, Bhat 11] and is extensively discussed in Chapter 3.

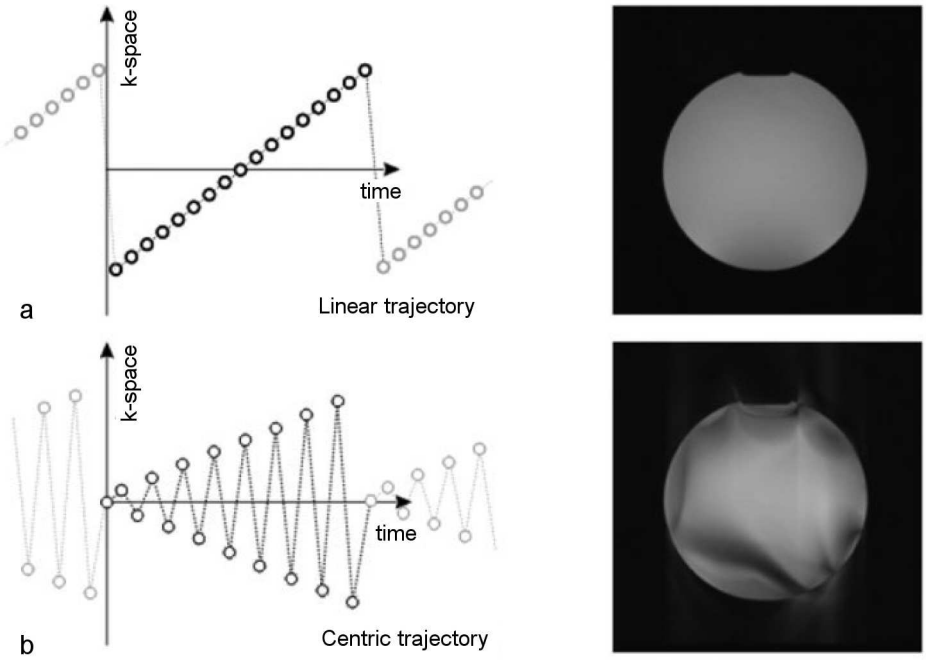

Figure 2.14: Gradient changes in the encoded k-space trajectories during steady state in bSSFP sequences can cause eddy currents related image artifacts. Smooth gradient changes, e.g. in a linear trajectory (a), have no visible effect in the final image quality. In contrast, abrupt gradient jumps (b) can generate eddy currents and cause strong image artifacts. This image was adapted from[Bier 05]

2.3.2 Motion Artifacts

The standard MR image equation (Eq. 2.9) is valid only in a time-invariant scenario, thus, when no motion is present. If motion occurs during the measurement, the magnetization at the location $\boldsymbol{r} = (x, y, z)$ becomes a function of time (τ) [Wood 85, Haac 86, Lauz 93, Xian 93]. In case of affine motion patterns, the deformation of the imaged object can be described by a linear transformation $\mathbf{A}(\tau)$ and a translation $\boldsymbol{r}_{tr}(\tau)$:

$$\mathbf{A}(\tau) = \mathbf{R}(\alpha_1(\tau), \alpha_2(\tau), \alpha_3(\tau)) \cdot \begin{bmatrix} 1 & S_{xy}(\tau) & S_{xz}(\tau) \\ 0 & 1 & S_{yz}(\tau) \\ 0 & 0 & 1 \end{bmatrix} \cdot \begin{bmatrix} S_x(\tau) & 0 & 0 \\ 0 & S_y(\tau) & 0 \\ 0 & 0 & S_z(\tau) \end{bmatrix} \quad (2.13)$$

and

$$\boldsymbol{r}_{tr}(\tau) = (r_x(\tau), r_y(\tau), r_z(\tau)) \quad (2.14)$$

Where $\mathbf{R}(\alpha_1(\tau), \alpha_2(\tau), \alpha_3(\tau))$ represents a 3D rotation at the time τ, $S_{xy}(\tau)$, $S_{xz}(\tau)$ and $S_{yz}(\tau)$ are the 3D shear parameters and $S_x(\tau)$, $S_y(\tau)$ and $S_z(\tau)$ are the scale factors.
Given these considerations, Eq. 2.9 can be rewritten [Steh 05a] as:

$$\begin{aligned} S'(t) &= \int_{\boldsymbol{r}} \rho_0(\boldsymbol{r}_0) \cdot e^{-j\gamma \int_t \boldsymbol{G}(\tau)\cdot(\mathbf{A}(\tau)\boldsymbol{r}+\boldsymbol{r}_{tr}(\tau))d\tau} d\boldsymbol{r}_0 \\ &= \int_{\boldsymbol{r}} \rho_0(\boldsymbol{r}_0) \cdot e^{-j\gamma \int_t \mathbf{A}^T(\tau)\boldsymbol{G}(\tau)\boldsymbol{r}d\tau} \cdot e^{-j\gamma \int_t \boldsymbol{G}(\tau)\boldsymbol{r}_{tr}(\tau)d\tau} d\boldsymbol{r}_0 \end{aligned} \tag{2.15}$$

where $\boldsymbol{r}_0$ is the position at the initial point in time $t = t_0$. According to Eq. 2.15 the consequences of motion during the MR acquisition can be split into two separate effects. The linear transformation $\mathbf{A}(\tau)$ can be interpreted as a modified k-space trajectory $\boldsymbol{k}'(t)$:

$$\boldsymbol{k}'(t) = \gamma \int_t \mathbf{A}^T(\tau)\boldsymbol{G}(\tau)d\tau \tag{2.16}$$

and the translational component $\boldsymbol{r}_{tr}(\tau)$ can be seen as a phase modulation $\beta_{tr}(\tau)$, such as:

$$\beta_{tr}(t) = \gamma \int_t \boldsymbol{G}(\tau)\boldsymbol{r}_{tr}(\tau)d\tau \tag{2.17}$$

The correspondence between translation $\boldsymbol{r}_{tr}$ and phase modulation $e^{-j\boldsymbol{k}\boldsymbol{r}_{tr}}$ is also known as the *Fourier shift theorem*. In general, this means that the correspondent k-space transformation can be computed for each and every linear transformation in k-space. This property of the Fourier transform is referred to as *Fourier similarity theorem*. For instance, in practice, a contraction in image domain corresponds to an expansion in k-space and vice versa. Rotational components are invariant in both domains [Steh 05a].

If motion is not compensated, image artifacts are generated. Two different techniques are commonly used to compensate the motion that occurs during acquisition. The former technique is called prospective motion correction and it is based on the idea that the gradient waveforms G of each TR can be adapted during the acquisition to be pre-compensated with respect to the motion of the object. In this way, the effective phase term of the measured MR signal is ideally kept unchanged during the whole acquisition. This technique requires a knowledge of the motion pattern of the imaged object before the actual data acquisition and, therefore, is not always feasible. The latter technique is referred to as retrospective motion correction. In this case motion can be computed after the actual data acquisition and used to correct the acquired data during image reconstruction. The retrospective approach significantly increases the computational load during image reconstruction because the motion corrected data often needs to be regridded to fall on a regular Cartesian grid. Yet, in a non-Cartesian approach, the regridding step is already required. A retrospective correction would therefore not add any additional computational load. For example, the phase modulation $\Delta\beta_{tr}$ corresponding to a simple rigid translation $dr_{tr} = (dx, dy, dz)$ can be easily computed according to the *Fourier shift theorem* as:

$$\Delta\beta_{tr} = \frac{2\pi}{N} \cdot (dx \cdot \sin(\theta)\cos(\phi) + dy \cdot \sin(\theta)\sin(\phi) + dz \cdot \cos(\theta)) \tag{2.18}$$

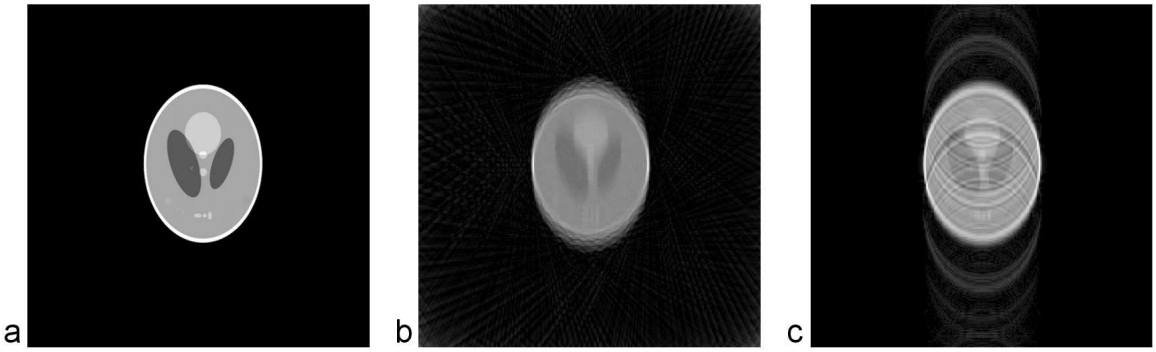

Figure 2.15: Example of motion artifacts in the 2D case. A standard Shepp-Logan phantom [Shep 74] (a) was used to compare the different motion artifacts for the radial (b) and the Cartesian (c) case. The resolution of all datasets was 256x256. The datasets in (a) was acquired without motion, while in (b) and (c) a sinusoidal motion was simulated in the superior-inferior direction with peak amplitude of 4 pixels and periodicity of 16 / acquisition. In radial scanning the motion artifacts appears as concentric streaks in all direction with a relatively low artifact amplitude. On the other hand, the Cartesian case displays strong discrete ghosting artifacts perpendicular to the readout direction. These images are courtesy of Johannes Churt.

where dx, dy, dz are the displacements measured in pixels and N is the number of samples along one readout. As in Section 2.2.4, θ and ϕ represent the polar and the azimuthal angle, respectively.

2.4 Current State of the Art in Coronary MRI

The final section of this chapter gives a short but comprehensive description of the state of the art of coronary MR imaging. This description is based on some of the most recent publications on the topic, such as [Haus 08, Stub 07, Mann 07, Kell 08]. The use and utility of coronary MRI has been investigated since the 1980s [Lieb 84, Paul 87] and the technique has constantly improved since then. However, for successful coronary MRI data acquisition, several major limitations still need to be overcome.

2.4.1 Contrast Enhancement

For a suitable visualization of the coronary arteries, an enhanced contrast between the oxygenated blood flowing in the coronaries and the surrounding myocardial tissue is essential. In coronary MRI, contrast enhancement can be obtained not only by the administration of contrast agents, i.e. exogenous enhancement, but also by using special preparation pulses in the MR sequence, i.e. endogenous enhancement. In case of exogenous enhancement, gadolinium (Gd) based contrast agents are administered intravenously and cause a reduction in the T1 of blood. With the use of an inversion pre-pulse, before the imaging part of the sequence, the signal of the myocardium can be strongly attenuated [Hofm 99]. If extracellular contrast agents are used, data

collection must happen during the first-pass phase and, therefore, breath-holding is mandatory. However, a prolonged acquisition window, and thus free breathing acquisitions, can be obtained using intravascular contrast agents [Li 98, Hube 03].
Endogenous contrast enhancement can be obtained mainly using specific preparatory pulses, such as: fat saturation [Rose 84], magnetization transfer contrast [Li 93], and T2-preparatory pulses [Wrig 91, Brit 95, Botn 99]. In particular, T2-preparatory pulses suppress the deoxygenated venous blood and are more widely used for coronary imaging. In principle, these methods take advantage of the natural differences in T2 between blood and myocardial muscle (Tab. 2.1). First, the magnetization is flipped onto the transverse plane and experiences T2 decay. After that, a so-called 90° tip-up pulse is applied. As the T2 of the muscular tissue is shorter than the T2 of the arterial blood, if the sampling is performed at the right timing (TE) after T2 preparation (Fig. 2.16), the final result is a reduced signal from the myocardium. These techniques are referred to as bright-blood imagining techniques as they provide

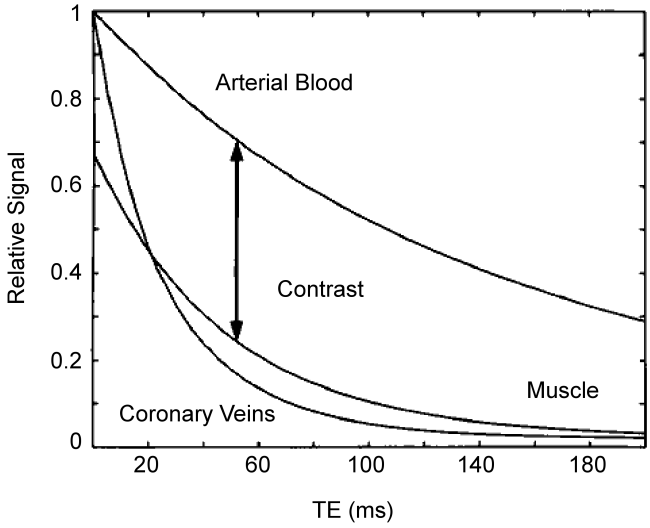

Figure 2.16: Simulated steady state signal as a function of TE resulting from T2 preparation. When the acquisition is performed at the right TE, the contrast between arterial blood, myocardial muscle and venous structures can be highly increased. This image was adapted from[Brit 95]

bright coronary lumen in contrast with dark surrounding myocardial tissue. Nevertheless, black-blood coronary MRI is also used in practice [Stub 01], especially to visualize the coronary vessel wall.

2.4.2 Localization and Whole-Heart Imaging

As mentioned already in Chapter 1, coronary arteries have a complex geometry and are usually tortuous and small in diameter. As a consequence, a sufficient imaging volume needs to be acquired to encompass the targeted vessel or vessels. On the other hand, increased volume coverage obviously implies increased total acquisition time

or decreased spatial resolution. The two typical approaches, concerning the volume coverage, are referred to as volume targeting and whole-heart imaging.
Volume targeting [Born 95, Stub 99b], i.e. the precise pre-localization of the target coronary vessel to be acquired, is achieved during the scout scanning steps, before the actual acquisition. In this case, low-resolution localization scans have to be performed with a setup identical to that of the actual high-resolution acquisition. The reduced target volume allows short acquisition times for the high-resolution scan. The targeted acquisition takes also advantage of the enhanced contrast given by the blood inflow in a relatively thin slab. Nevertheless, the targeting procedure is highly operator-dependent and complicated scout scans can increase the total examination time, thus neutralizing the advantages of a fast acquisition. In addition, only a limited access to the distal part of the coronaries can be achieved with this approach.
Whole-heart imaging [Steh 05b, Haus 08, Picc 12], on the other hand, allows the acquisition of the entire volume of the cardiac organ. In this case, the localization of the coronaries is obtained by reformatting the acquired dataset with a post-processing software tool. This technique has the great advantage of minimizing the operator's interaction for the localization and to potentially assess the whole length of the coronary vessels. The acquisition time for a whole-heart dataset is naturally larger than that for a smaller targeted volume. Several acceleration techniques, such as parallel imaging [Prue 01, Gris 02] and compressed sensing [Lust 07] have been developed in the last years and applied to reduce the acquisition time of whole-heart coronary MRI.

2.4.3 Navigator-Gating

Coronary arteries are constantly subjected to both cardiac and respiratory motion. A description of the cardiac and respiratory motions was given in Section 1.2.
In order to minimize the motion artifacts due to the periodic contraction of the heart, coronary MRI acquisitions are typically performed within a short time window during the phase of minimal cardiac motion. In adult subjects, this time window usually corresponds to the so called mid-diastolic phase (Fig. 1.4(D)). The phase of minimal cardiac motion is normally assessed with a 2D cine preparation scan, before the actual data acquisition. A subject-dependent delay time with respect to the R-wave (Fig. 1.4) is then selected to trigger data acquisitions.
As previously mentioned, the amount of MRI data needed to cover the entire coronary tree (or even a specific coronary artery) with sufficient resolution and the current speed limitations of the MR scanners do not allow to acquire the data within a fraction of an heartbeat. Hence, the acquisition is interleaved across several heartbeats. In this case, the cardiac motion due to respiration must also be taken into account. Even though breath-hold acquisition is certainly a possibility, this approach has some limitations (Section 1.4). The state of the art approach to compensate for respiratory motion in free-breathing coronary MRI, requires the use of a beam-navigator [Ehma 89]. A software navigator is simply an additional and quick preparation pulse, acquired on a moving structure, right before or after the actual data acquisition. The respiratory beam-navigator is usually placed on the dome of the right hemidiaphragm (Fig. 2.17(a)) and provides a feedback on the respiratory position of the

diaphragm, relative in time to the data acquisition window [McLe 02]. The feedback is provided along the major direction of respiratory motion, namely the SI direction (Section 1.2.2). A narrow acceptance window is applied to the signal of the navigator in case of respiratory gating (red window in Fig. 2.17(b)). Hence, only the interleaves acquired within the same respiratory phase, e.g. end-expiration, are accepted and used for the reconstruction of the final data, while all the other interleaves are discarded and re-acquired. In addition, prospective motion compensation (Section 2.3.2) can be performed on interleaves acquired within the acceptance window, if the position of the diaphragm is assessed before the data acquisition window [Dani 97]. It has been suggested [Wang 95] that a linear correlation factor exists, which approximates the linear relation of the SI position of the diaphragm and the two large coronary arteries. Thus, the feedback provided by the navigator is translated into an offset of the RF slice position, taking the correlation factor into account. Although major improvements in navigator-gated coronary MRI have been achieved in recent years [Desh 06, Nguy 09, Jhoo 10], there are still a number of outstanding problems that limit the clinical usage of this technique. 1) Respiratory gating in navigator-gated acquisitions performs with an acceptance rate of less than 40%, in many cases. 2) An ill-positioned navigator [Stub 99a], as well as irregularities on the respiratory pattern of the patient [Tayl 99] might lead to extended examination times. In cases where the variation in respiratory motion is very large, adaptive windowing techniques [Desh 06, Jhoo 10] are not reliable and the acquisition might not be completed. 3) The accuracy of the motion detection performed with the navigator is sub-optimal, as the fixed correlation factor does not take the inter-patient variability into account [Dani 97, Mogh 12] and is adversely affected by hysteretic effects [Nehr 01] and temporal delays [Spue 02].

2.4.4 Self-Navigation

Innovative techniques, implementing respiratory self-navigation, have recently been introduced to overcome the drawbacks of navigator-gated acquisitions [Steh 05b, Lai 08]. As shown in Fig. 2.18, the aim of these methods is to extract the information on the respiratory motion directly from the readouts acquired for imaging, thus eliminating the need for the external beam-navigator. More specifically, these techniques try to achieve a reliable assessment of the position of the heart in readouts oriented along the SI direction, acquired at the beginning of each interleave. This information is extracted from the 1D FFT of these readouts, which can be interpreted as projections of the imaging volume onto the SI axis. The SI projection of each interleave is compared with a reference projection acquired at the beginning of the examination, using a center of mass approach [Steh 05b] or cross-correlation [Lai 08] to determine the respiratory offset. This enables to perform the motion correction directly in k-space during image reconstruction (Section 2.3.2). These techniques promise: 1) an acceptance rate of 100%; 2) simplified examination planning and an a priori knowledge of the duration of the acquisition regardless of the individual respiratory patterns; and 3) improved accuracy of the motion compensation.
The implementation of new algorithms for image acquisition, reconstruction and res-

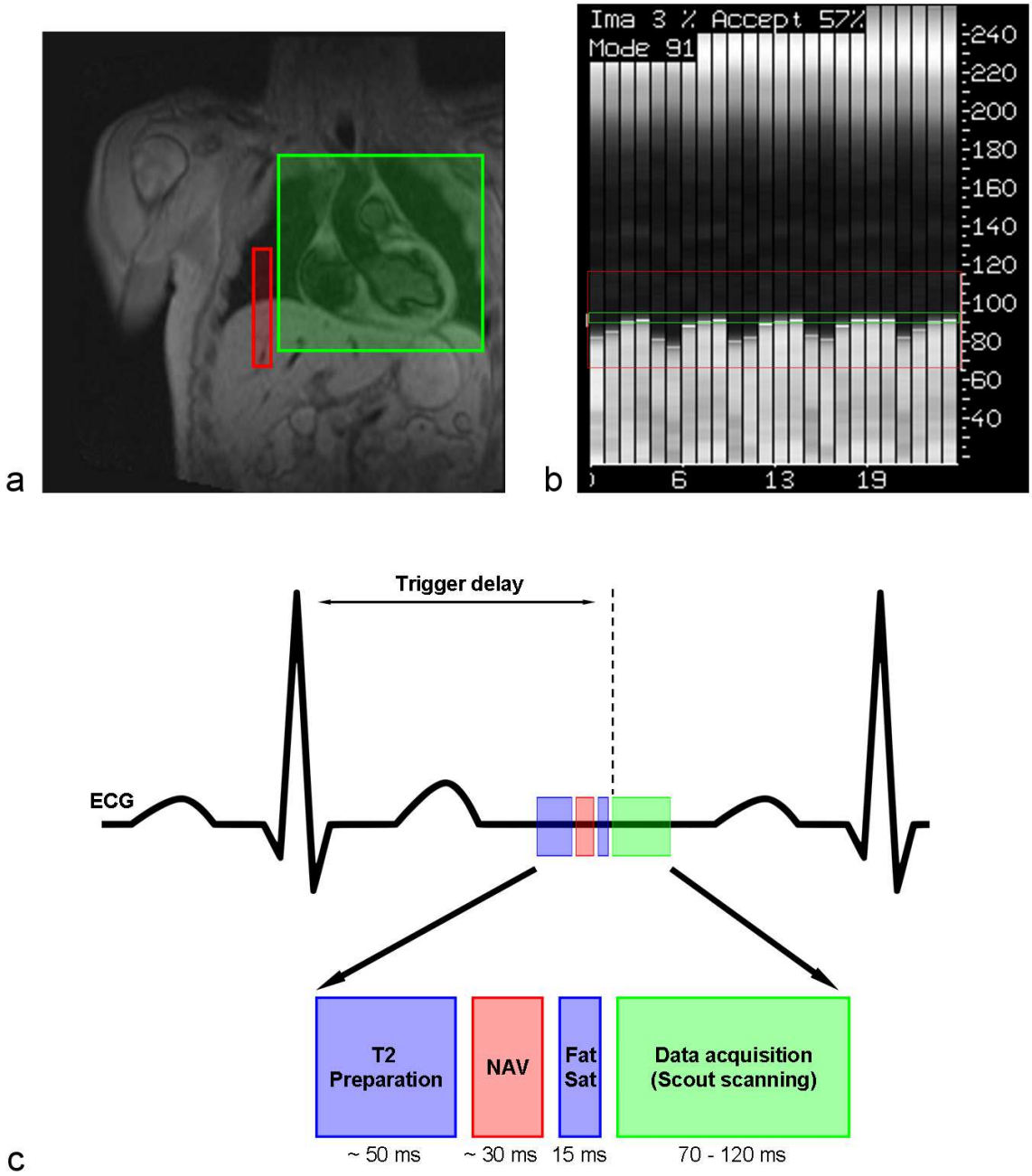

Figure 2.17: Schematic representation of a navigator-gated acquisition. The field of view (FOV) of the navigator is usually placed at the lung-liver interface (a) and is represented here by the red rectangle. The imaging FOV, in the case of a whole-heart acquisition, is represented by the green square. An automatic algorithm detects the position of the liver-lung interface over time at every heartbeat (b). A small acceptance window is defined, usually in end-expiration (the thin and green horizontal rectangle in (b)). In this example, data acquisition is performed right after the navigator acquisition (c). The interleaves acquired when the navigator signal falls outside the acceptance window are discarded and re-acquired. T2 preparation pulses are usually placed before the navigator acquisition, to affect also the contrast of the navigator signal. Fat-saturation is placed right before the actual data acquisition for maximum effectiveness (c).

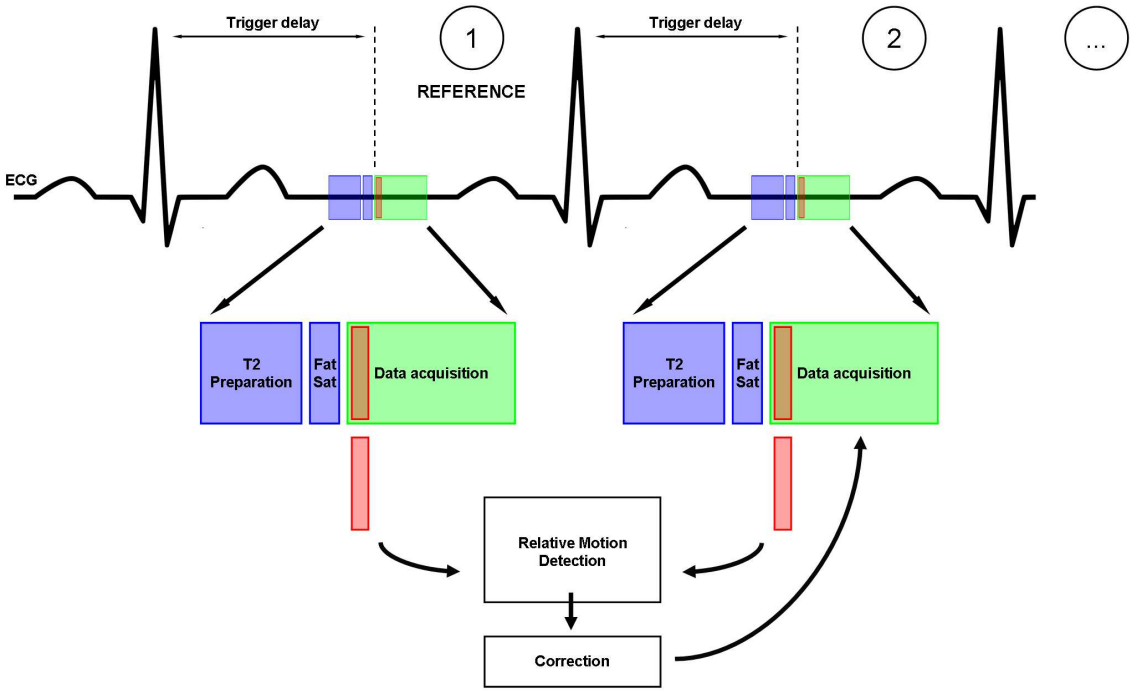

Figure 2.18: Schematic representation of self-navigation. The navigator acquisition is no longer needed and the information on the respiratory motion is extracted directly from the group of readouts used for imaging. This intrinsic motion information is depicted here as a red rectangular box inside the green box. The relative respiratory motion is computed by comparing each interleave with a reference (usually from the data acquired within the first heart beat). A relative correction can be computed and applied on-line to data acquired during the current heart beat, before image reconstruction. With self-navigation, all interleaves are used to form the final dataset and, thus, 100% scan efficiency is achieved.

piratory motion detection in the field of self-navigation is one of the central themes of the following chapters.

Chapter 3

Interleaved 3D Radial Whole-Heart MRI with Minimal Eddy Currents

This chapter describes a novel 3D radial trajectory based on a spiral phyllotaxis pattern, which combines both an overall uniform distribution of the acquired readouts and minimal eddy currents. The described trajectory is also intrinsically prepared for self-navigated cardiac MRI. These features are assessed in comparison with two alternative 3D radial trajectories, previously known in literature and based on two different implementations of an Archimedean spiral pattern. The image quality achieved with the novel approach is assessed both in phantoms and in vivo and compared with images acquired with one of the Archimedean trajectories. In vivo, the improvements obtained with the novel trajectory are evaluated for navigator-gated whole-heart coronary MRI acquisitions in 6 healthy volunteers. Major parts of this chapter are currently published in [Picc 11].

3.1 Motivations

3.1.1 Whole-Heart Acquisition with 3D Radial Trajectories

As described in Chapter 1, the anatomy of the heart is very complex and the location and orientation of the heart differ within the thorax is different for each individual. Until now, only experienced operators are able to precisely localize the volumes of interest and to perform a comprehensive cardiac MR examination. As a consequence, the option to acquire a 3D volume that covers the whole heart with high and isotropic resolution is a highly desirable goal [Born 95]. In such configuration, some

of the preparatory steps of a cardiac examination are obsolete, since the complexity of slice planning is significantly reduced [Stub 99b]. In addition, it is possible to reconstruct views with arbitrary orientations off-line, e.g. curved reformats along the coronary vessels. As mentioned in Section 2.2.4, in a 3D scenario, radial sampling offers at least two pronounced general advantages compared to Cartesian sampling. This acquisition approach is intrinsically more robust with respect to both undersampling [Lauz 96, Barg 02, Shu 06] motion artifacts [Steh 04].

Cardiac imaging is performed in the presence of periodic contraction of the heart as well as respiratory motion. As described in the previous chapters, the contraction of the heart is frozen in a specific data acquisition window of the cardiac cycle via ECG triggering [Kim 01b], and respiratory motion is usually reduced with the use of respiratory gating (Section 2.4.3). This can be referred to as a highly interleaved data acquisition scheme. As mentioned in Section 2.4.4, in the case of 3D radial MRI, information about the respiratory motion of the heart can be extracted directly from the readouts that are oriented along the superior-inferior direction. In this scenario, rapidly changing gradient moments have to be carefully avoided to prevent eddy current effects when a bSSFP sequence is used for acquisition (Section 2.3.1). Furthermore, as described in Section 2.2.4, image reconstruction methods for radial MRI involve gridding and sampling density compensation. The complexity of the density compensation algorithm can be reduced if the radial readouts are distributed uniformly. Thus, in summary, a 3D radial trajectory that is optimally suited for cardiac MRI features: (1) interleaving properties that minimize eddy current effects and (2) uniform distribution of the readouts.

3.1.2 Spiral Phyllotaxis Pattern

In botany, the word *phyllotaxis* indicates the arrangement of leaves on a stem. The pattern known as "spiral phyllotaxis" is an eye-catching arrangement, consisting of two sets of spirals forming a lattice. This pattern can be identified in a number of plants and flowers (Fig. 3.1), where the numbers of visible clockwise and counter-clockwise spirals are typically associated with two successive elements, Fs_n and Fs_{n+1}, of the Fibonacci sequence:

$$Fs_n = Fs_{n-1} + Fs_{n-2}, \text{ with } Fs_0 = 0 \text{ and } Fs_1 = 1. \tag{3.1}$$

In these cases, as a new leaf is formed around the center of the spiral, the azimuthal angle between its position and that of the previous leave is always close to the golden angle. Extensive studies on spiral phyllotaxis and its mathematical properties have been reported in many scientific fields within natural sciences [Doua 96], theoretical sciences [Math 74, Voge 79, Rldl 82, Fowl 92] and also engineering applications [Li 09]. The use of sampling strategies and reconstruction techniques involving Fibonacci numbers [Clin 99] and the golden angle [Chan 09, Wink 07, Lu 08] have also been applied to MRI.

Figure 3.1: Examples of the spiral phyllotaxis pattern in nature. This peculiar arrangements of leaves and petals can be identified in several different plants and flowers and represents a natural optimization of their spatial distribution. In the cactus on the left side of the image, elements of the two eye-catching sets of spirals running clockwise (red) and counter-clockwise (blue) are highlighted. The pictures of flowers are courtesy of Ana Paula Piccini.

3.1.3 Research Contributions

In the present chapter, a novel 3D radial trajectory, based on a spiral phyllotaxis pattern is introduced, which integrates both an overall uniform distribution of the readouts and optimized interleaving properties. This trajectory is intrinsically prepared for self-navigated cardiac MRI. These features of the new approach were theoretically assessed in comparison with two well-established alternative 3D radial trajectories, based on two different implementations of an Archimedean spiral pattern. In addition, the image quality achieved with the novel trajectory in phantoms was compared with that of images acquired with one alternative trajectory. Both radial acquisitions were reconstructed with identical uniform density compensation. Finally, the experiments were repeated for navigator gated whole-heart coronary MRI in 6 healthy volunteers.

3.2 Theory

3.2.1 Archimedean Spiral Pattern

In a straightforward approach, the implementation of a 3D radial trajectory can be based on an Archimedean spiral pattern [Wong 94, Niel 06]. This specific pattern can be mathematically described in a scenario where the radius r is kept constant and the azimuthal φ_n and polar angle θ_n of a readout $n = 1, 2, \ldots N$ going through the center of k-space are computed as follows [Saff 97]:

$$r = const. , \tag{3.2}$$

$$\varphi_n = \left(\varphi_{n-1} + \frac{3.6}{\sqrt{N\,(1 - h_n^2)}} \right) \bmod (2\pi) , \tag{3.3}$$

$$\theta_n = \arccos(h_n), \tag{3.4}$$

with

$$h_n \;=\; -1 + \frac{2n}{N} \;\text{ and }\; n \;\in\; [1, N]\,. \tag{3.5}$$

In the Archimedean spiral pattern, the revolutions of the origins of the linear readouts on the surface of a sphere in k-space get both tighter and more densely sampled in proportion to the total number of readouts N. This approach provides a simple formulation for a 3D radial trajectory and allows for a highly uniform distribution of the readouts [Saff 97]. In this work, the definition of uniform sampling in 3D given in [Steh 05b] and based on the based on the relative standard deviation (RSD) of the distances $d_{i,j}$ between the origin point of each radial readout and its four closest neighbours was used:

$$RSD \;<\; 10\%\;, \tag{3.6}$$

The complete formulation of the RSD is given in Section (3.3.1). An example of the overall distribution of the readouts on the half sphere is displayed in Fig. 3.2 both in a top view and angulated view.

3.2.2 Implementation of the Spiral Phyllotaxis Pattern in 3D

In the year 1979 the German physicist H. Vogel published a closed formula for the spiral phyllotaxis pattern in 2D [Voge 79]. In order to provide a dense and uniform sampling for 2D fast cardiac MRI sequences, a solution featuring Vogel's formula had already been proposed in [Clin 99], but limited to the frequency-encoding plane. In the current work, the formulation in 2D polar coordinates of the original pattern was directly translated into 3D spherical coordinates [Picc 11]:

$$r \;=\; const.\;, \tag{3.7}$$

$$\varphi_n \;=\; \frac{(2\pi)}{360} \cdot n \cdot \varphi_{gold}\;, \tag{3.8}$$

$$\theta_n \;=\; \frac{\pi}{2} \cdot \sqrt{\frac{n}{N}}\;. \tag{3.9}$$

While the radius, r, is constant, the azimuthal angle φ_n of a readout $n = 1, 2, \ldots N$ going through the center of k-space is proportional to the golden angle, $\varphi_{gold} = 137.51°$. As done for the radius in the original 2D formulation, the polar angles θ_n are calculated in proportion to the square root of n over the total number of readouts N that are used to sample the whole 3D space. An example of the overall distribution of the readouts on the half sphere is displayed in Fig. 3.3 both in a top view and angulated view.

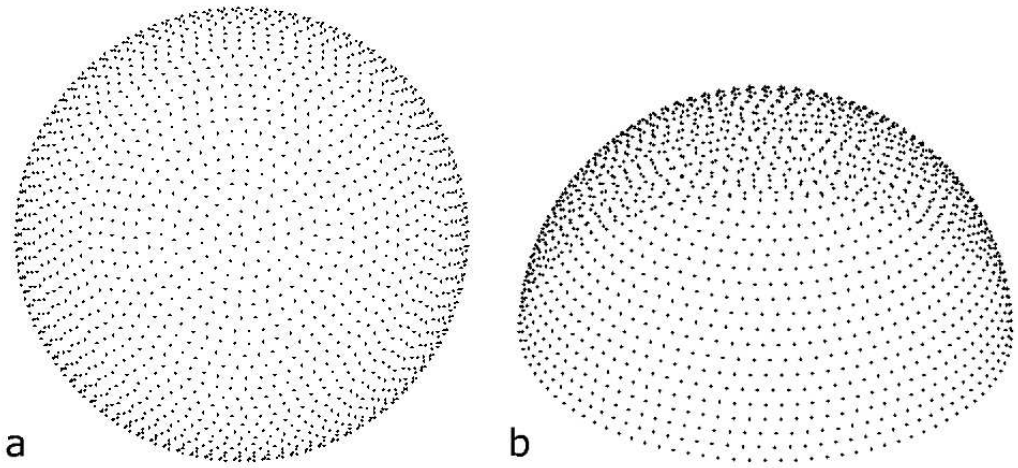

Figure 3.2: Distribution of the origins of the readouts in a 3D Archimedean spiral pattern with $N = 1600$ radial readouts in top view (a) and angulated view (b). Each dot represents the origin of a linear readout going through the center of k-space. This approach provides a highly uniform distribution of the readouts.

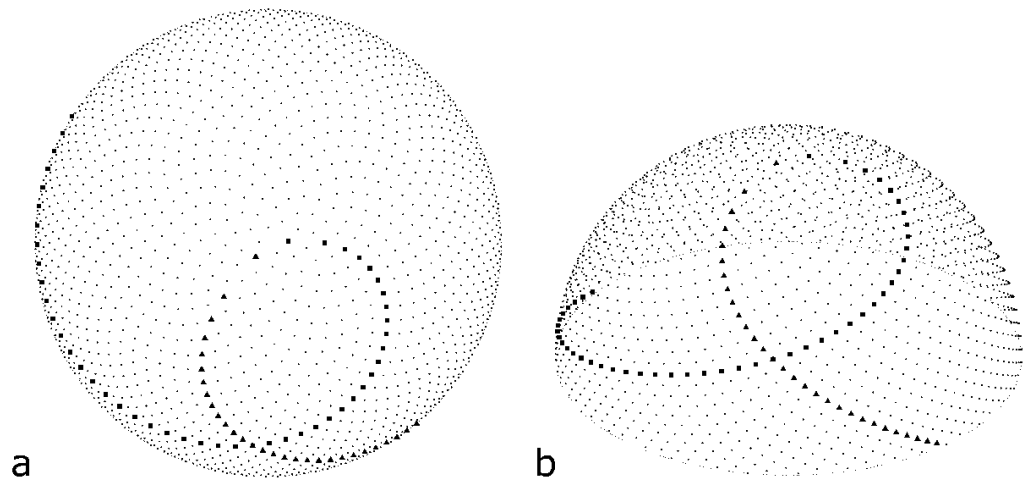

Figure 3.3: Distribution of the origins of the readouts in a 3D spiral phyllotaxis pattern with $N = 1600$ radial readouts in top view (a) and angulated view (b). Each dot represents the origin of a linear readout going through the center of k-space. The elements of two eye-catching spirals running clockwise (squares) and counter-clockwise (triangles) are highlighted in the plot. These spirals are associated with interleaving the trajectory with 34 and 55 interleaves, respectively, which are two successive Fibonacci numbers.

3.2.3 Interleaving Techniques

Since cardiac MRI data acquisition is performed in a highly interleaved fashion, the 3D radial trajectory needs to be adequately prepared. Thus, a total number of readouts $N = M \cdot P$ can be straightforwardly interleaved in M interleaves with P readouts per interleave just by assigning every M^{th} readout to a specific interleave. This interleaving technique maintains the overall uniform distribution of the total number of readouts on the sphere, but can result in large consecutive phase encoding steps of the gradient moments and, thereby, in eddy currents. An alternative approach, in the context of 3D radial MRI, was recently proposed in [Steh 04] to avoid eddy current effects with self-navigated cardiac MRI. In that solution, at first the pattern of a single interleave is constructed, e.g. an Archimedean spiral with P readouts. Then, the single interleave is rotated M-times with a constant azimuthal angle. Although this leads to an increased density of readouts originating from the top of the sphere, the displacement of successive readouts within one interleave is significantly reduced. Henceforth, the Archimedean spiral pattern interleaved with the straightforward method will be referred as *Type A*, while the pattern interleaved with the rotation-based method will be referred as *Type B*. In addition, when referring to the interleaved spiral phyllotaxis pattern, the straightforward interleaving method is always to be intended. In Fig. 3.4, columns (a) and (b) illustrate the differences between the *Type A* approach and the *Type B* approach, respectively. In comparison, the interleaving properties of the spiral phyllotaxis pattern are plotted in columns (c) and (d). While in case of an Archimedean spiral pattern, the uniform distribution of the readouts excludes small displacements of successive readouts, the interleaved spiral phyllotaxis pattern integrates both features. If the number of interleaves is a Fibonacci number (Fig. 3.4, column (d)), then the trajectory self-arranges in such a way that the displacements between successive readouts within one interleave are minimized [Math 74]. Intrinsically, the actual rotation angle between successive interleaves is the golden angle.

3.3 Materials and Methods

3.3.1 Theoretical Evaluation

The novel 3D spiral phyllotaxis pattern was compared with both the Archimedean spiral patterns of *Type A* and *Type B*, using simulations and analyses performed in Matlab 7.3 (The MathWorks Inc, Natick, MA, USA). First, the general uniformity of the distribution of readouts was evaluated. For this purpose, the *RSD* of the distances $d_{i,j}$ between each origin point i and each of its four closest neighbours j was calculated for all trajectories:

$$RSD = \frac{\sqrt{\frac{1}{N \cdot 4} \cdot \sum_{i=1}^{i=N} \sum_{j=1}^{j=4} (d_{i,j} - \mu_d)^2}}{\mu_d}, \tag{3.10}$$

with μ_d being the mean distance, defined as:

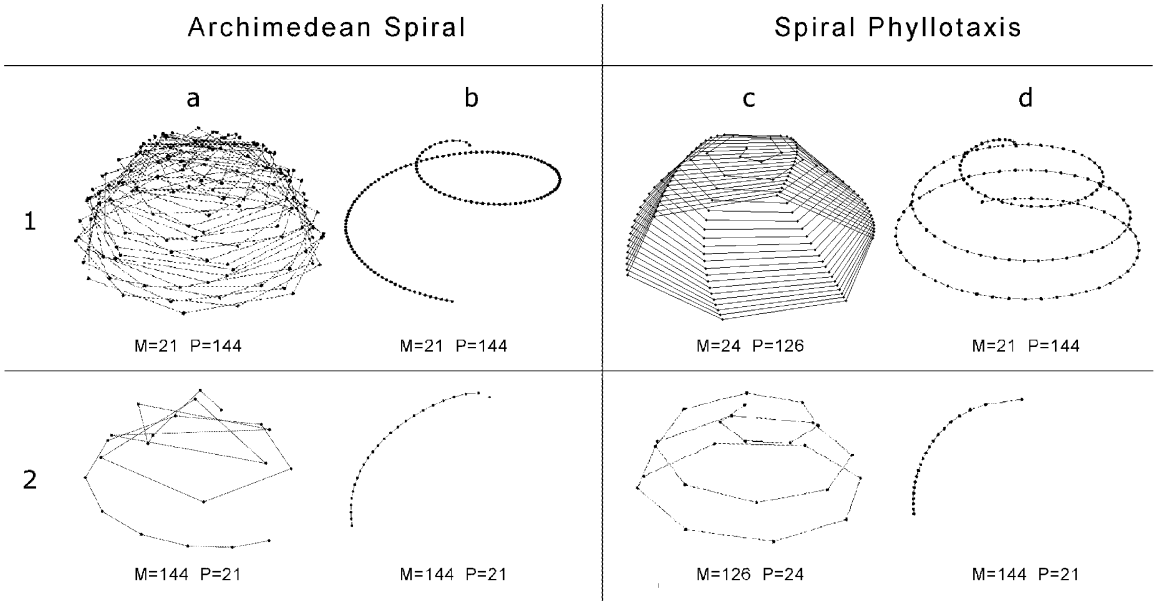

Figure 3.4: Visualization of the differences of the interleaving techniques of the *Type A* uniform Archimedean spiral pattern in the columns (a) and the *Type B* non-uniform Archimedean spiral pattern (b) in comparison to the properties of the spiral phyllotaxis pattern in the columns (c) and (d). Each plot represents one of M interleaves with P readouts out of a total number of $N = M \cdot P = 3024$. In row (1) M is much smaller than P, whereas row (2) represents the highly interleaved case with M larger than P. The dots represent the origins of the linear readouts which run through the center of k-space. Straight lines connecting successive readout origins represent the change of the gradient moment from one readout to the next. In the case of the Archimedean spiral patterns, either an overall uniform distribution of the readouts is achieved with the straightforward interleaving approach (*Type A*) of (a.1) and (a.2) or the displacement of successive readouts is minimized with the rotation-based approach (*Type B*) of (b.1) and (b.2). Unless the number of interleaves is a non-Fibonacci number (c.1, c.2) the spiral phyllotaxis pattern, straightforwardly interleaved, integrates both features (d.1, d.2). In this latter case, the trajectory self-arranges in such a way that the displacements between successive readouts within one interleave are minimized and the rotation angle between successive interleaves equals the golden angle.

$$\mu_d \;=\; \frac{1}{N \cdot 4} \cdot \sum_{i=1}^{i=N} \sum_{j=1}^{j=4} d_{i,j} \;. \tag{3.11}$$

The *RSD* was calculated for a constant number of readouts $P = 34$ per interleave, while the number of interleaves was increased following the Fibonacci series, with $M = [\ 1,\ 2,\ 3,\ 5 \quad \ldots \quad 233,\ 377\ ]$.

The aim of a second analysis was to provide a measure of the expected eddy current effects associated with each trajectory. Thus, the average angular distance in radians between successive readouts within one interleave was calculated. This measure was performed for each trajectory with a constant number of readouts $P = 34$ per interleave for an increasing number of interleaves $M = [\ 1,\ 2,\ 3,\ 5 \quad \ldots \quad 233,\ 377\ ]$.

Finally, the point spread function (PSF) (Section 2.2.4) of the radial 3D trajectory based on the Archimedean spiral pattern non interleaved and that of the trajectory based on the radial 3D spiral phyllotaxis pattern were compared. Therefore, k-space input data with 22% radial undersampling (Section 2.2.4) and $N = 12818$ of both trajectories were initialized with constant values and were reconstructed using the same density compensation. The signal distribution of the two PSFs was visually analysed in three dimensions. Furthermore, the signal intensity of the central peaks and the mean signal intensities in two regions of interest comprising 400 pixels were compared in the central slice of a total number of 384 transversal slices with a 384 pixels squared matrix corresponding to a $2 \cdot FOV$ representation.

3.3.2 MR Experiments

The presented 3D radial trajectory based on the spiral phyllotaxis pattern was implemented on a 1.5 T MAGNETOM Avanto scanner (Siemens AG, Healthcare Sector, Erlangen, Germany) with software version B15A and was compared with an established implementation of the Archimedean spiral pattern [Saff97, Niel06] in phantoms and in vivo. Radial 3D data acquisition was performed with: 1) the uniform Archimedean spiral pattern, non interleaved, as the reference data, 2) the interleaved Archimedean spiral pattern of *Type A*, and 3) the new 3D spiral phyllotaxis interleaved pattern. In all experiments, non-selective, T2-prepared, fat-saturated, balanced SSFP imaging was performed with the following parameters: TR/TE 3.0/1.52 ms, FOV $(220\ \text{mm})^3$, matrix 192^3, measured voxel size $(1.15\ \text{mm})^3$, flip angle 90° and receiver bandwidth 898 Hz/Px (Hertz/Pixel). A total of 12818 radial readouts were acquired in 377 interleaves for an overall undersampling ratio of 22% with respect to the Nyquist limit in the 3D radial case. Two-fold oversampling was applied in the readout direction to automatically avoid foldover artifacts [Lauz98]. Image reconstruction was performed online with a gridding algorithm [Pipe99] featuring identical density compensation settings [Niel07] for all protocols (Section 2.2.4).
Experiments on a multi-purpose phantom were performed only with the body coil. Artifacts produced by eddy current effects in the interleaved Archimedean spiral and

the interleaved spiral phyllotaxis were evaluated by qualitative comparison with the reference image data.
Whole-heart coronary imaging was performed in 6 healthy volunteers after informed consent was signed. A total of 12 elements of a body matrix coil (anterior) and the spine matrix coil (posterior) were selected for the acquisitions. The reference trajectory was acquired in a segmented fashion, from the top of the sphere to the equator, to minimize the changing gradient moments. The measurements were ECG-triggered and a subject-dependent delay was applied in order to position the data acquisition window in late diastole, where cardiac motion is expected to be minimal [Kim 01b]. To avoid artifacts caused by respiratory motion, gating was performed with a crossed-slice spin echo navigator placed on the dome of the right hemidiaphragm. The acceptance window of the navigator (Section 2.4.3) was set to 5 mm.

3.3.3 Image Quality

To extract the right coronary artery (RCA), the isotropic image data were reformatted during post-processing with the curved cut tool in *syngo 3D* (Siemens AG, Healthcare Sector, Erlangen, Germany). The in vivo images were quantitatively evaluated for SNR, CNR and vessel sharpness of the RCA, as described in [Li 01]. For SNR and CNR, the mean blood signal intensities were measured in a cross-sectional plane of the ascending aorta at the RCA origin, while myocardial mean signal intensities were taken at the anterior portion of the left ventricular wall, inferior to the left anterior descending artery (LAD). Regions of interest for the measurement of noise were carefully placed in sections of the lungs with minimal streaking artifacts. Although it was not possible to generally avoid residual contribution of artifact noise, SNR and CNR were nevertheless considered a general image quality measure. The inverse of the average distance between the 20% and the 80% of the signal intensity profiles on both sides of a user-selected line perpendicular to the axes of the RCA was used for the calculation of the vessel sharpness [Li 01].

3.4 Results

3.4.1 Theoretical Evaluation

The plot of the *RSDs* of the alternative implementations of the interleaved Archimedean spiral pattern in Fig. 3.5 confirms that for more than $M = 34$ interleaves the uniformity of the distribution of readouts of the *Type A* pattern is very high with an *RSD* of less than 2%, whereas the uniformity of the *Type B* pattern decreases with an increasing number of interleaves. Even with $M = 34$ interleaves the *RSD* is already $> 7\%$. In contrast to this, the *RSD* of the spiral phyllotaxis pattern is $6 - 7\%$ regardless of the number of interleaves.

For the average distance of successive readouts in one interleave, the performance of the two Archimedean spiral patterns is reversed, Fig. 3.6. For the *Type A* compared to the *Type B* pattern, the average distance of successive readouts is increased by about one order of magnitude. Furthermore, the average distance is uncorrelated

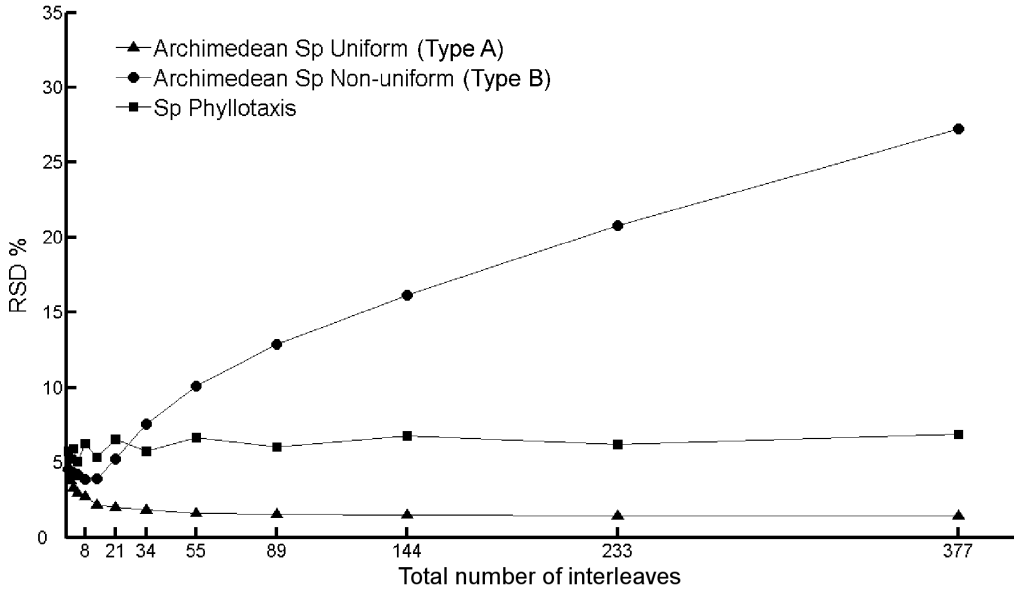

Figure 3.5: Plots of the relative standard deviation *RSD* of the distance between adjacent readouts on the sphere over the total number of interleaves. The distributions were simulated with a constant number of readouts per interleave ($P = 34$) for the three described methods. Increasing the total number of interleaves, the *RSD* of the *Type A* Archimedean spiral pattern decreases rapidly and remains very low, whereas the Archimedean spiral pattern implementing the non-uniform interleaving approach of *Type B* increases to significantly high values. The *RSD* of the spiral phyllotaxis pattern remains consistently low regardless of the number of interleaves. Even if the RSD of the spiral phyllotaxis is higher than the uniform Archimedean spiral, density compensation for uniform distribution is still applicable, as described in [Steh 05b].

with the number of interleaves. The mean distance of successive readouts of the spiral phyllotaxis pattern rapidly decreases with an increasing Fibonacci number of interleaves and is practically identical to the Archimedean spiral pattern of *Type B*.

The innermost parts of the two PSFs do not show any significant difference and, in general, each PSF individually features a very similar signal distribution in all planes containing the SI axis. However, as displayed in the central coronal and central sagittal slices of the two PSFs in Fig. 3.7, the spatial distribution of the signal intensities in the evaluated volume reveals prominent differences. In the PSF of the Archimedean spiral pattern, in (a) and (c), a spherical volume around the center of k-space with very little streaking components can be identified. Although the transversal diameter of the corresponding central volume is smaller in the PSF of the spiral phyllotaxis pattern (d), the volume with minimal streaking is extended to a cylinder oriented along the SI direction (b). The signal intensity of the central peak of the PSFs is identically 4014 for both trajectories, the one based on the Archimedean spiral pattern and the other on the spiral phyllotaxis pattern. In the framed region labelled with number (1), the mean signal intensity is lower for the Archimedean

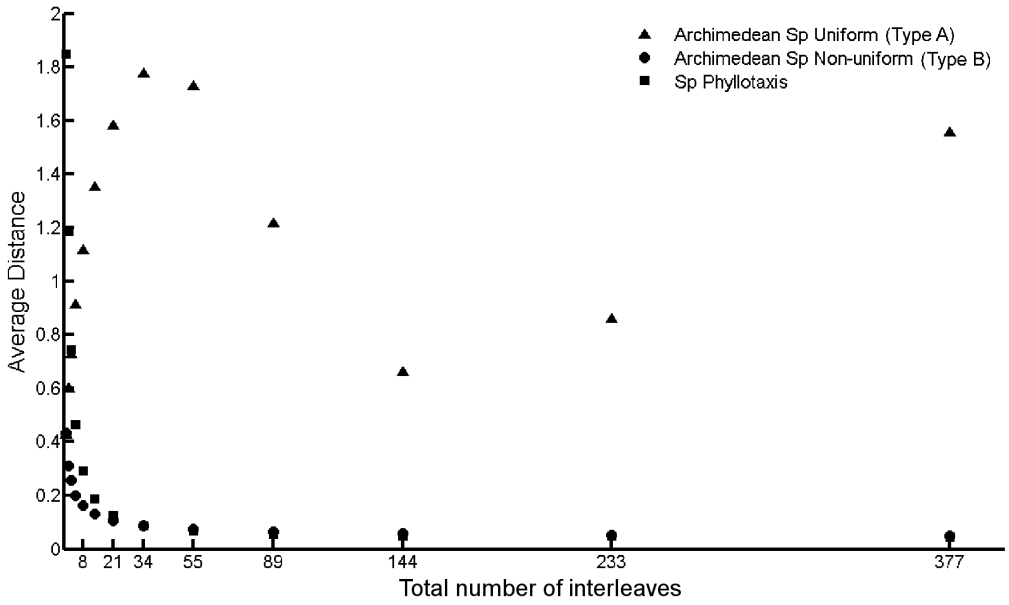

Figure 3.6: Plots of the average angular distance (in radians) between the origins of subsequent readouts within one interleave over the displayed total number of interleaves, computed only for Fibonacci numbers, for the three methods described. The mean distance is very high for the uniform Archimedean spiral pattern and shows no correlation with the number of interleaves. Both the spiral phyllotaxis and the non-uniform Archimedean spiral, on the other hand, show smooth gradient displacements and a similar decrease with the increase of the total number of interleaves, thus implying robustness to eddy current effects.

spiral pattern, 0.16 ± 0.11, compared to the spiral phyllotaxis pattern, 0.25 ± 0.18. Nevertheless, the signal intensity of the framed region (2) in the PSF of the novel trajectory, 0.48 ± 0.32, is about one-fifth of the Archimedean spiral, 2.77 ± 1.60.

3.4.2 MR Experiments and Image Quality

Compared with the reference data set in Fig. 3.8a, which was acquired with a non-interleaved Archimedean spiral pattern, phantom images were degraded by eddy current effects when data acquisition was performed with the interleaved Archimedean pattern of *Type A*: Fig. 3.8b. The image quality was almost completely restored in case of the interleaved spiral phyllotaxis pattern in Fig. 3.8c.

The in vivo experiments (Fig. 3.9) not only confirmed that eddy currents are strongly reduced with the interleaved spiral phyllotaxis pattern, but also residual streaking artifacts were significantly diminished. This trend was also reflected by SNR and CNR measurements (Tab. 3.1). Both SNR and CNR of images acquired with the interleaved Archimedean pattern decreased in comparison to the reference data. With the spiral phyllotaxis pattern, SNR and CNR were even superior to the reference. The

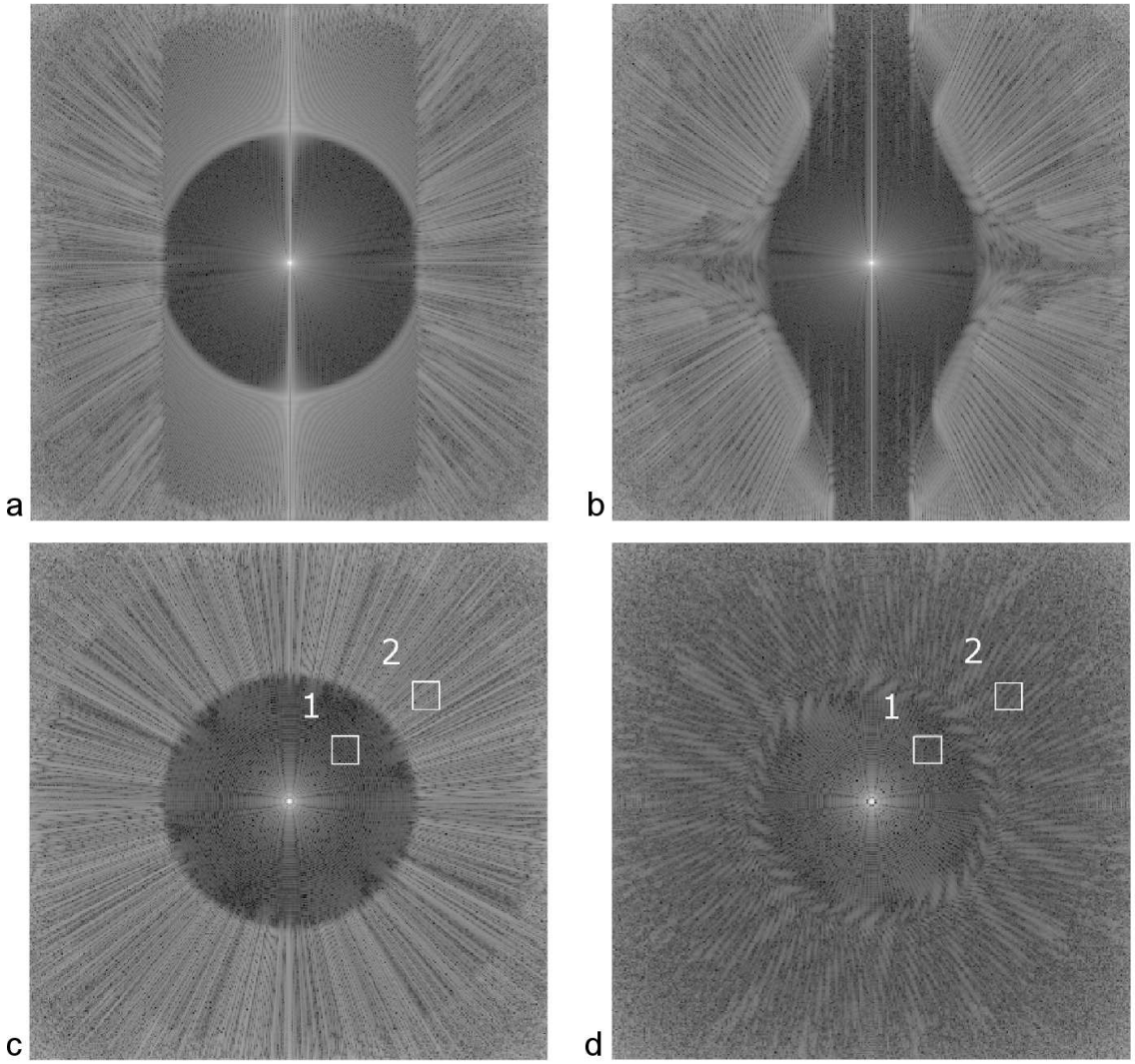

Figure 3.7: Comparison between the PSFs of the 3D radial trajectories based on the uniform Archimedean spiral pattern (a,c) and on the new spiral phyllotaxis pattern (b,d) over two FOVs. Both trajectories were acquired with an undersampling ratio of 22% and total number of readouts $N = 12818$. The plots represent the central coronal (a,b) and the central transversal (c,d) slices of a 3D volume with the signal intensities plotted on a logarithmic scale. While the amplitude of the central peak is the same for both PSFs, the overall signal distribution of the streaking patterns differs significantly.

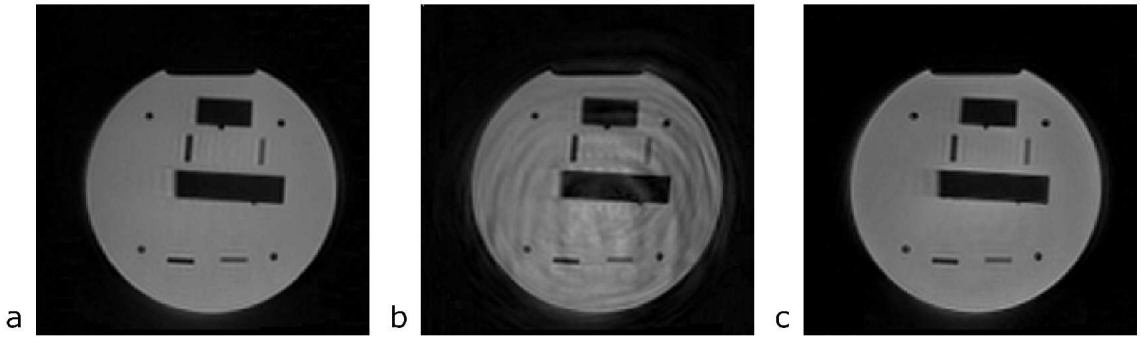

Figure 3.8: Phantom experiments with an SSFP sequence demonstrating the sensitivity of different types of 3D radial sampling patterns to eddy currents. Since the overall distribution of readouts was uniform for all the sampling patterns, the same image reconstruction program including the density compensation function was used in all cases. (a) Reference image acquired with a non-interleaved Archimedean spiral pattern (12818 readouts): only minor ringing artifacts are visible. (b) Image acquired with the Archimedean spiral pattern interleaved with the straightforward approach of *Type A* (12818 readouts in 377 interleaves and 34 readouts per interleave): the image quality is degraded by severe eddy current effects. (c) Novel interleaved 3D spiral phyllotaxis pattern (12818 readouts in 377 interleaves and 34 readouts per interleave): the image quality is almost completely restored.

vessel sharpness of 0.74 ± 0.13 in case of the spiral phyllotaxis pattern was slightly superior to both the interleaved and even the non-interleaved Archimedean spiral pattern with values of 0.64 ± 0.14 and 0.68 ± 0.12, respectively. Irrespectively of the overall image quality and of the trajectory used for acquisition, residual bright fat signal, around the proximal part of the coronary vessels could be detected in different locations in all the image data.

	Archimedean Non Interl.	Archimedean Interleaved	Spiral Phyllotaxis
SNR	5.71 ± 1.41	4.17 ± 1.05	6.42 ± 1.71
CNR	2.46 ± 0.94	1.81 ± 0.83	2.96 ± 1.16
Vessel sharp.	0.68 ± 0.12	0.64 ± 0.14	0.74 ± 0.13

Table 3.1: Numerical results of the comparison between the in vivo acquisitions with the three different trajectories. Not only the new spiral phyllotaxis pattern results in an improved image quality with respect to the Archimedean spiral pattern with interleaving approach of *Type A*, but also shows reduced artifacts with respect to the non-interleaved Archimedean spiral.

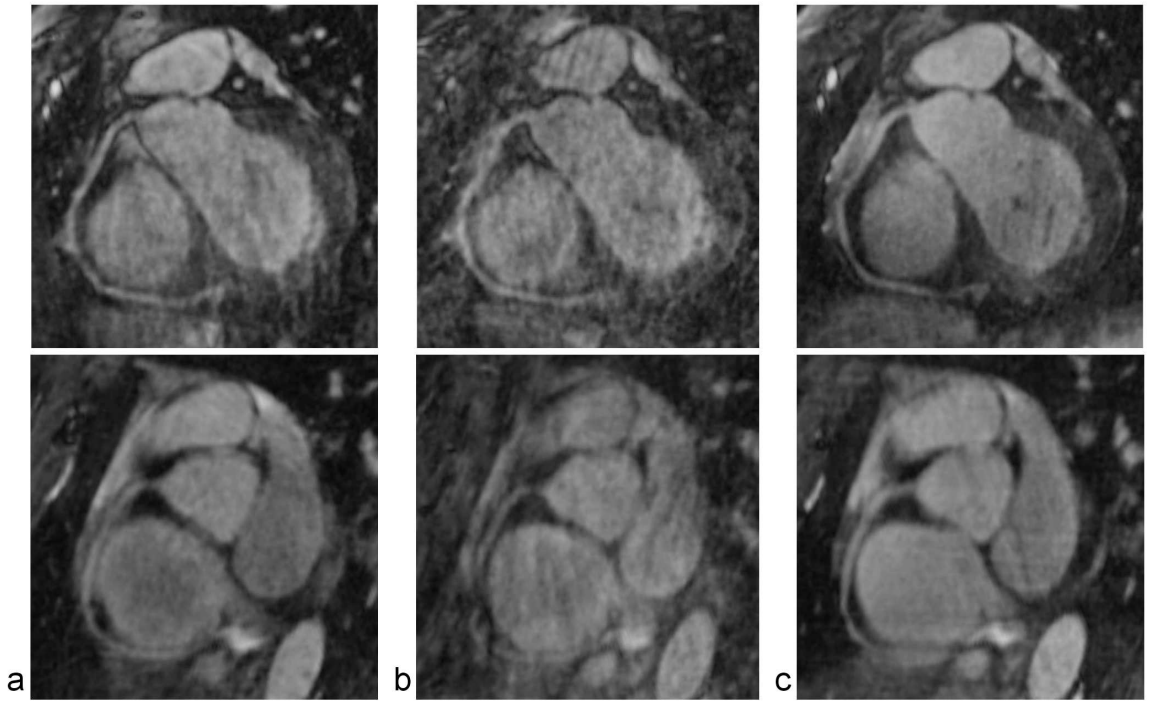

Figure 3.9: Reformatted images of two RCAs are depicted for acquisitions obtained with the three different 3D radial trajectories reconstructed with a gridding algorithm featuring identical density compensation settings. (a) Reference images, which were acquired with a non-interleaved 3D Archimedean spiral pattern, were compared to (b) images from Archimedean spiral pattern acquired with the straightforward interleaving approach of *Type A*. In the latter case, the image quality was degraded by eddy current effects. In images that were acquired with the novel interleaved 3D spiral phyllotaxis pattern (c), the overall image quality was even better than the reference. The new trajectory features superior interleaving properties while preserving an overall uniform sampling distribution.

3.5 Discussion

The current implementation of the 3D radial trajectory based on the spiral phyllotaxis pattern features an overall uniformity in the distribution of the readouts. In fact, although the RSD of the spiral phyllotaxis is higher than that of the uniform Archimedean spiral, a density compensation algorithm for uniform distribution is considered to be sufficient when the RSD is less than 10% [Steh 05b]. Furthermore, the new trajectory intrinsically provides an arrangement of the readouts that minimizes eddy current effects, if interleaved with a Fibonacci number. Nevertheless, an effective sorting of the readouts is also feasible when a non-Fibonacci number of interleaves is selected. Alternative mathematical models for constructing the spiral phyllotaxis can be implemented to further increase the overall uniformity of the trajectory. These can include the introduction of a variable offset to the azimuthal shift in Vogel's formula [Rldl 82] or the addition of other constraints, e.g. the target distance between adjacent readouts [Fowl 92]. In these cases, the consistency of the intrinsic arrangement of the readouts needs to be verified and a trade-off between

feasible improvements and computational effort has to be considered.

Phantom experiments showed that the final image quality obtained with the interleaved spiral phyllotaxis pattern is close to the uniform Archimedean non interleaved spiral pattern. Although eddy current effects were avoided, a slight residual degradation of the image quality might be explained by a disadvantage of the novel trajectory when the FOV is larger than the imaged object. The reason for the reduction of streaking in vivo can be found in the substantial difference in the PSFs of the trajectories used. Since RF excitation was non-selective and the size of the object largely exceeded the FOV in SI direction, the novel trajectory can be expected to be more robust against aliasing artifacts in this direction. The difference in the transversal orientation of the PSFs might also have a positive effect, if aliasing energy of anterior-posterior or left-right structures, such as the chest wall or the arms, is taken into account. This, in fact, might also positively affect the overall image quality reflected in the results of SNR and CNR. Nevertheless, considering the number of cases analysed, neither the superior SNR and CNR, nor the improvement in vessel sharpness can be rated as statistically significant. In the latter case, the improvement is more likely to be caused by the general improvement of the image quality, rather than a difference in the PSFs, since the innermost part of the two PSFs is practically identical.

The image quality of all in vivo data sets was affected by the prolonged acquisition times, usually caused by irregularities in the breathing pattern of the volunteers and/or by a sub-optimal placement of the beam navigator. For this reason, coronary MRI implementing respiratory self-navigation methods is highly desired. An extra readout constantly oriented along the SI direction can be added at the beginning of each interleave of the spiral phyllotaxis pattern and used for the detection of the respiratory motion [Steh 05b]. If the extra readout is not taken into account in the reconstruction, then all the properties of the trajectory remain unchanged. Therefore, the 3D spiral phyllotaxis pattern is intrinsically prepared for self-navigation.

The spiral phyllotaxis pattern also holds further mathematical properties that can be exploited for clinical applications. In the highly interleaved setup required for coronary MRI, this trajectory automatically arranges in such a way that each new interleave is placed in the largest azimuthal gap left by the preceding set of interleaves and always divides the gap according to the golden ratio, thus providing an almost uniform sampling pattern over time [Wink 07]. As a consequence, subsets of successive interleaves at arbitrary time points can be used to reconstruct sub-sampled imaging volumes with high spatial uniformity. In this context of temporal stability, an experimental comparison between the new 3D spiral phyllotaxis pattern and the adaptive radial 3D projection reconstruction method, recently proposed in [Chan 09] and based on multi-dimensional golden means, is considered very interesting. Moreover, Fig. 3.4(a.2) and 3.4(c.2) suggest that the distribution of the readouts in a single interleave in a highly interleaved setup is more uniform for the spiral phyllotaxis than for the uniform Archimedean spiral, when a non-Fibonacci number of interleaves is selected. The overall sampling uniformity of the spiral phyllotaxis makes it attractive

for applications dealing with highly undersampled data. In this context, the impact of parallel imaging techniques for non-Cartesian trajectories, such as [Seib 07] can be explored. Furthermore, the combination of methods exploiting the redundancy of the information contained in the images, such as HYPR [Mist 06] or iterative reconstruction methods like compressed sensing [Lust 07], with the 3D spiral phyllotaxis pattern represents an attractive possibility [Done 08]. Such combinations, in fact, could lead not only to highly reduced total examination times for applications such as coronary MRI, but also to feasible applications in dynamic studies, e.g. cine or perfusion MRI. Eventually, concerning the sub-optimal effectiveness of the fat saturation pulses, better results could be achieved by improving the shimming procedure within the imaged volume [Desh 03]. On the other hand, since the fat saturation pulse is applied only once at the beginning of each interleave, further advantages could derive from the acquisition of a smaller number of readouts per interleave.

3.6 Conclusion

The new 3D radial trajectory based on the spiral phyllotaxis pattern is a "natural" solution for radial 3D MRI. This trajectory features a simple mathematical implementation and can be easily integrated into existing 3D radial acquisition frameworks without the need for a dedicated density compensation algorithm. The spiral phyllotaxis pattern combines both an overall uniformity of the distribution of the readouts and an intrinsic arrangement that reduces eddy current effects, thus overcoming the limitations of the reference approaches. This work, and in particular the good results obtained in the in vivo experiments, demonstrated that the radial 3D trajectory based on the spiral phyllotaxis pattern is a robust solution for volumetric acquisitions where both radial undersampling and motion are involved and where a high interleaving setup is required. The application of the new trajectory for self-navigation and the integration of motion correction algorithms will be discussed in the next chapters.

Chapter 4

Robust 1D Respiratory Self-Navigation

In this chapter, a new approach for self-navigated whole heart coronary MRI, based on a novel technique to isolate the blood pool, is described. The isolation is obtained using a specific combination of the output signals from a phased-array surface receiver coil, placed on the chest. Furthermore, an algorithm for the automatic segmentation of the blood pool is proposed. Signal suppression, automatic segmentation, motion detection and compensation are fully integrated in the data acquisition and reconstruction framework to allow a fast and easy workflow for coronary MR imaging. The results of the self-navigation are compared with the navigator-gated technique in 10 healthy volunteers. Major parts of this chapter are published in [Picc 12].

4.1 Motivations

4.1.1 State of the Art Navigator-Gating

As described at the end of Chapter 2, the state of the art approach to minimize the effects of respiratory motion during coronary MRI examination consists in the use of a beam-navigator [Ehma 89]. Such navigator is usually placed on the dome of the right hemidiaphragm and provides feedback on the respiratory position of the diaphragm [McLe 02] along the major direction of respiratory motion, namely the superior-inferior direction. A gating window is defined in end-expiration, such that only the interleaves acquired within the window are used for the final reconstruction. All the other interleaves are discarded and re-acquired. A more detailed description

is provided in Section 2.4.3. There are three major intrinsic limitations in the standard navigator-gated technique. 1) Respiratory gating performs with an efficiency of less than 40%, in many cases. 2) An ill-positioned navigator, as well as irregularities on the respiratory pattern of the patient, might lead to unpredictably extended examination times. In cases where the variation in respiratory motion is very large, adaptive windowing techniques [Desh 06, Jhoo 10] are not reliable and the acquisition might not be completed. 3) The accuracy of the motion detection performed with the navigator is sub-optimal, as it does not take the inter-patient variability into account, and is adversely affected by hysteretic effects and temporal delays.

4.1.2 Self-Navigation with Radial 3D Trajectories

As described in Section 2.4.4, respiratory self-navigation has recently been introduced to overcome these drawbacks. With this method it is possible to assess the information on the respiratory motion directly from the 1D FFT of readouts acquired at the beginning of each interleave and which can be interpreted as projections of the imaging volume onto the SI axis (Fig. 4.1a, b). The SI projection of each interleave is compared with a reference projection acquired at the beginning of the examination to determine the respiratory offset. This enables to perform motion correction directly in k-space during image reconstruction with: 1) an acceptance rate of 100%, 2) simplified examination planning and a priori knowledge of the duration of the acquisition regardless of the individual respiratory patterns, and 3) improved accuracy of the motion compensation.

Radial 3D trajectories are particularly well suited for this application, as they combine straightforward adaptation to self-navigation [Steh 05b, Picc 11] with intrinsic robustness against motion [Steh 04] and low sensitivity to undersampling [Lauz 96, Barg 02]. However, 3D radial acquisitions are usually performed using non-selective RF pulses such that the signal contributing to the radial readouts is collected over the entire volume. In this scenario, fat saturation [Rose 84] and T2 preparation [Wrig 91, Brit 95] are sometimes insufficient to ensure the necessary contrast in the SI projections to isolate the signal of the blood pool (Fig. 4.1c-e). It has been shown that the presence of additional sources of bright signal, e.g. the spine, the chest wall, the arms and the liver, can heavily perturb the results of a detection performed with center of mass [Lai 08]. The use of more robust techniques, such as cross-correlation, is required to perform a reliable self-navigation. Therefore, all sources of additional bright signal must be suppressed such that the contribution of the blood pool in the SI projections can be reliably isolated.

4.1.3 Research Contributions

In this chapter, the development, implementation and testing of a new technique for improved performance of self-navigated whole heart coronary MRI is described in detail. The 3D radial sequence featuring the spiral phyllotaxis pattern introduced in the previous chapter was adapted to self-navigation [Picc 12]. A novel technique to

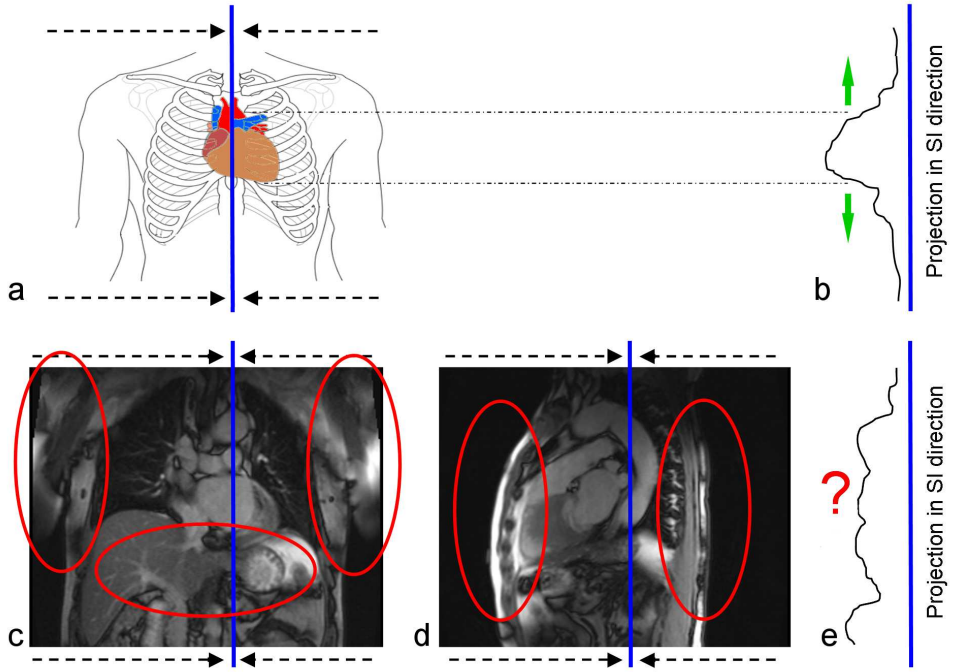

Figure 4.1: Graphical representation of the shape of a typical SI projection in the ideal and in the real case scenario. The SI projections can be interpreted as projections of the whole imaging volume onto the SI axis (black dotted arrows). In an ideal scenario (a) the blood-pool is the only source of bright signal within the chest. Thus, the position and displacement (green arrows) of the heart along the SI projection can be easily identified (b). However, in a real setup, here represented by a 2D sagittal (c) and a 2D coronal (d) slice, several other sources of bright signal (red ellipses) can corrupt the SI profile (e). In this case the identification of the blood pool is impossible.

suppress the additional bright signal from the arms and the chest wall is illustrated, which allows to reliably isolate the blood pool. This technique is based on the combination of the output signals from a phased-array surface receiver coil, placed on the chest. Furthermore, an algorithm for the automatic segmentation of the blood pool within the reference SI projections is proposed. Signal suppression, automatic segmentation, motion detection and compensation were all fully integrated in the data acquisition and reconstruction framework to allow a fast and easy workflow for coronary MR imaging. The results of the self-navigation are compared with the navigator-gated technique in 10 healthy volunteers.

4.2 Materials and Methods

4.2.1 Isolation of the Blood Pool

In general, reliable isolation of the bright signal of the blood pool is essential to achieve robust self-navigation. In the case of non-selective 3D radial acquisitions,

the input data used for self-navigation is degraded by several additional sources of bright signal: the anterior chest wall, the spine, the lateral chest wall, the arms and the liver (Fig. 4.1c, d). It has been demonstrated that the signal from the anterior chest wall can be efficiently suppressed by a saturation slab [Stub 99b]. Furthermore, the signal originating from the spine can be significantly reduced by just excluding the signal from the posterior phased-array coil in post-processing. In contrast, the suppression of the signal originating from the lateral structures, i.e. the arms and the lateral chest wall, is a more challenging task.

Similarly to the methodology used for the spine, the exclusion of the lateral coil elements of the anterior phased-array coil was initially attempted to exclude the signal contribution of the lateral structures. However, a significant amount of lateral signal was still caught by the central coil elements. Therefore, a new targeted signal combination was considered, to exploit advantageously the hardware structure of the anterior phased-array coil. In general, a *Mode Matrix* technology (Siemens AG, Healthcare Sector, Erlangen, Germany) is implemented in the hardware of some of the phased-array coils of the Siemens system [Reyk 04] (Fig. 4.2). In particular, in

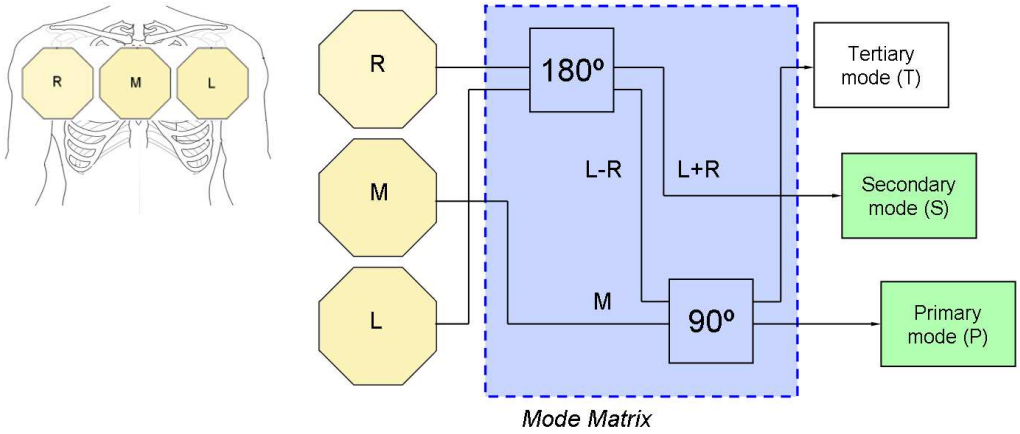

Figure 4.2: Simple scheme of the *Mode Matrix* technology. The three physical coil elements R, M and L are hardware combined to form the three mode signals P, S and T. The mathematical formulation corresponding to this scheme is reported in Eq. 4.1.

the anterior phased-array coil, the signals from the right (R), middle (M) and left (L) coil elements are amplified and combined to form a set of three mode signals, referred to as primary mode (P), secondary mode (S) and tertiary mode (T). The corresponding mathematical formulation is given in Eq. 4.1.

$$\begin{bmatrix} P \\ S \\ T \end{bmatrix} = \begin{bmatrix} \frac{1}{2} & -\frac{j}{\sqrt{2}} & -\frac{1}{2} \\ \frac{1}{\sqrt{2}} & 0 & \frac{1}{\sqrt{2}} \\ \frac{1}{2} & \frac{j}{\sqrt{2}} & -\frac{1}{2} \end{bmatrix} \cdot \begin{bmatrix} R \\ M \\ L \end{bmatrix} \tag{4.1}$$

The P mode can be regarded as a one-channel circularly polarized (CP) coil, which is used for standard imaging. An example is shown, in magnitude $|\mathcal{FFT}\{P\}|$, in Fig. 4.3a.1. Because of the contribution of the additional lateral signal, the bright signal of the blood pool is not clearly isolated from the background in the SI projections, Fig. 4.3a.2. As it can be deduced from the signal $|\mathcal{FFT}\{S\}|$, displayed in Fig. 4.3b, the largest component that forms the S mode originates from the lateral coil elements, while the central portion is almost completely excluded. A combination C of the two modes, obtained by subtraction of $|\mathcal{FFT}\{S\}|$ from $|\mathcal{FFT}\{P\}|$, efficiently suppresses the signal from the lateral structures, Fig. 4.3c.1. Although the implementation

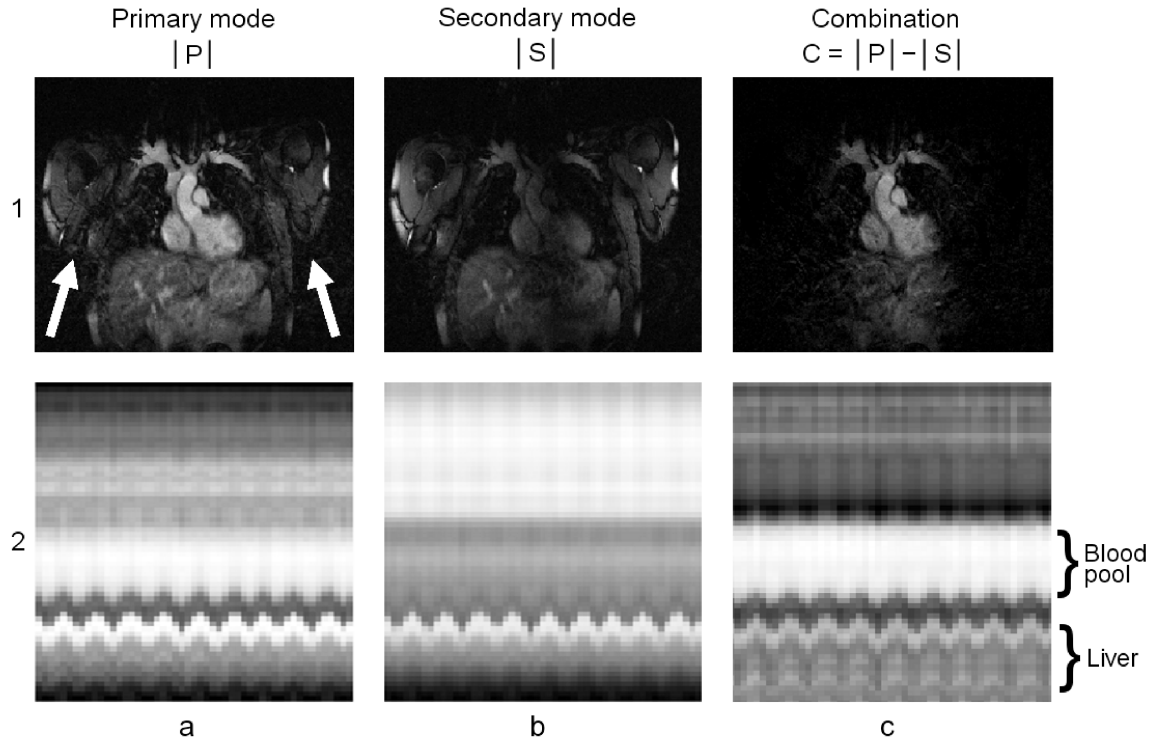

Figure 4.3: Example of the suppression of the bright signal of the lateral structures by combination of the mode signals from the anterior phased-array coil. While row (1) shows three 2D coronal slices, obtained with standard Cartesian acquisitions from one of the volunteers, row (2) displays three series of SI projections acquired with the 3D radial trajectory, in the same volunteer, in 50 consecutive heartbeats. Column (a) displays the magnitude of the signal reconstructed with the primary mode: in this case the blood pool is not clearly isolated from the background in the series of SI projections (a.2), due to the contribution of bright signal from the lateral structures (a.1, white arrows). Since the magnitude of the signal reconstructed with the secondary mode, displayed in (b), originates predominantly from the lateral coil elements, an advantageous combination of the two mode signals is implemented. If $|\mathcal{FFT}\{S\}|$ is subtracted from $|\mathcal{FFT}\{P\}|$, then the bright signal of the lateral structures is efficiently suppressed (c.1) and a reliable isolation of the bright signal of the blood pool in the SI projections is possible (c.2).

of the channel combination utilizes the *Mode Matrix* hardware, this method can be generalized for other configurations of phased array surface coils with right, left and middle coil elements. The mathematical formulation of the signal suppression applied to the SI readouts is directly derived from Eq. 4.1:

$$C_{SI} \;=\; |\,\mathcal{FFT}\{P_{SI}\}\,| - |\,\mathcal{FFT}\{S_{SI}\}\,| \;=$$

$$= \;\left|\,\mathcal{FFT}\left\{\frac{(R_{SI}-L_{SI})}{2} \;-\; j\,\frac{M_{SI}}{\sqrt{2}}\right\}\,\right| \;-\; \left|\,\mathcal{FFT}\left\{\frac{(R_{SI}+L_{SI})}{\sqrt{2}}\right\}\,\right|, \tag{4.2}$$

where P_{SI} and S_{SI} represent the complex readouts with SI orientations obtained respectively from the primary and secondary modes, and R_{SI}, L_{SI} and M_{SI} are the complex SI readouts from the right, left and middle coil elements. The symbol j represents the imaginary unit, and the $|\cdot|$ operator computes the absolute value of the signal pixelwise. $\mathcal{FFT}\{X_{SI}\}$ represents the SI projection of the SI readout X_{SI}, while C_{SI} is the SI projection resulting from the channel combination. After the channel combination is performed, the additional bright signal is suppressed in the SI projections and the blood pool is reliably isolated, Fig. 4.3c.2.

4.2.2 Segmentation of the Blood Pool

A reliable identification of the structure corresponding to the blood pool is essential to compute its motion using cross-correlation. While the channel combination provides the suppression of the additional bright lateral signal, this method does not ensure the blood pool to be the only, or at least the brightest, isolated structure within the SI projections. Hence, an algorithm was developed which automatically segments the blood pool in four steps. This algorithm was applied, after intensity normalization (Eq. 4.3), to the reference SI projection F_N that is obtained from the very first acquired readout. In the equation, F represents the reference SI projection before normalization.

$$F_N(i) = \frac{F(i) - \min\{F\}}{\max\{F\} - \min\{F\}}. \tag{4.3}$$

The algorithm assumes that the FOV is placed such that the blood pool be in the center of the SI projections.
The four steps are as follows: 1) The index of a local maximum within the blood pool, M, is found in an initial search range around the central point of the SI projection, equal to one-eighth of the total length of the projection. A second point m, representing the index of the local minimum candidate, is iteratively moved outwards, Fig. 4.4a. 2) At each iteration, two areas A_1 and A_2 are computed and compared. A_1, highlighted by diagonal stripes in Fig. 4.4b, is the area of the trapezoid delimited by the vertices $F_N(M)$ and $F_N(m)$ on the projection and by the indexes M and m on

the abscissa. A_2 is the area under the curve (AUC) of the projection, spanned from index M to m. The stopping criterion is reached when the former exceeds the latter:

$$A_1 = \frac{(\ F_N(M) + F_N(m)\ ) \cdot\ \mid m - M \mid}{2} > \sum_{i=M}^{m} F_N(i)\ = A_2 \tag{4.4}$$

3) The final position of m is then assigned to the index corresponding to the local minimum within the current $[M, m]$ interval, Fig. 4.4c. 4) Finally, the indices i_1 and i_2, corresponding to $F_N(i_k)\ \simeq\ 0.5 \cdot (\ F_N(M) - F_N(m)\ )$, where $k = 1, 2$ and the symbol $\simeq$ refers to the closest pixel, represent the final result of the segmentation, Fig. 4.4d.

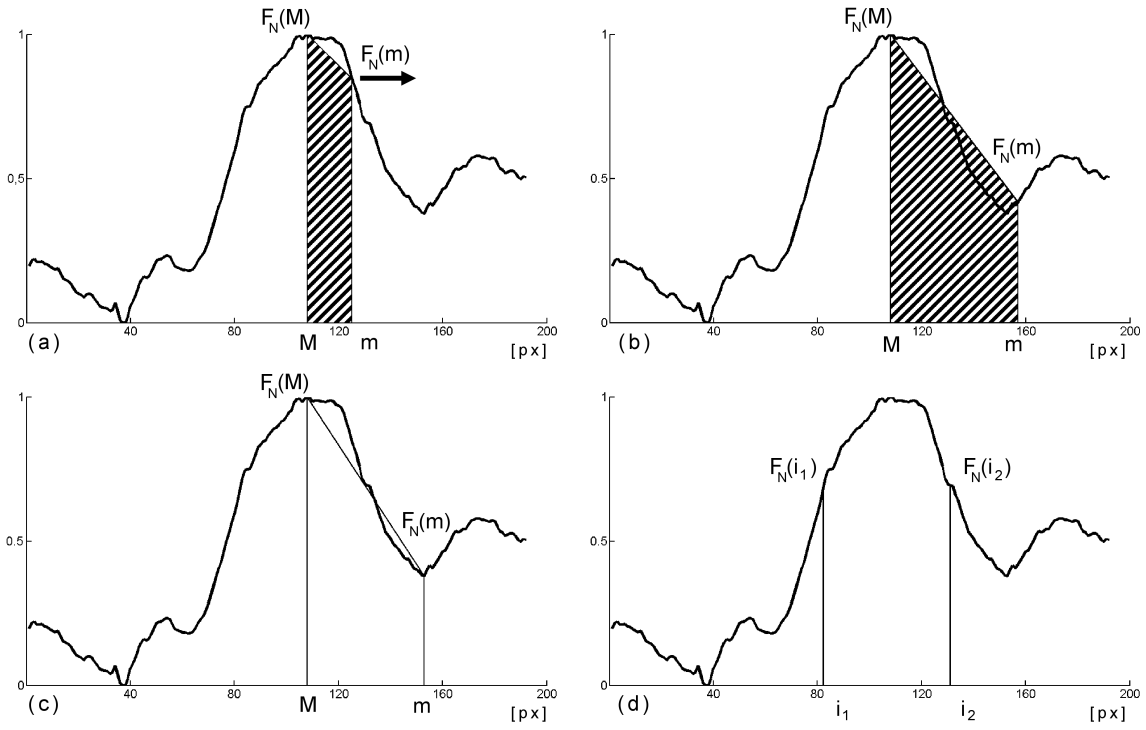

Figure 4.4: Graphical representation of the four steps algorithm for the automatic segmentation of the blood pool in the normalized reference SI projection, F_N. 1) The index of a local maximum M is detected within a neighbourhood of the central point of the projection and a second index m is iteratively moved outwards (a). 2) A criterion based on the area under the curve between M and m is used to stop the iterations (b). 3) The index corresponding to the local minimum between these two points is chosen as the final m (c). 4) Finally, two indices i_1 and i_2, corresponding to the amplitude of 50% of the difference between $F_N(M)$ and $F_N(m)$ are selected as final result of the segmentation (d).

4.2.3 Motion Detection and Compensation

The segmented section $[i_1, i_2]$ of the blood pool in the reference SI projection F_N is then cross-correlated with each of the successive normalized SI projections G_N. A modified version of the cross correlation algorithm was adopted:

$$\underset{\Delta i}{\operatorname{argmax}} \frac{\sum_{j=i_1}^{i_2}(F_N(j) - \bar{F_N}) \cdot (G_N(j + \Delta i) - \bar{F_N})}{\sqrt{\sum_{j=i_1}^{i_2}(F_N(j) - \bar{F_N})} \cdot \sqrt{\sum_{j=i_1}^{i_2}(G_N(j + \Delta i) - \bar{F_N})}}; \tag{4.5}$$

with $\bar{F_N}$ defined as:

$$\bar{F_N} = \frac{\sum_{j=i_1}^{i_2} F_N(j)}{i_2 - i_1}; \tag{4.6}$$

This allows to compute the respiratory shift in SI direction, in pixels, corresponding to each interleave. Motion correction is performed in k-space, prior to the interpolation of the radial readouts onto the Cartesian grid, by shifting the linear phase of each readout by an angular increment $\Delta\beta$, according to the *Fourier shift theorem*. As previously described at the end of Section 2.3.2, the linear phase increment for each readout, where N is the total number of readouts, is computed according to the detected shift Δi and to the polar angle θ between the current readout and the SI orientation. The mathematical formulation can be directly derived form Eq. 2.18:

$$\Delta\beta = \frac{2\pi}{N} \cdot \Delta i \cdot \cos(\theta) \tag{4.7}$$

4.2.4 MR Experiments

The presented signal suppression method and the segmentation algorithm were fully integrated in the Siemens data acquisition and image reconstruction framework, with software release syngo MR B17A. The new method for self-navigation was compared with a navigator-gated approach featuring the same acquisition protocol. In vivo experiments were performed on 10 healthy volunteers - 6 males and 4 females, age: 35 ± 12.5 years - after written consent was obtained. The imaging platform was a 1.5 T MAGNETOM Avanto scanner (Siemens AG, Healthcare Sector, Erlangen, Germany). A total of 12 elements of the anterior and posterior phased-array coils were activated for signal reception. Data acquisition was performed with a 3D radial trajectory implementing the spiral phyllotaxis pattern [Picc 11], adapted to self-navigation [Picc 12]. All measurements were interleaved and ECG-triggered. A 2D cine-scan

with transversal slice orientation, prior to the whole heart measurement, was used to precisely determine the individual delay of the acquisition window, needed to target the cardiac rest period in mid-diastole (Section 1.2.1). The cubic FOV was positioned such that the first readout of every interleave was oriented along the SI direction (Fig. 4.5). T2-prepared, fat-saturated, balanced SSFP imaging was performed for both navigator-gated and self-navigated acquisitions with the following parameters: TR/TE 3.0/1.52 ms, FOV $(220\ \text{mm})^3$, matrix 192^3, acquired voxel size $(1.15\ \text{mm})^3$, flip angle 90° and receiver bandwidth 898 Hz/Px. A total of 11687 radial readouts were acquired in 377 heartbeats. This resulted in an overall undersampling ratio of 20%, with respect to the Nyquist limit in the 3D radial case. Two-fold oversampling was applied in the readout direction to automatically avoid foldover artifacts [Lauz 98]. For gated acquisitions, a crossed-slice spin echo navigator was accurately positioned on the dome of the right hemidiaphragm. The width of the gating window of the navigator was 5 mm and slice tracking with a fixed correlation factor of 0.6 [Wang 95] was used. For self-navigated acquisitions, motion correction was applied to 100% of the acquired interleaves. A dummy interleave, without data acquisition, was applied before the beginning of the actual measurement to avoid artifacts from signal oscillations on the reference projection.

As a quality control during self-navigated acquisitions, all SI-projections were visualized with the Inline Display (Siemens AG, Healthcare Sector, Erlangen, Germany). The quality control enabled the operator to assess the successful isolation of the blood pool for all projections, as well as the correctness of the segmentation and the plausibility of the feedback of the cross correlation (Fig. 4.6). This procedure allowed an early reaction at the beginning of the acquisitions, if the FOV was incorrectly positioned by the operator, such that a wrong structure was initially segmented. Furthermore, the feedback of the beam-navigator was acquired as well during self-navigated acquisitions and used for data analysis.

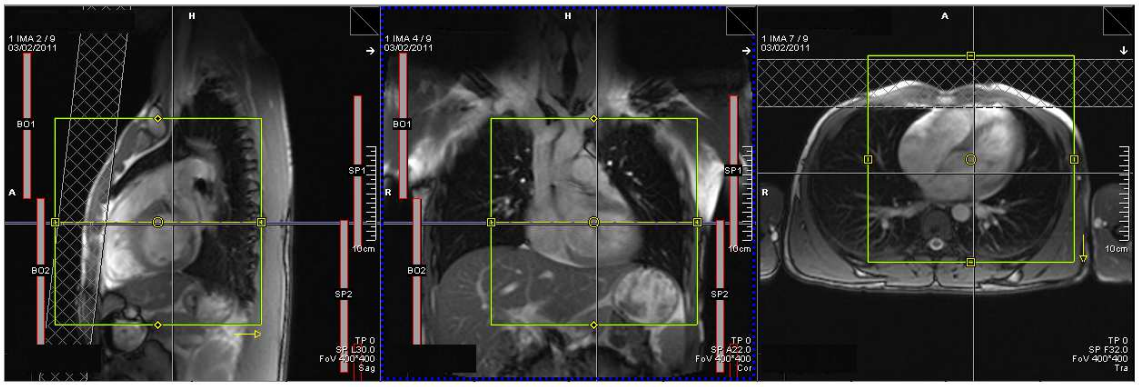

Figure 4.5: Example of the acquisition planning with the new self-navigated approach. The cubic FOV is positioned such that the blood pool is in the center in each of the views (yellow/green squares). The placement of a saturation slab (gray rectangle) allows to suppress the bright signal of the anterior chest wall. This image is courtesy of Siemens AG, Healthcare Sector, Erlangen, Germany.

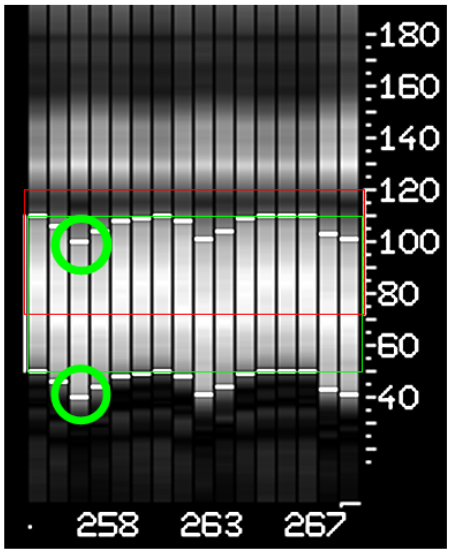

Figure 4.6: Example of the inline display used for the quality control during the measurements. The display shows the SI projections as soon as they are acquired. The bright signal from the blood pool is clearly isolated from the background in the center of the projections. The result of the segmentation and cross-correlation is visible as pairs of bright horizontal marks within each projection. One of these pairs is highlighted in the picture by two green circles. The use of such feedback method allows an early reaction in case of misplacement of the FOV or wrong segmentation. This image is courtesy of Siemens AG, Healthcare Sector, Erlangen, Germany.

4.2.5 Data Analysis

Due to the absence of a ground truth on the actual respiratory motion of the heart, the analysis of the data was performed in two steps. First a technical validation of the new method was accomplished and then the datasets acquired with the new method were compared with the navigator-gated acquisitions for acquisition time and image quality. As for the technical validation, the feedback provided by the cross correlation on the SI projections was compared with the feedback on the position of the diaphragm, provided by the beam-navigator, in all self-navigated acquisitions. To test the improvements obtained with the new technique, self-navigated motion detection was performed, for all volunteers, in three different configurations. The SI projections were cross correlated using: (1) the P mode and the complete reference SI projection (2) the signal combination and the complete reference SI projection, (3) the proposed approach. For each configuration and for each volunteer, the feedback from the self-navigation and that from the navigator were plotted, for all interleaves, in a common graph to visually assess their synchronicity. A strong synchronicity was interpreted as the proof of principle that a motion correlated to the respiratory cycle was detected by the self-navigation [Wang 95]. A quantification of the linear dependence between the two feedbacks was obtained by computing the Pearson product-moment correlation coefficient (PMCC) [Lee 88] in Matlab 7.3 (The MathWorks Inc, Natick, MA, USA). In addition, in case of strong visual synchronicity and high PMCC, the slope of the linear regression between the feedback of the self-navigation and of the

cross correlation was computed. The value of the slope was considered as an estimation of the subject-specific correlation factor, extended to the full respiratory cycle.

4.2.6 Acquisition Time and Image Quality

The total acquisition time of the self-navigated method was compared with the total acquisition time of the navigator-gated technique to estimate the average improvement in scan efficiency. The 3D isotropic image data, acquired with both methods, were reformatted in post-processing with CoronaViz 2.0 (Work in Progress software, Siemens Corporate Research, Princeton, NJ, USA) to visualize the right coronary artery (RCA), the left anterior descending artery (LAD) and the left coronary circumflex (LCX). The results of the off-line reformats were used for qualitative assessment of the image quality and to compare the number of detectable coronary arteries with the two acquisition schemes. A coronary artery that could be manually segmented for a length of at least 40 mm was defined as detectable. Vessel length was assessed for all the RCAs, LADs and LCXs that could be detected in both groups of datasets. Finally, the inverse of the average distance between the 20% and the 80% of the signal intensity profiles on both sides of a cross-sectional line, perpendicular to the axes of the coronary vessel, was used for the calculation of the vessel sharpness as described in [Li 01]. The final value of the vessel sharpness for each single coronary was averaged on eight manually selected cross-sections, distributed along the whole length of the segmented vessel. Statistical comparisons on all the results obtained on the navigator-gated and the self-navigated acquisitions were performed by means of a paired two-tailed Student t test. Values of $p \leq 0.05$ were considered as statistically significant.

4.3 Results

4.3.1 Data Analysis

Navigator-gated as well as self-navigated whole-heart coronary MRI acquisitions were successful in all volunteers. The visual assessment of the motion detection when the cross correlation was applied to the complete SI projection in P mode showed that almost no motion could be detected in 3 volunteers. In this case, the synchronicity with the feedback from the beam navigator was low in all volunteers and the total average value of the PMCC was only 0.67 ± 0.54. After the proposed signal combination, the blood pool was visualized as an isolated structure in all SI projections. Even when cross correlation was applied still to the complete projection, the visualized synchronicity showed a clear improvement. The average PMCC increased to 0.81 ± 0.08. Nevertheless, the value of the slope of the linear regression was lower than 0.2 for 5 volunteers with its total average being only 0.32 ± 0.24. The proposed algorithm for automatic segmentation, performed after signal combination, was always successful, despite the high variability of the shape of the SI profiles among different subjects. An example of the feedback from the motion detection obtained

with the new method is displayed, with two red lines, in Fig. 4.7a over a series of SI projections acquired in 50 consecutive heartbeats. In addition, an example of the high synchronicity with the feedback from the beam-navigator can be assessed in Fig. 4.7b, where the motion of the diaphragm is depicted by a green line. In this case, the average value of the PMCC was the highest, 0.85 ± 0.12, and confirmed the consistency of the motion estimation. With the new method, the average value of the slope of the linear regression between the result of the cross-correlation and the detection of the beam navigator, over all in vivo datasets, was 0.47 ± 0.30. This is graphically supported by Fig. 4.7b, where the curve of the self-navigation appears dampened if compared with the navigator. Fig. 4.7c shows the displacement detected with the new self-navigation plotted against the SI shift of the right hemidiaphragm, detected with the navigator. The range of 1D corrections varied, in average, between a minimum displacement of the blood pool of ± 1.15 mm, i.e. one pixel, and a maximum of ± 12.6 mm.

4.3.2 Acquisition Time and Image Quality

As reported in Tab. 4.1, with the full efficiency of the self-navigated method, the total acquisition time was reduced by more than 60%, compared to the navigator-gated reference. All RCAs could be segmented in both cases, whereas the segmentation of the LAD was possible in 9 of the 10 datasets acquired with navigator-gating and in all 10 self-navigated acquisitions. The LCX could be segmented only in 8 datasets, the same for both acquisitions. The quantitative assessment of vessel length and sharpness, displayed in Tab. 4.1, shows a slight average superiority of the new method. Although the mean improvement in the detected vessel length and sharpness was 8.3% and 5.8%, respectively, only the improvement in the vessel sharpness of the RCA showed a statistical significance ($p < 0.05$). In comparison with the reference (Fig. 4.8a, c, e), the image quality obtained with the self-navigation technique (Fig. 4.8b, d, f) was equivalent or slightly superior in almost all cases. In only one case, while the distal part of the LAD was well visualized in the navigator-gated dataset (Fig. 4.9a), the corresponding part appeared blurred by the effect of the residual motion artifacts in the self-navigated dataset (Fig. 4.9b). In general, the presence of minor artifacts, due to uncompensated residual motion, could be noticed in all datasets.

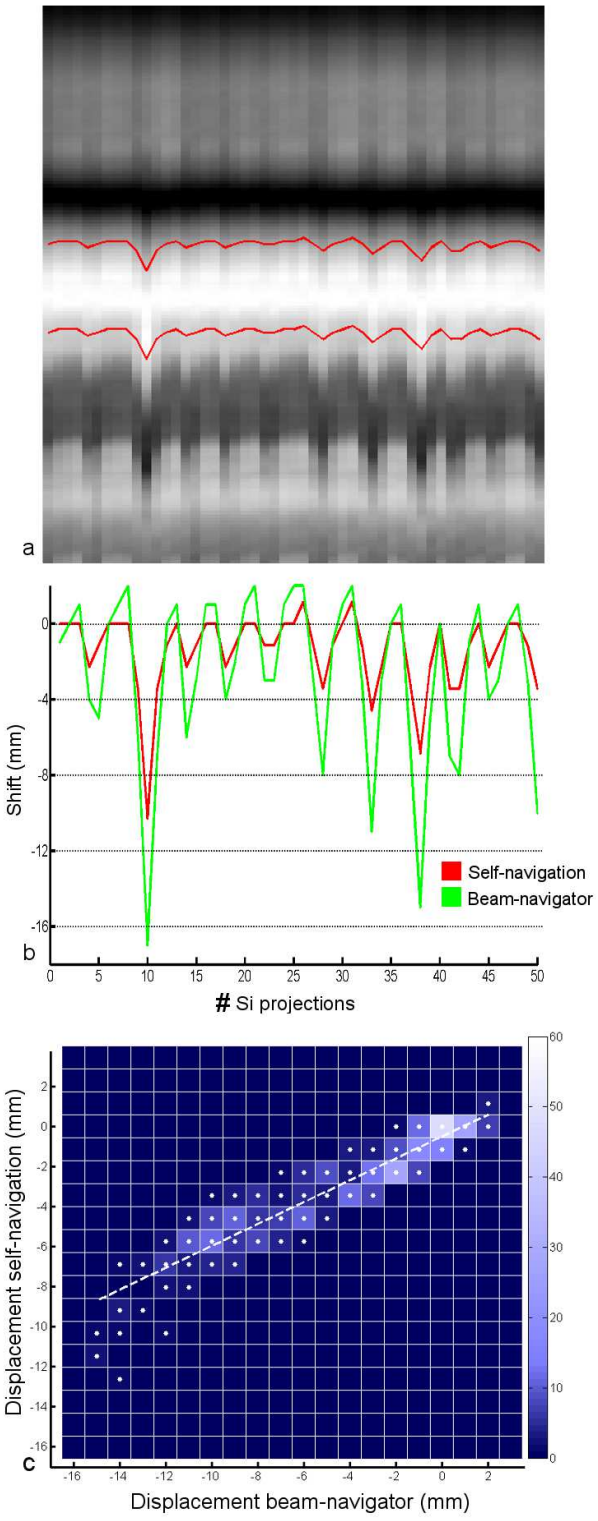

Figure 4.7: The respiratory motion detected by cross-correlation on the bright signal of the blood pool was compared for validation with the position of the diaphragm, detected by the beam-navigator. Due to the intrinsic limitations of the navigator-gated methods, the comparison with the position of the diaphragm is considered as a proof of principle for the proposed motion detection and not as a ground truth on the real respiratory motion of the heart. A series of 50 SI projections, acquired in 50 consecutive heartbeats, in one of the volunteers, is displayed in (a). The bright region in the central part of the projections is the isolated signal originating from the blood pool. The two red lines visualize the respiratory displacement, detected with the cross-correlation algorithm, of the two indices (i_1 and i_2) selected by the segmentation algorithm (Section 4.2.2). The results of the cross-correlation are overlapped to the corresponding results of the beam-navigator (green line) in (b). It appears evident that the motion detected with the two methods is synchronous. A plot showing the displacements measured with the self-navigation versus the corresponding displacements detected by the beam-navigator is shown in (c). The number of occurrences of all pairs of values, represented by the white dots, is color coded in the background and the linear regression is represented by the white line. The precision of the self-navigation is given by the acquired voxel size, 1.15 mm, whereas that of the beam-navigator was 1.0 mm. For this specific volunteer, the value of the PMCC was 0.94 and that of the slope of the linear regression was 0.54.

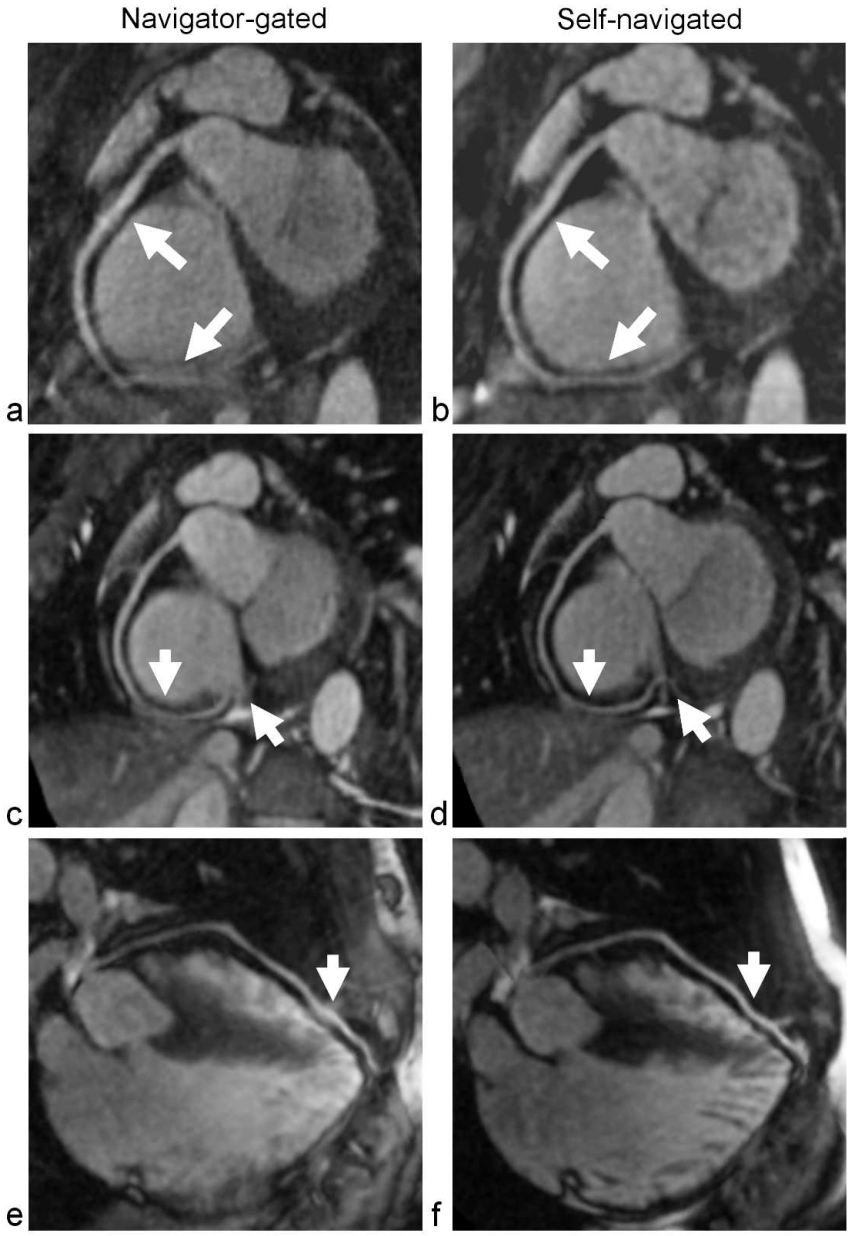

Figure 4.8: Reformatted images of the RCA (a-d) and of the LAD (e-f) are depicted for reference acquisitions obtained with the navigator-gated technique (a, c, e) and with the new self-navigation (b, d, f). In the specific case of (a), the low scan efficiency of the navigator-gated technique resulted in poor image quality. The white arrows in (a) and (b) highlight the proximal and the distal part of the RCA: the dataset acquired with self-navigation displays superior vessel sharpness and length. The white arrows in (c, e) and (d, f) highlight regions where the new method resulted in an improved delineation of the coronary vessels, in two cases where similar image quality was obtained with both approaches. However, minor blurring artifacts due to uncompensated residual motion can still be noticed.

	Reference vessel	Navigator-gated approach	Self-navigated approach	Significance of difference*
Detected/Total	RCA	10/10	10/10	
	LAD	9/10	10/10	
	LCX	8/10	8/10	
Vessel length [mm]	RCA	101.65 ± 23.72	113.46 ± 19.03	*N.S.*
	LAD	91.84 ± 39.46	99.52 ± 31.60	*N.S.*
	LCX	68.21 ± 12.88	71.62 ± 9.73	*N.S.*
Vessel sharpness	RCA	1.00 ± 0.23	1.09 ± 0.22	$p < 0.05$.
	LAD	1.03 ± 0.19	1.10 ± 0.24	*N.S.*
	LCX	1.16 ± 0.28	1.18 ± 0.22	*N.S.*
Scan time [min]		16.23 ± 6.28	6.07 ± 0.57	$p < 0.01$.
Scan efficiency [%]		41.16 ± 11.75	100 ± 0.0	$p < 0.01$.

* *N.S.* = Not Significant (Student t test)

Table 4.1: Numerical results and statistical significance of the comparison between the self-navigated acquisitions and the reference navigator-gated acquisitions. The acquisition time was more than halved with comparable results as for vessel sharpness and length.

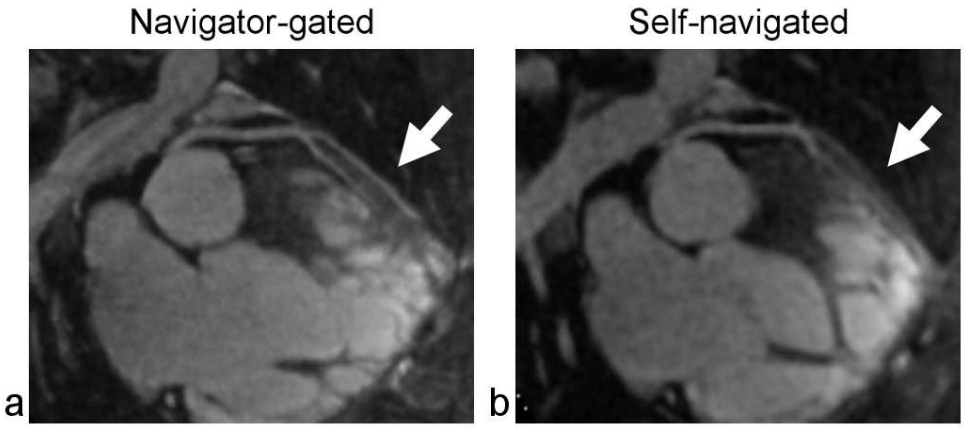

Figure 4.9: Reformatted images of the LAD of one of the examined subjects are depicted for the acquisition performed with navigator-gated approach (a) in comparison with the new self-navigated approach (b). For the specific subject, the total acquisition time of the navigator-gated dataset was as low as 14.8 min. While the distal part of the coronary vessel is well outlined in (a), the correspondent section is blurred in (b). In this case, the approximation of the respiratory motion to an SI translation proved to be inadequate to achieve a good image quality with self-navigation and residual blurring artifacts are clearly visible (white arrows). The extension of the proposed algorithm for motion correction to more complex motion models can potentially overcome this limitation in self-navigated acquisitions.

4.4 Discussion

The static bright signal from the lateral structures affects the result of the cross correlation such that the respiratory motion of the heart can not be adequately detected. This is confirmed by the insufficient or even failing motion detection in some of the volunteers and, in general, by the low values of the PMCC. The proposed method for the isolation of the blood pool shows to perform robustly in a number of subjects. The described technique for channel combination can be integrated in all modern MR systems where at least a set of L, M and R coil elements are available and where the absolute phase of the acquired signal is known separately for each element. In case anterior phased-array coils with smaller coil elements are used, similar results might be obtained by the simple selection of the central elements. However, as this method is introduced to address the specific problem of the suppression of the lateral bright signal in the SI projections, its adaptation to different applications, such as dark blood acquisitions, might not be straightforward. An alternative approach could be slab-selective excitation. In this case, nevertheless, monitoring of the required SAR and extension of the TR have to be considered. A substitute solution might be also found in the field of parallel RF transmission [Kats 06], which would allow spatially selective RF excitation.

The proposed automatic segmentation of the blood pool shows to improve the results obtained with the use of the complete SI projections after suppression of the lateral signal. Without segmentation, in fact, even if the good synchronicity and the high PMCC indicate the detection of respiratory motion, the low values of the slope of the linear regression imply that the result of the cross correlation is biased by the presence of static structures within the projections (ex: static bright signal on top of Fig. 4.7a). The proposed segmentation algorithm performs reliably as long as the FOV is placed correctly, i.e. if the blood pool is in the center. In case of an inadequately placed FOV, the quality control (Fig. 4.6) allows a prompt correction of the placement in an early stage of the acquisition, such that the temporal efficiency of the measurement is not affected. This control proved to be useful in particular with female volunteers, as the bright signal from the chest wall is not always completely suppressed by the anterior saturation slab. Moreover, the initial search range for the local maximum in the segmentation algorithm could be adapted for each acquisition to better fit the anatomy of each subject.

The superiority of the new self-navigated approach is confirmed by the strong visual synchronicity with the detection of the navigator and by the highest values of the PMCC. Fig. 4.7c shows that the linear relationship between the displacement of the heart and the diaphragm is not constant over all the respiratory cycle and is stronger close to end-expiration, where most of the samples are located, in agreement with the literature [Wang 95]. The average value of the slope of the linear regression is very similar to that recently reported in [Jahn 07]. The relatively high standard deviation of this value confirms that the correlation factor between the motion of the blood pool and the diaphragm is highly subject-dependent [Tayl 99]. The flat tops that can be observed in Fig. 4.7b originate from the fact that the precision of the cross correlation,

in the present implementation, is dictated by the actual image resolution. Since self-navigation allows to estimate the respiratory motion directly on the imaged organ, motion correction can be extended from the narrow gating window of the navigator to the full respiratory cycle. As a consequence, all interleaves of the self-navigated approach feed into image reconstruction. Hence, with the new method, the total acquisition time only depends on the average heart-rate of the examined subject and 100% success rate as well as 100% scan time efficiency are achieved. Moreover, the total duration of the measurement can be always estimated in advance. This feature makes the self-navigated method superior to navigator-gating both with respect to the planning of the single coronary MRI acquisition and for the integration of this technique into a complete cardiac examination.

The new method not only features major improvements in the detection of the coronaries in cases where navigator-gating is affected by very low scan efficiency (Fig. 4.8a, b), but also results in a slightly improved sharpness of the coronary vessels in cases where similar image quality is obtained with both acquisitions (Fig. 4.8c-f). As the acquisition protocol was the same for both methods, the average improvement in image quality obtained with the self-navigation is considered to be mainly related to the reduced total acquisition time (Section 1.2.3). In addition, the use of cross-correlation directly applied to the segmented blood pool makes the 1D motion correction performed with the new approach more reliable than with the navigated acquisitions, where the motion is estimated indirectly, on the diaphragm. Nevertheless, artifacts caused by uncompensated residual motion and non-linearities in self-navigated datasets suggest that the approximation of the respiratory motion to an SI translation is not always adequate [McLe 02, Wang 95]. In particular, Fig. 4.9 provides an example where a better result was achieved with the navigator-gating technique. This can be explained by the fact that, as the acquisition is performed consistently within the same respiratory phase, all motion components are intrinsically minimized in a navigator-gated setup. A similar effect could be obtained in self-navigation by selecting the reference SI projection "a posteriori" among the interleaves acquired during end-expiration [Picc 13a]. This would allow to maximize the number of interleaves acquired during the reference respiratory position and, thus, to minimize the number of 1D corrections. A sub-pixel precision of the 1D motion detection would be possible with the use of interpolation on the SI projections. Nevertheless, for a real improvement of the self-navigated method, the extension of the motion correction to more complex motion models needs to be explored first. An extended projection-based approach that makes use of the 3D positional information contained in all projections of the 3D radial trajectory is one possibility [Wieb 01]. Affine motion correction [Mank 02, Mank 03], furthermore, can be achieved with techniques based on image registration [Bhat 11].

Beyond these extensions, the possibility to perform coronary MRI at 3T would allow to obtain higher SNR and, therefore, to aim towards an improved spatial resolution [Bi 05, Xie 10]. If issues regarding the effectiveness of the T2 preparation [Neza 09], fat saturation and off-resonance artifacts [Shah 09] are efficiently addressed at 3T, the presented method can be straightforwardly applied also to this setup. Further-

more, acceleration of the acquisition process could be obtained using reconstruction methods that exploit the redundancy of the information contained in the image. As the signal combination based on the coil elements is used only for self-navigation, parallel imaging performances remain unaffected. In addition, the use of iterative reconstruction methods, such as compressed sensing [Lust 07], applied to radial 3D [Done 08], might be considered. If the acquisition time is highly reduced, a more comfortable examination for the patient can be provided and the probability of involuntary motion of the examined subject is reduced. Eventually, if a high acceleration of the acquisition is achieved, applications of the current method in dynamic studies, e.g. whole-heart cine or perfusion MRI, might be considered.

4.5 Conclusion

The described self-navigation method, implementing automatic isolation and segmentation of the blood pool, achieves a high overall reliability and 100% scan time efficiency with respect to the respiratory motion. This technique outperforms the existing navigator-gated approaches for simplicity of the examination setup, efficiency and total scan time. In average, the total duration of the acquisition is reduced by more than 60%. Moreover, with the new implementation, not only whole-heart coronary MRI can be performed without the use of a respiratory beam-navigator, but the robustness and the success rate of the acquisition are highly improved by the use of cross-correlation as 100% success rate is achieved. Furthermore, comparable or slightly superior results in image quality with respect to the current navigator-gated techniques are obtained. For these reasons, the described self-navigated approach is already appealing for extensive clinical studies, some of which have been already started. Finally, such approach offers a sound basis for a future extension of the motion correction to models of higher complexity.

Chapter 5

Patient Studies

The aim of this chapter is to evaluate the image quality and diagnostic performance of the self-navigated whole-heart MR acquisition described in the previous chapter for the detection of coronary artery disease (CAD) as well as for the identification of congenital anomalies of the heart and the coronary arteries. To enable initial testing of this sequence in patients, the time gap between perfusion imaging and 2D late gadolinium enhancement (LGE) in routine clinical scans was exploited without affecting the overall scan time. Major parts of this chapter are published in [Picc 14].

5.1 Motivations

5.1.1 Premises

As described at the beginning of this thesis (Chapter 1), whole-heart MRA has shown to be an appealing non-invasive and radiation free alternative to X-ray coronary angiography for the detection of coronary artery stenoses. The importance of this potential is even enhanced when considering that, in average, up to 40% of the patients routinely examined with X-ray is found to have no significant coronary artery stenosis [Diss 02]. Coronary MR angiography is also suited for assessing coronary arteries in children and young adults, because the cancer risk from radiation exposure is even higher in this population [Klei 06]. In addition, free-breathing, whole-heart MR imaging has demonstrated to be clinically relevant for the assessment and follow up of congenital heart diseases (CHD)[Tang 11], as well as for the planning of electrophysiology procedures.

5.1.2 Research Contributions

It appears clear how the expertise of the user, as well as the accurate planning of the scan and its total duration, play a fundamental role on the final image quality of a navigator-gated coronary MR acquisition [Saku 11]. Additionally, as the standard examination time per patient is usually strictly limited by the schedule of the clinical MR system, the inclusion of a scan with unknown duration, i.e. dependent on the respiratory pattern of the patient, is quite problematic. The 3D whole-heart self-navigated technique described in Chapter 4, however, can overcome all these drawbacks. Self-navigation performs motion detection and correction directly using the readouts acquired for imaging and allows for: an acceptance rate of 100%, simplified examination planning, a priori knowledge of the duration of the acquisition regardless of the individual respiratory patterns, and improved accuracy of the motion compensation. For these reasons, it becomes possible to attempt a first optional integration of the whole-heart self-navigated coronary MRA sequence into a complete clinical cardiac MR routine exam, with minimal or no impact on the total examination time. As the performance of self-navigation hinges on myocardium-blood contrast, and provided that there is often a time gap between perfusion imaging and late gadolinium enhancement (LGE) imaging in routine clinical protocols, high-resolution self-navigated 3D whole-heart imaging may be performed to obtain information on both the general cardiac anatomy and the coronary tree. This first patient study was conducted with the Cardiac MR Center at the university hospital of Lausanne (CHUV), in Switzerland. The goal of this study was to assess, in a clinical setting, the image quality and diagnostic performances of the self-navigated whole-heart sequence described in the previous chapters of this thesis. To the best knowledge of the author, this is the first clinical evaluation of a whole-heart self-navigated coronary MRA sequence. The acquired datasets were assessed by experts in the field of coronary MRA, for evaluation of both qualitative and quantitative endpoints for all coronary arteries. Furthermore, the diagnostic information contained in the acquired data was analysed with the help of four experienced cardiologists, with respect to CAD, CHD and coronary arterial anomalies and variants (CAAV). In this chapter, preliminary results on 78 patients are reported.

5.2 Materials and Methods

5.2.1 Study Population

A total of 78 patients with a mean age of 48.5 ± 20.7 years and age range of $8 - 82$ years (53 men, mean age 50.0 ± 19.3 years and age range $14 - 82$ years; 25 women, mean age 45.4 ± 23.4 and age range $8 - 79$ years) were examined. There was no significant difference in age between the male and female subjects ($p = 0.371$, using a two-sample, two-tailed, Student t test). The average body-mass index was 24.3 ± 4.6 kg/m^2. Patients were referred to cardiac MR (CMR) for known or suspected CAD (n=40), congenital anomalies (n=17), evaluation of a cardiomyopathy (n=14) and other subcategories (n=7). All patient indications are reported in Tab. 5.1. In the current study no specific exclusion criteria were applied and the MRA datasets

from all 78 patients were included in the final quantitative analyses. This study was approved by the local ethics committee at the University Hospital in Lausanne (Commission cantonale (VD) d'éthique de la recherche sur l'être humain).

Indications for CMR	Stress Perf.	MR Angio	LGE	X-ray
Suspected CAD (n=18)	18/18	2/18	18/18	2/18
CAD - Ischemia (n=11)	11/11	0/11	11/11	9/11
CAD - Viability (n=11)	0/11	0/11	11/11	10/11
Cardiomiopathy (n=14)	0/14	1/14	14/14	5/14
Congenital Anatomy (n=16)	1/16	15/16	7/16	1/16
Coronary Abnormality (n=1)	0/1	0/1	1/1	1/1
Others (n=7)	0/7	3/7	5/7	3/7
Total (n=78)	30/78	21/78	67/78	31/78

Table 5.1: Patient indications: the patient cohort was subdivided in seven categories with common indications for cardiac MR. The last category (Others) includes e.g. workup of valvular disease and right ventricular assessment in pulmonary hypertension.

5.2.2 Coronary MRA Data Acquisition

All examinations were performed on a 1.5T clinical MRI scanner (MAGNETOM Aera, Siemens AG, Healthcare Sector, Erlangen, Germany). Thirty elements of the anterior and posterior phased-array coils were activated for signal reception. Data acquisition was performed using the 3D radial trajectory with a spiral phyllotaxis pattern [Picc 11], adapted for self-navigation as described in [Picc 12]. The self-navigated scan did not require any extra localizer and the planning of the whole-heart acquisition only included the placement of the cubic FOV around the heart as seen on the very first scout scan used for cardiac imaging. A saturation slab at the level of the anterior chest wall was also localized on this scout. Motion detection, correction and image reconstruction were performed automatically and in real time on the console of the system. All measurements were performed using k-space segmentation and ECG-triggering. For the acquisition of each k-space segment, both T2-preparation (TE=40 ms) and fat saturation were added prior to bSSFP image data acquisition. In all patients, a total dose of 0.2 mmol/kg of Gadobutrol (Gadovist, Bayer Schering Pharma, Zurich, Switzerland) was administered. Specifically, the dose was injected as a single bolus of 0.2 mmol/kg for viability assessment (n=27) and for angiography of the great vessels (n=11), or 0.1 mmol/kg for each a viability and angiography assessment (n=10), or as a bolus of 0.1 mmol/kg for first-pass assessment during adenosine, completed by a bolus of 0.1 mmol/kg at rest (n=30). Immediately after administration of the total dose, stacks of axial, sagittal, and coronal volume interpolated breath-hold

examination (VIBE) images were acquired for assessment of thoracic anatomy. After completion of these anatomical images, i.e. approximately 4 minutes after the last injection, the 3D self-navigated imaging was performed with the following parameters: TR/TE 3.1/1.56 ms, FOV (220 mm)^3, matrix 192^3, acquired voxel size (1.15mm)3, radio frequency (RF) excitation angle 115Âř, and receiver bandwidth 900 Hz/px. A total of about 15000 radial readouts were acquired in 377 (acquisition window (AW) = 100 ms) or 610 (AW = 75 ms) heartbeats, depending on the individual heart rate of each patient (20), and with an overall sampling ratio of 20% of the Nyquist limit. The trigger delay was set by the cardiologist operating at the scanner using visual inspection of the most quiescent mid-diastolic period on a mid-ventricular short axis cine image series acquired prior to the injection of the contrast agent. The performance of the self-navigation module was assessed during acquisition, using the inline display, as described in [Picc 12] (Fig. 4.6). The heart rate of all patients was recorded during the routine 2D cine acquisitions before contrast injection and used to compute the expected duration of the self-navigated whole-heart scan. The actual duration of the whole-heart scan was assessed for comparison.

5.2.3 Coronary Arteries and Image Quality

The proximal, mid and distal segments of the right coronary artery (RCA), and of the left anterior descending artery (LAD), the left main stem (LM) and the proximal segment of the left circumflex artery (LCX) were identified and classified following the guidelines of the American Heart Association [Aust 75]. All segments were graded on a 5-point scale for image quality by two experts (Prof. Matthias Stuber (M.S.), PhD, Department of Radiology, University Hospital (CHUV) and University of Lausanne (UNIL) / Center for Biomedical Imaging (CIBM), Lausanne, Switzerland and the author of this thesis (D.P.)), adapted from [McCo 97] using consensus reading as proposed in [Kim 01a]. The scale grades border definition of the coronary arteries as follows: 0 = not visible, 1 = markedly blurred, 2 = moderately blurred, 3 = mildly blurred and 4 = sharply defined. Any segment with grade > 0 was considered as âĂIJvisualizedâĂİ. The two experts were completely blinded towards the patient indications or clinical conditions. The percentage vessel sharpness was then also computed for all the visualized coronary segments, using an approach similar to that described in reference [Etie 02]. In this approach, first the analysed vessel is projected into a 2D plane using an algorithm for multiplanar reformatting. Edge filtering is then applied to the 2D image and the point-wise sharpness of the coronary vessel is computed as the difference between the maximum intensities of the edges of the vessel border and the local background signal. The sharpness of the specific vessel segment included in each 2D reformat is then reported as a percentage value of the ratio between the mean sharpness along the whole segment and the maximum difference of signal intensity. Furthermore, visual vessel length was measured for both the right and left coronary system using CoronaViz 2.0 (Work in Progress software, SCR, Princeton, NJ, USA). Vessel diameter was computed for all visualized coronary segments.

5.2.4 Coronary Arteries and Diagnosis of CAD

On the MR images, a double-blinded evaluation for the detection of significant luminal coronary disease on the LM, RCA, LAD and proximal LCX was performed for all patients by consensus reading, while the observers (M.S. and D.P.) did not know whether an X-ray coronary angiogram would be available for comparison in a given patient, nor the specific indications for CMR. The stenoses on the X-ray angiograms were independently identified and graded ($> 50\%$ of the vessel diameter considered significant) by an experienced clinician (Christophe Sierro (C.S.), MD, Division of Cardiology and Cardiac MR Center, University Hospital of Lausanne (CHUV), Lausanne, Switzerland). After unblinding, sensitivity and specificity were computed on the proximal and mid segments of the coronary vessels that were available for analysis with both modalities. Per-patient, per-vessel and per-segment analyses are reported.

5.2.5 Statistical Analysis

In order to assess any significant difference in image quality between coronary segments, all segments were binned in three groups: proximal (including prox. RCA, LM, prox. LCX and prox. LAD), mid (including mid RCA and mid LAD) and distal (including dist. RCA and dist. LAD). Quality grades and percentage vessel sharpness were compared among the three groups as follows. First, a one-way ANOVA was used to test whether an effect was present among the means of the three groups. A $p \leq 0.05$ was considered statistically significant. When an effect was found, multiple paired two-tailed Student t test were performed with a $p \leq 0.017$ considered statistically significant after Bonferroni adjustment for multiple comparisons (0.05/3), as described in [Tell 03]. As for the vessel visualization (grade > 0), the odds of visualized/non-visualized were computed for each of group. Odds ratios (OR) and their 95% confidence intervals (CI95%) were then computed among the three groups as described in [Medi 03]. All statistical analyses were performed with Excel 2007 (Microsoft, Bothell, Wash), except for the ANOVA tests that were performed in Matlab v7.13 (Mathworks, Natick, MA). Sensitivity and specificity values were calculated using Excel 2007.

5.2.6 Congenital Heart Disease

The performance of the whole-heart self-navigated technique was also tested for visualization of congenital malformations of the general heart anatomy as well as of the coronary arteries by assessing the origin, anatomy, and relationship of the proximal coronary arteries with the cardiac anatomy and the great vessels. The assessment of the CHD cases was performed by an experienced cardiologists, with specialization in congenital malformations (Pierre Monney (P.M.), MD, Division of Cardiology and Cardiac MR Center, University Hospital of Lausanne (CHUV), Lausanne, Switzerland). Examples of CHD examined in this study included: transposition of the great arteries, univentricular heart, and aortic malformations.
In comparison with a normal cardiac anatomy (Fig. 5.1a), the pathology known as transposition of the great arteries (TGA) is characterized by a ventriculo-arterial discordance, in which the aorta (Ao) is connected to the right ventricle (RV), while the

main pulmonary artery (MPA) is connected to the left ventricle (LV) (Fig. 5.1b). Systemic and pulmonary circulations run parallel, such that de-oxygenated blood from the organs does not circulate through the lungs. Among the anatomically relevant differences it can be noted that aorta and pulmonary artery do not cross, but are parallel. This congenital condition is not compatible with life and intracardial shunt surgery is mandatory after birth. In this context, atrial switch (Mustard operation) was the best available option for palliative surgery until the year 2000, when the more technically challenging arterial switch (Jatene operation) became more routinely performed. In the Mustard operation, a *trousers-shaped* patch in the atria is performed to redirect the venous blood from the superior and inferior vena cava (SVC and IVC) to the LV and the oxygenated blood from the pulmonary veins (PV) to the RV (Fig. 5.1c). After surgery, the circulation is no more parallel, but in series and the *weak* RV becomes the systemic ventricle.

In comparison with normal cardiac anatomy (Fig. 5.2a), a condition where the tricuspid valve did not develop and the right atrium-ventricular plane is not perforated is defined as tricuspid atresia (Fig. 5.2b). Systemic venous blood is diverted to the left atrium through a large atrial septal defect (ASD) and mixed to the oxygenated pulmonary venous blood (cyanotic condition). There is usually an associated ventricular septal defect (VSD) communicating to a rudimentary RV or outlet chamber to which the pulmonary artery is connected. The only effective pumping chamber is the LV and the condition is that of a functionally univentricular heart. A last-option palliative surgery for univentricular hearts is known as Fontan circulation (Fig. 5.2c). The systemic venous return is directly diverted to the pulmonary artery, completely bypassing the cardiac chambers and the pulmonary artery is disconnected from the ventricle. As a consequence, the blood flow to the lungs becomes passive and a low-resistance pulmonary circulation is a prerequisite for the success of such palliative surgery. Sometimes, a transient fenestration between the IVC conduit and the RA, with secondary closure is necessary.

In comparison with a normal anatomy of the superior aorta (Fig. 5.3a), frequent aortic malformations include aortic aneurysms (Fig. 5.3b) and aortic coarctation (Fig. 5.3c). For diagnostic purposes it is very important to be able to precisely measure the diameter of the aorta at various locations.

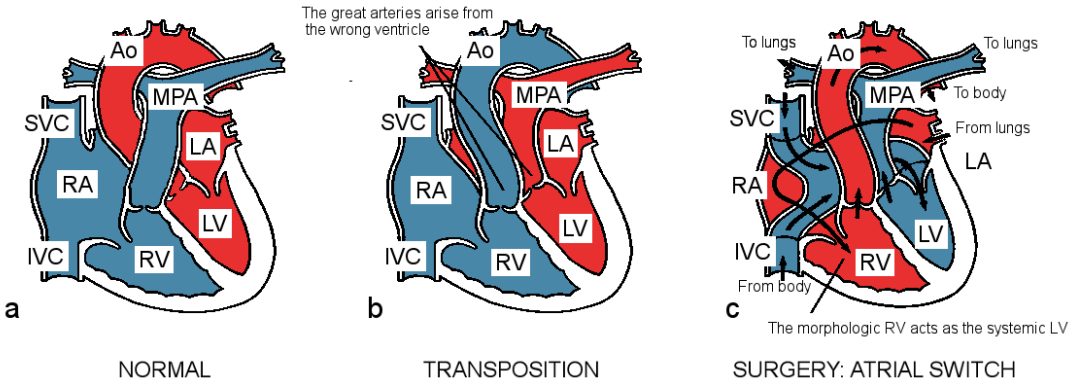

Figure 5.1: In comparison with a normal cardiac anatomy (a), the pathology known as transposition of the great arteries is characterized by a ventriculo-arterial discordance, in which the aorta is connected to the RV, while the main pulmonary artery is connected to the LV (b). In the Mustard operation, a *trousers-shaped* patch in the atria is performed to redirect the venous blood from the SVC and IVC to the LV and the oxygenated blood from the PV to the RV (c). After surgery, the circulation is no more parallel, but in series and the *weak* RV becomes the systemic ventricle.

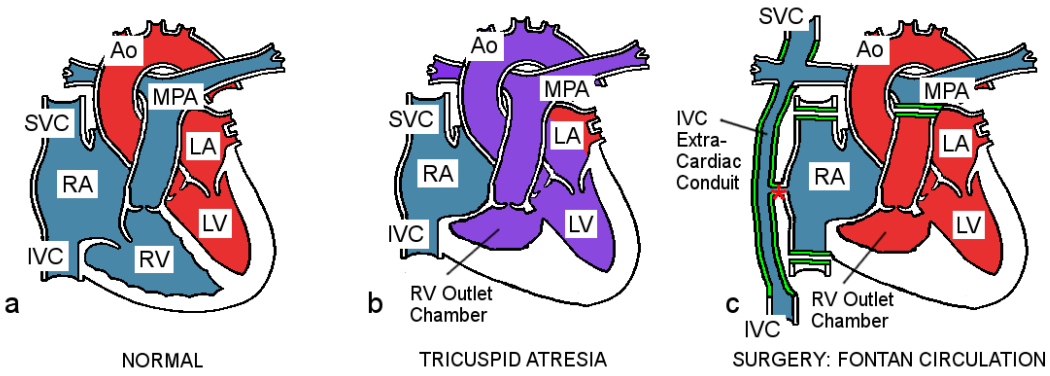

Figure 5.2: In comparison with normal cardiac anatomy (a), a condition where the tricuspid valve did not develop and the right atrium-ventricular plane is not perforated is defined as tricuspid atresia (b). A last-option palliative surgery for univentricular hearts is known as Fontan circulation (c). The systemic venous return is directly diverted to the pulmonary artery, completely bypassing the cardiac chambers and the pulmonary artery is disconnected from the ventricle. Sometimes, a transient fenestration between the IVC conduit and the RA, with secondary closure (*) is necessary.

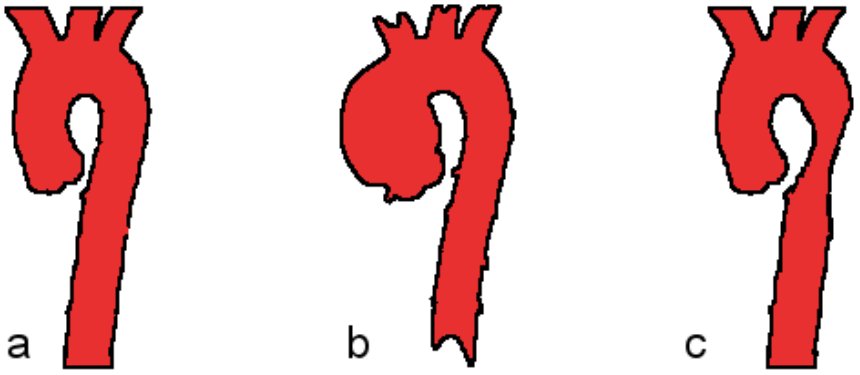

Figure 5.3: In comparison with a normal anatomy of the superior aorta (a), frequent aortic malformations include aortic aneurysms (b) and aortic coarctation (c). For diagnostic purposes it is very important to be able to precisely measure the diameter of the aorta at various locations.

5.3 Results

In the patients population studied, the prevalence of cardiovascular risk factors was in line with a population of known or suspected CAD, with 30.8% of patients with positive systemic arterial hypertension (50% negative, and 19.2% unknown), 25.7% positive hypercholesterolemia (53.8% negative, and 20.5% unknown), and somewhat lower prevalence for other risk factors (e.g. 10.3% diabetes mellitus, 14.1% positive family history, and 15.4% smokers). In all patients, coronary MRA data acquisition was successfully completed. The average predicted acquisition time, based on the heart rate measured during the cine acquisitions, was 7.38 ± 1.85 min and the measured time for the 3D whole-heart self-navigated protocol was 7.84 ± 1.88 min. A high linear correlation and almost unitary slope ($R2 = 0.88$, slope $= 0.95$) were found between the expected and measured scan times for all patients, as shown on the scatter plot in Fig. 5.4.

Some examples of the 3D self-navigated whole-heart acquisitions are reported in Fig. 5.5,Fig. 5.7, and Fig. 5.6, displayed in a coronal (a), sagittal (b) and axial (c) view. All patient descriptions are courtesy of Pierre Monney, MD.
Fig. 5.5 shows the case of a 34 years old male patient with a mild form of tetralogy of Fallot (aorta overriding the inter-ventricular septum, mal-alignment ventricular septum defect (VSD), pulmonary or sub pulmonary stenosis and right ventricular hypertrophy). This patient underwent late surgical correction at age 31 with patch closure of the VSD and implantation of a valved conduit (Contegra 22 mm) between the right ventricle and the pulmonary artery. He was referred for CMR to quantify the degree of pulmonary regurgitation through the conduit, which was suspected to be severe by echocardiography. The multiplanar reformat in (d) shows normal origin and course of the coronary tree.
Fig. 5.7 shows the dataset of a 17 years male patient, born with the shone complex (association of stenosis of the left ventricle outflow at various levels). Coarctation of

the aorta and aortic valve stenosis were diagnosed. The patient had a surgical repair of the coarctation during childhood and underwent a Ross operation at the age of 14 for severe aortic valve stenosis. Surgery included the implantation of the autologous pulmonary valve in aortic position and implantation of a bovine valved conduit in pulmonary position. The procedure was complicated by and an endocarditis of the valved conduit one year later, resulting, despite aggressive antibiotic treatment, into a stenosis of the conduit. He recently underwent a percutaneous pulmonary valve implantation, which is visible as a extended dark artifact in (b). Cardiac MRI was requested to asseess the right ventricular volume and function. The multiplanar reformat in (d) nicely depicts the whole coronary tree, where the anomalous left coronary artery originates from the non-coronary sinus.
Fig. 5.6 shows the dataset of a 77 years old male patient with multiple cardiovascular risk factors and 3-vessels disease who had a coronary artery bypass grafting (CABG) at the age of 72 using the left internal mammary artery (LIMA) to the mid LAD and a sequential saphenous vein graft to the distal LCX (multiplanar reformat in d). The X-ray angiography of the saphenous bypass is reported in (e) for direct comparison. He was referred for stress perfusion MRI because of ongoing, although atypical, exertional chest pain A more complete analysis on the visualization of coronary bypass grafts with the self-navigated sequence is published in [Copp 13b].

5.3.1 Coronary Arteries and Image Quality

The number of visualized coronary segments, the average quality grades, vessel sharpness, vessel length, and vessel diameter for all coronary segments are reported in Table 5.2. The quality grades and the vessel sharpness of the LM, proximal LAD and proximal and mid RCA were in average higher than those of the respective distal segments.

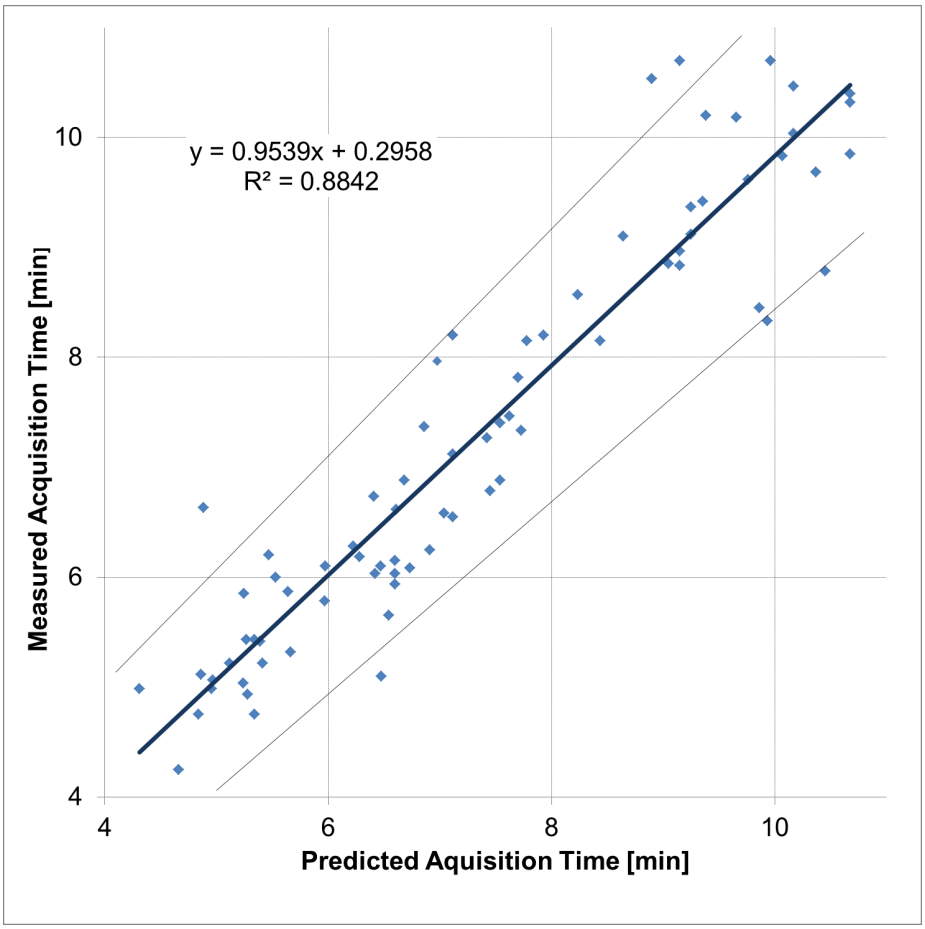

Figure 5.4: Scatter plot of the predicted and measured duration of the whole-heart, high resolution acquisitions for all patients. The expected duration can be calculated simply by multiplying the average RR interval of the patients for the number of acquired heart-beats. The intercept of the regression line (in blue) is only slightly above zero (0.298) and the slope is almost equal to one (0.954). The CI95% is also displayed (in black). This intuitively shows how scan time becomes predictable as all the acquired data are used for the final reconstruction.

Coronary Segment	**LM** (16.6 ± 4.5 [mm]:)	**LAD** (68.6 ± 33.4 [mm]): Prox.	Mid	Dist.
Visualized:	76/78	71/78	61/78	44/78
Grade:	2.0 ± 0.9	1.8 ± 1.1	1.3 ± 0.9	0.7 ± 0.7
Sharpness [%]:	42.0 ± 11.6	39.5 ± 10.2	35.2 ± 10.3	37.2 ± 10.0
Diameter [mm]:	3.5 ± 0.6	2.9 ± 0.5	3.0 ± 0.5	2.9 ± 0.6
Coronary Segment	**LCX** (31.0 ± 21.9 [mm]:) Prox.	**RCA** (82.0 ± 41.1 [mm]): Prox.	Mid	Dist.
Visualized:	65/78	76/78	70/78	43/78
Grade:	1.2 ± 0.8	1.8 ± 1.0	1.5 ± 1.0	0.7 ± 0.5
Sharpness [%]:	39.2 ± 8.9	37.5 ± 12.8	36.6 ± 11.8	24.2 ± 7.5
Diameter [mm]:	3.1 ± 0.5	3.0 ± 0.8	2.8 ± 0.6	2.9 ± 0.7

Table 5.2: Quantitative results: Quantitative results of the image quality of the coronary arteries in all 78 patients. The visual quality grades and, the vessel sharpness, diameter and length are given as a mean ± one standard deviation. The average total sampled length of each artery is mentioned after its abbreviation.

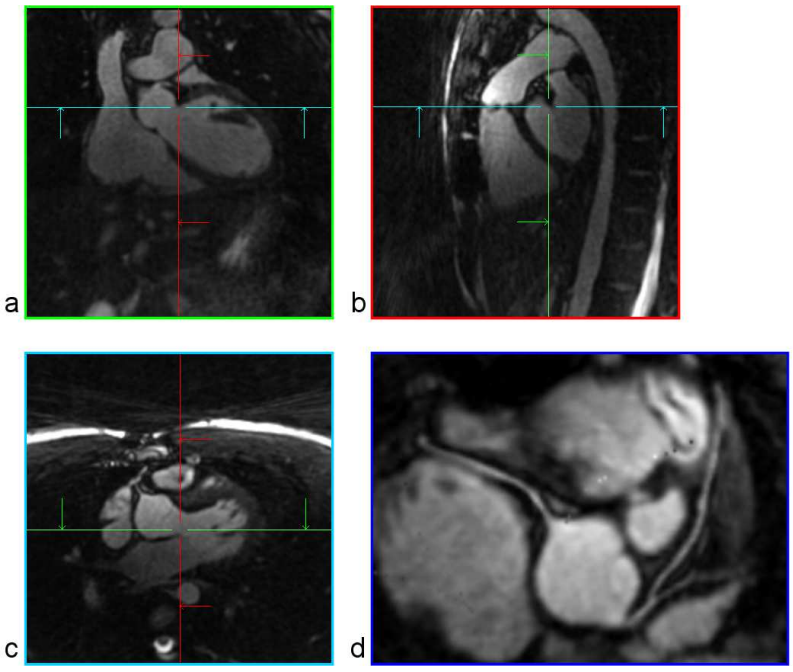

Figure 5.5: Example of whole heart dataset acquired with the self-navigated sequence displayed in a coronal (a), sagittal (b) and axial (c) view. The patient is a 34 years old man with a mild form of tetralogy of Fallot. The multiplanar reformat in (d) shows normal origin and course of the coronary tree.

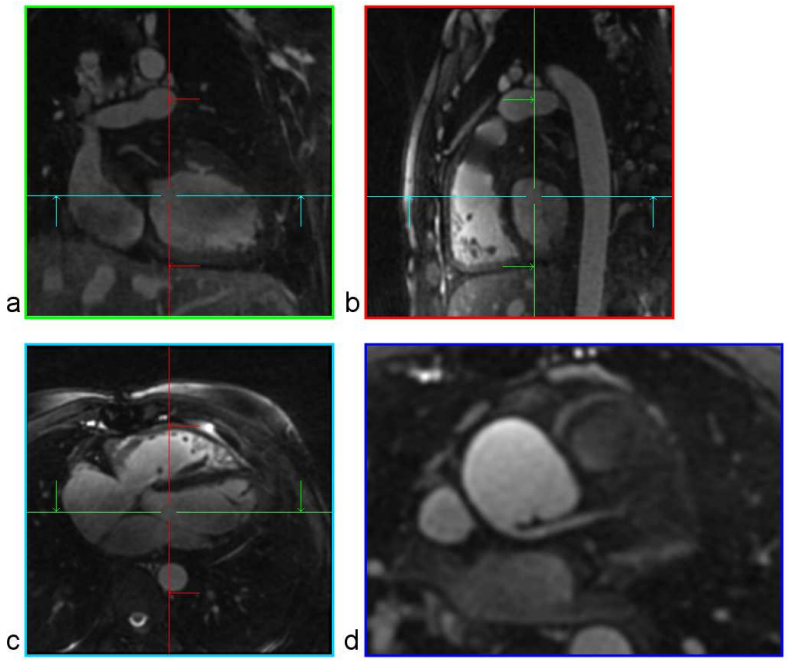

Figure 5.6: Example of whole heart dataset acquired with the self-navigated sequence displayed in a coronal (a), sagittal (b) and axial (c) view. The patient is a 17 years old male, born with the shone complex. The multiplanar reformat in (d) nicely depicts the whole coronary tree, where the anomalous left coronary artery originates from the non-coronary sinus.

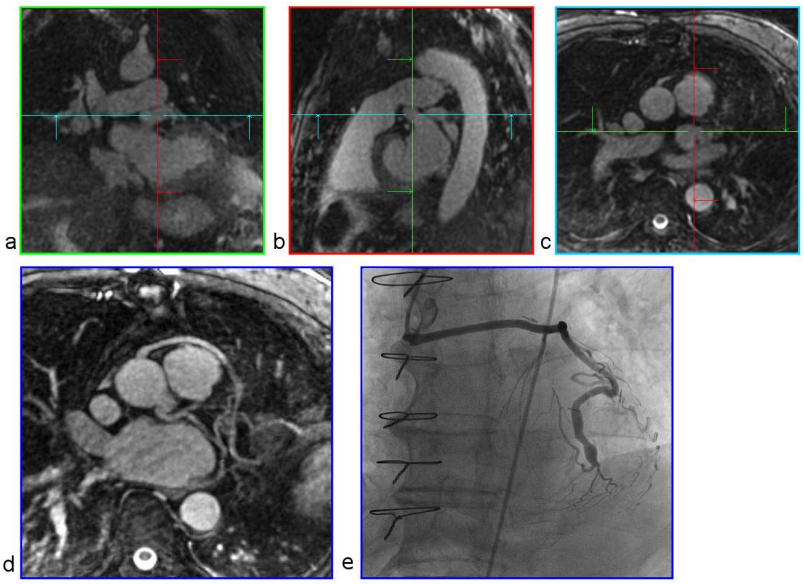

Figure 5.7: Example of whole heart dataset acquired with the self-navigated sequence displayed in a coronal (a), sagittal (b) and axial (c) view. The patient is a 77 years old man with multiple cardiovascular risk factors and 3-vessels disease who had a coronary artery bypass grafting (CABG) at the age of 72. A saphenous vein graft to the distal LCX is shown in the multiplanar reformat in (d). The X-ray angiography of the saphenous bypass is reported in (e) for a direct comparison.

5.3.2 Coronary Arteries and Diagnosis of CAD

After unblinding, it was found that X-ray coronary angiograms were available in 31 of the 78 patients. Two datasets were excluded from the analysis due to the low image quality of the MRA (quality grade = 0), in which the coronary arteries could not be visualized. For the remaining 29 patients, the majority of the X-ray angiograms were obtained before (n=22) the MRA scan (n=2 on the same day, n=5 MRA first). In these patients, n=3 had a time gap of more than 90 days with respect to the MRA scan, while the average time between the two examinations was 45 days. The LM and RCA were assessed in all 29 X-ray images, while images of the LAD and LCX were available in 28 cases. The double-blinded comparison of self-navigated whole-heart coronary MRA with X-ray angiography resulted in an overall per-patient sensitivity and specificity of 71.4% (15/21) and 62.5% (5/8), respectively for the detection of significant coronary artery disease in the proximal and mid segments. The total per-vessel sensitivity and specificity on the proximal and mid segments of the coronary vessels were 64.7% (22/34) and 85.0% (68/80), respectively, on the total of 114 coronary vessels examined. The values for each vessel are reported separately in 5.3. Considering proximal and mid segments of each coronary artery separately, sensitivity and specificity reached an overall per-segment value of 46.2% and 82.6%, respectively. In Fig. 5.8, example reformats of the left and right coronary artery system, obtained with the 3D self-navigated approach (a, c, e) in patients with X-ray angiographically defined coronary artery disease are displayed. The corresponding X-ray coronary angiograms are shown in Fig. 5.8b, d and f. On the coronary MRA in Fig. 5.8a, the lesion in the proximal LAD and just distal to the take-off of a diagonal branch can clearly be identified. This is confirmed on the X-ray angiogram in Fig. 5.8b. While the lumen narrowing of the proximal RCA on the MRA shown in Fig. 5.8c can clearly be identified, the further course of this artery is obscured in the region of a stent. In Fig. 5.8e another representative example is displayed where significant disease is identified in the proximal LAD on MRA and confirmed on the corresponding X-ray coronary angiogram.

Comparison with X-ray	**Sensitivity**	**Specificity**
Per-patient:	71.4%(15/21)	62.5%(5/8)
Per-vessel (total):	64.7%(22/34)	85.0%(68/80)
LM:	50.0%(1/2)	92.3%(26/27)
LAD (prox. + mid):	66.7%(10/15)	92.3%(12/13)
LCX (prox.):	33.3%(1/3)	88.0%(22/25)
RCA (prox. + mid):	71.4%(10/14)	53.3%(8/15)
Per-segment:	46.2%(18/39)	82.6%(109/132)

Table 5.3: Sensitivity and specificity of the proposed technique for the detection of CAD: Results are proposed per-patient, per-vessel and per-segment.

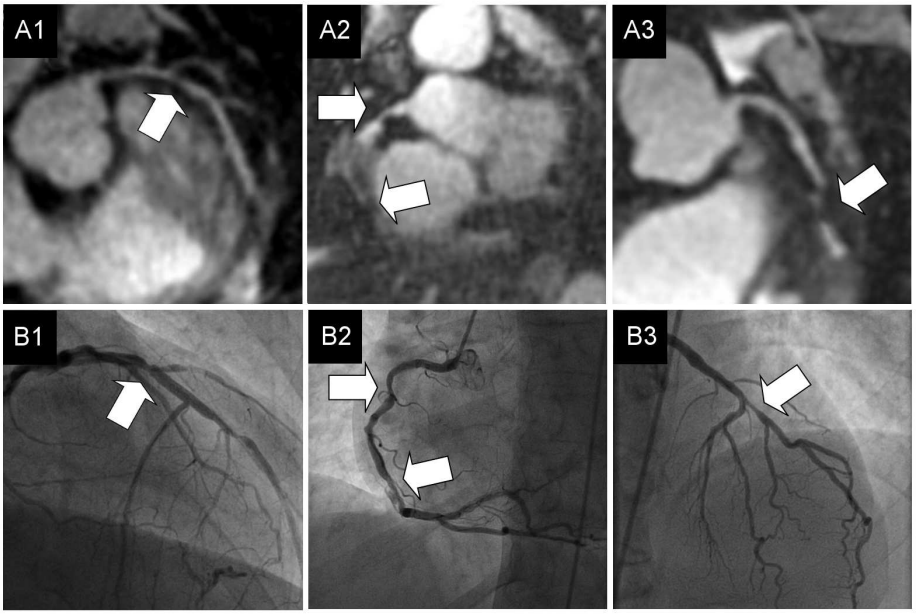

Figure 5.8: Example comparing multiplanar reformats of the whole-heart self-navigated coronary MRI datasets (A) with the correspondent X-ray coronary angiograms (B). A significant stenosis of the mid LAD, highlighted by the white arrow, can be clearly identified with both modalities (1). Two interstent re-stenoses (white arrows) of the proximal RCA between two stents are well visible in both MRI reformats and X-ray (2). The bright artifact between the two stenoses in (A2) is caused by the implanted stent. Another example of significant stenosis of the mid LAD (arrow) is displayed in (3). The X-ray images are courtesy of Christophe Sierro, MD.

5.3.3 Statistical Analysis

The mean grades for the proximal, mid and distal segment groups were 1.7 ± 1.0, 1.4 ± 1.0 and 0.7 ± 0.8, respectively. The average percentage vessel sharpness values for the proximal, medial and distal segment groups were 39.5 ± 11.2, 35.9 ± 11.1 and 29.1 ± 10.6, respectively. In both cases, the ANOVA test revealed a significant effect ($p = 6.5e - 23$ for the grades and $p = 9.5e - 10$ for the sharpness). From the t tests a statistical difference was found among all three groups for both quality grades and vessel sharpness ($p < 0.017$). A proximal coronary segment was found to be 2.3 times more likely to be visualized, when compared to mid segments ($OR_{prox-mid} = 2.3$, CI95% $= [1.3, 4.2]$). A mid coronary segment was 4.2 times more likely to be visualized with respect to a distal segment ($OR_{mid-dist} = 4.2$, CI95% $= [2.4, 7.1]$), while the visualization ratio between proximal and distal segments was 9.5 ($OR_{proxdist} = 9.5$, CI95% $= [5.6, 16.1]$). All these values were found to be statistically significant as per [Medi 03].

5.3.4 Congenital Heart Disease

Anomalous cardiac anatomy, origin and course of the coronary arteries could be very well visualized in all congenital cases. One example for each of the CHD cases described in the Methods section is reported: Fig. 5.9 for the transposition of the great arteries, Fig. 5.10 for the tricuspid atresia, and Fig. 5.11 for aortic aneurysm. All anatomical landmarks described in the methodology could be identified and are reported in the figures. Examples of anomalous origin and course of the coronary arteries in cases of CAAV are reported in Fig. 5.12 and Fig. 5.13.

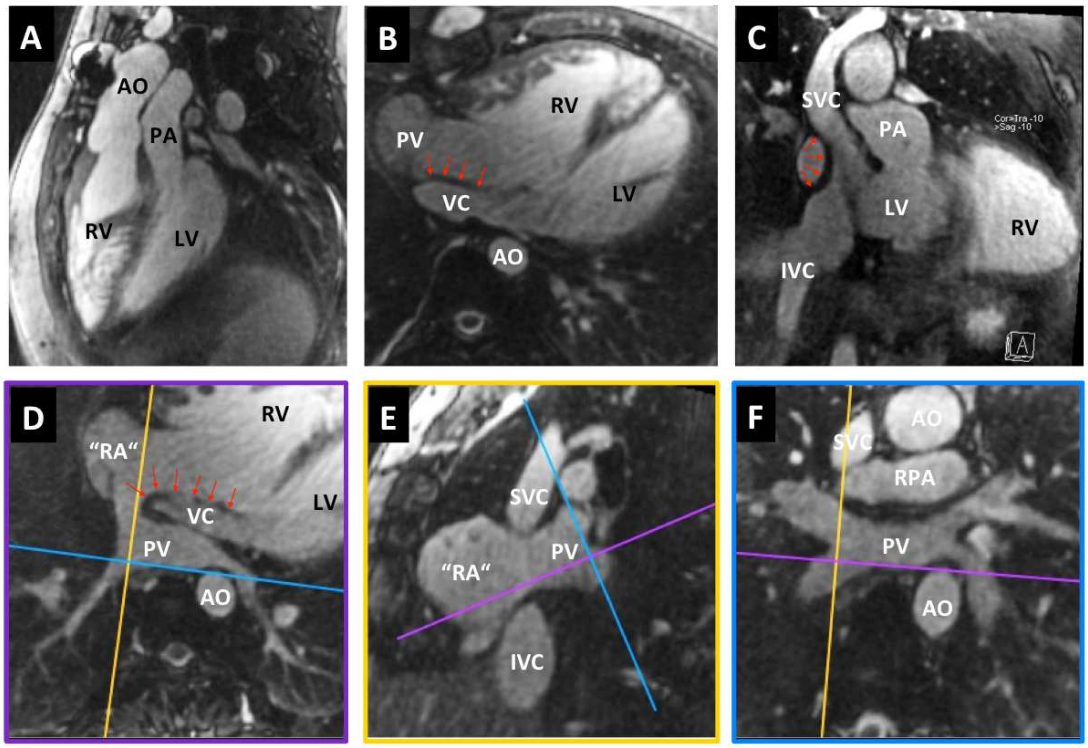

Figure 5.9: Example of transposition of the great arteries corrected by atrial switch (Mustard operation). The ventriculo-arterial discordance, with the aorta anterior and running parallel to the pulmonary artery (PA) is visible in (A). The systemic atrial pathway, connecting the caval veins to the left ventricle can be visualized in (B) and (C). The red arrows indicate the inter-lateral baffle. The pulmonary atrial pathway, connecting the pulmonary veins to the systemic right ventricle is displayed in (D-F). The three figures in the bottom row have orthogonal orientations, highlighted by the coloured axes. These images are courtesy of Pierre Monney, MD and are published in [Monn 13].

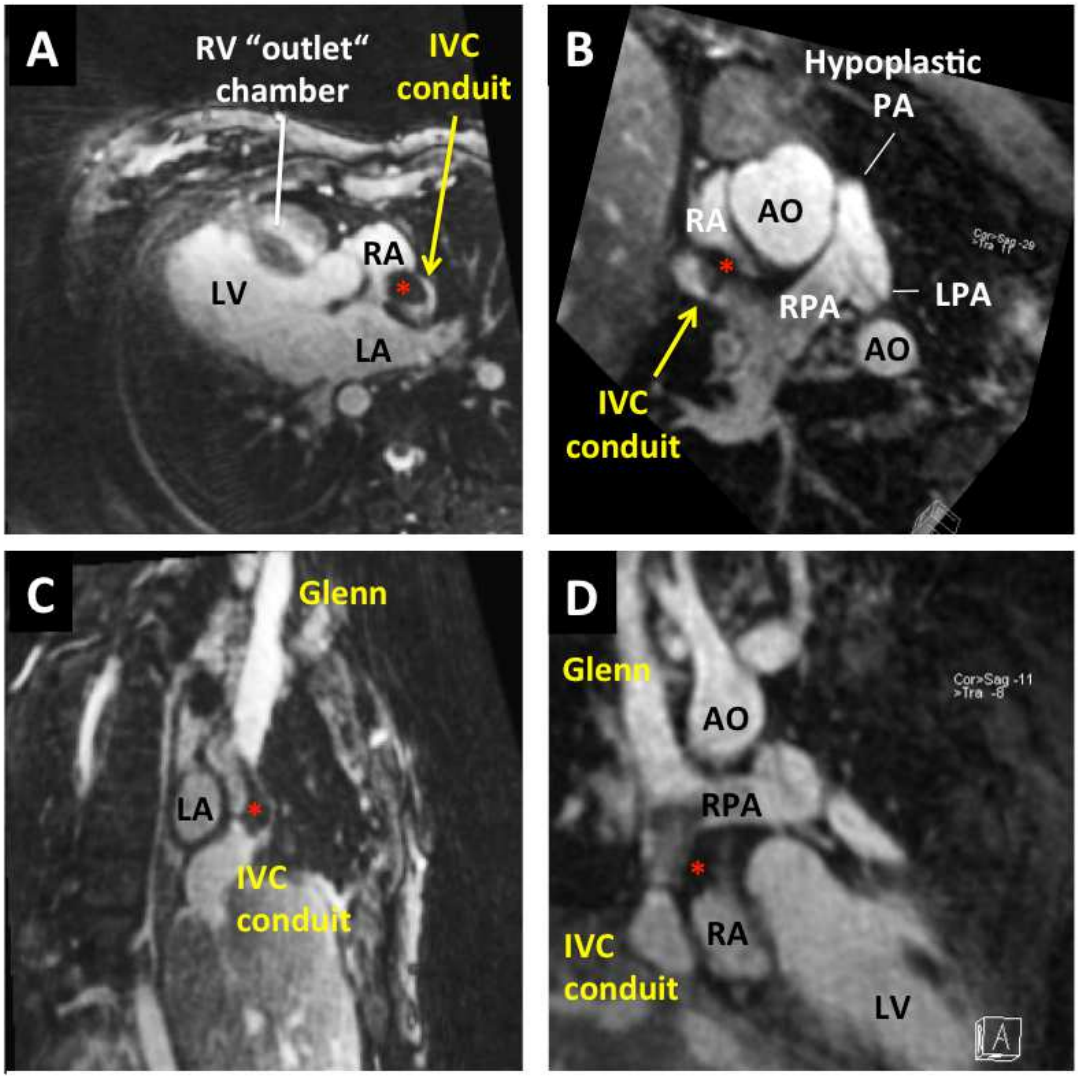

Figure 5.10: Example of tricuspid atresia with palliative Fontan circulation. The univentricle has a left ventricular morphology and a small right ventricular outlet chamber can be recognized (A). The IVC extracardiac conduit is seen behind the RA with a susceptibility artifact corresponding to the previous percutaneous closure of the fenestration (*). The main pulmonary artery is hypoplastic and the communication between the IVC extracardiac conduit and the right pulmonary artery (RPA) is wide (B). Figures (C) and (D) are oblique sagittal and coronal views centered on both venae cavae, showing non stenotic Fontan conduit and Glenn shunt to the RPA. These images are courtesy of Pierre Monney, MD and are published in [Monn 13].

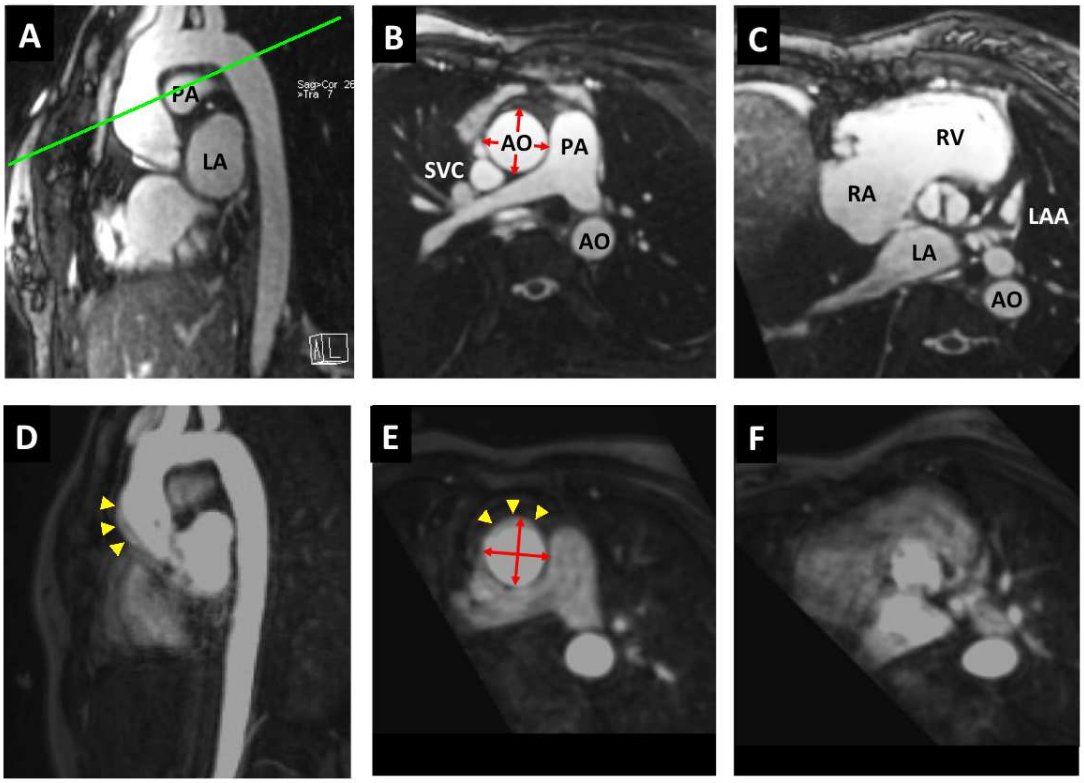

Figure 5.11: Bicuspid aortic valve with ascending aortic aneurysm: comparison between the self-navigated 3D whole-heart dataset (A-C) with a conventional 3D angiogram (D-F). The green line in (A) represents the position of the plane in (B), oriented perpendicular to the ascending aorta. Although the morphology of the aortic arch is well shown on both acquisitions, the turbulent and anteriorly directed ejection flow through the bicuspid aortic valve causes an artifact in the interior part of the ascending aorta in the conventional angiography (D, E - yellow arrowheads). The maximum diameter of the ascending aorta can be correctly measured on both acquisitions (B, E - red arrows). Imaging of the aortic root is affected by motion artifacts in the conventional angiogram and does not allow for any measurement (F). On the other hand, the ECG-gated self-navigated MR dataset offers a precise visualization of such region, including the morphology of the aortic valve, the left atrial appendage (LAA) and the proximal part of the left coronary system (C). These images are courtesy of Pierre Monney, MD and are published in [Monn 13].

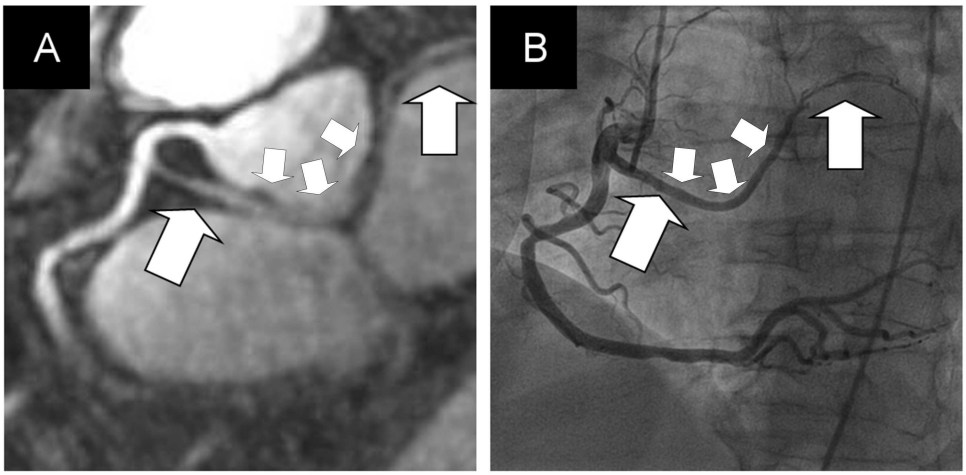

Figure 5.12: Example comparing multiplanar reformats of the whole-heart self-navigated coronary MRI datasets (A) with the correspondent X-ray coronary angiogram (B). A rare case of anomalous origin and course of the LCX from the proximal RCA is clearly depicted with exact correspondence between both imaging modalities (white arrows). While the anatomy of the coronary artery is well depicted in the MRA and perfectly corresponds to what can be observed in the X-ray, only the MRI dataset provides a clear understanding of the relationship of the LCX with the great vessels and surrounding cardiac anatomy. In this case the anomalous coronary had posterior course, between the aorta and the left ventricle, which corresponds to a benign congenital anomaly that does not need surgery. The X-ray images are courtesy of Christophe Sierro, MD.

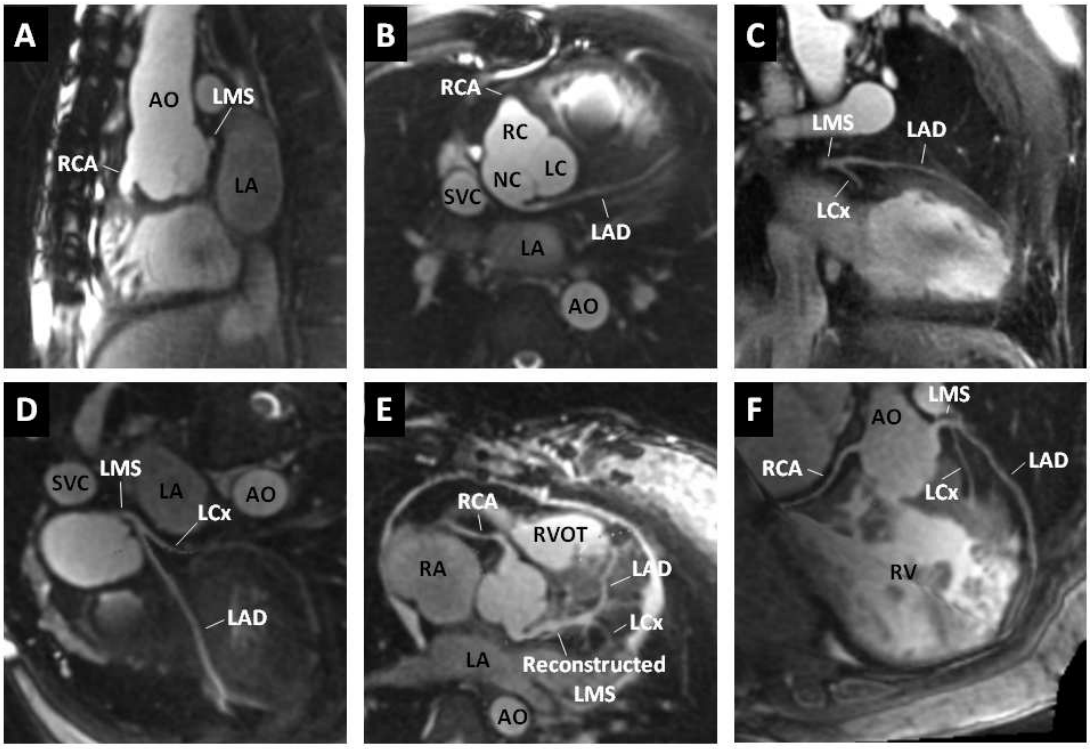

Figure 5.13: Examples of anomalous coronary arteries imaged with the self-navigated whole-heart sequence. Abnormal left coronary artery (LCA) arising from the non-coronary sinus and running between the aorta and the left atrium (A-C). Multiplanar reformat of abnormal LCA from the non-coronary sinus (D). Multiplanar reformat of a surgically reconstructed left main stem in a case of an abnormal left coronary artery arising from the pulmonary artery (ALCAPA) syndrome (E). Normal course of the coronary arteries in a case of transposition of the great arteries (TGA) (F). Aorta is connected to the morphological right ventricle. Legend - LMS: left main stem, LAD: left anterior descending artery, LCx: left circumflex artery, RCA: right coronary artery, NC: non-coronary cusp, RC: right coronary cusp, LC: left coronary cusp, LA: left atrium These images are courtesy of Pierre Monney, MD and are published in [Monn 13].

5.4 Discussion

In this work, the diagnostic performance of the self-navigated coronary MRA approach was tested in patients with suspected or known coronary artery disease. To the best of our knowledge, this has not been previously ascertained in the literature. Data acquisition was successful in all subjects, while the total scan time showed high correlation with that predicted using the heart rate of the subjects. The overall image quality was on average satisfactory and main and proximal coronary segments could be visualized significantly more often than mid and distal segments (in 92.3% vs. 84.0% and 55.8% of the cases, respectively). The subjective score and vessel sharpness were also significantly higher ($p < 0.05$) in the main and proximal segments with respect to their distal counterparts and anomalies of the coronary arteries could be always confirmed or excluded. The respiratory self-navigated sequence resulted in a per-vessel specificity that is comparable to the values reported in the literature for conventional navigator-gated coronary MRA (85%), while the sensitivity (64.7%) is lower. While changes in the respiratory pattern or diaphragmatic drift have been a reason for scan termination or inability to reconstruct an image in navigator-gated acquisitions in the past [Saku 05], this no longer applies for self-navigated coronary MRA. As the only determinant of acquisition duration is the heart rate of the patient, the scan duration is known a priori, which is most useful for protocol definition. Although self-navigation leads to highly predictable scan duration, data accepted for reconstruction originate from a large range of respiratory displacements. Hence, a change in orientation or shape of the heart between respiratory phases is more likely, but the current reconstruction algorithm does not account for these effects. For these reasons, an image reconstruction technique, which excludes image data acquired during outlier respiratory positions, may lead to an improvement in image quality.

While discussing the average grades for each coronary segment, obtained in this study, some important aspects should be considered. First, the grading performed by the two experts was completely blinded with respect to the specific patientsâĂŹ indications or medical condition. In other words, low grades for specific coronary segments were given regardless of the underlying reason for the suboptimal visualization (e.g. bad performance of the self-navigated sequence, presence of a stent, presence of disease, calcifications etc.). Secondly, the patient group was varied and representative of an unselected cohort of patients that may routinely be referred to cardiac MRI. All age, weight and size categories were included, no exclusion criteria (e.g. extrasystole or irregular breathing) were applied, and the acquisition was planned by several different operators with general training in cardiac MRI, but no special training on the use of the self-navigated sequence. Although image quality is on average satisfactory for the visualization of the proximal segments of the coronary tree, the method still needs to be improved to better visualize more distal parts. Residual, unsuppressed cardiac motion and residual three-dimensional respiratory displacement are likely causes of image quality degradation. In particular, we have only exploited respiratory motion correction in superior-inferior direction. However, it is has been documented [Mank 02] that this motion is more complex and individually dependent. Therefore, future developments should be directed toward 3D motion correction. As

the 3D radial k-space sampling scheme enables respiratory motion correction in any direction, an expansion to 3D motion correction seems straightforward and holds promise for improved image quality [Lai 09]. In parallel to shortcomings related to respiratory motion suppression, variable RR intervals and high heart rates are other common sources of image artifacts that affect self-navigation as much as the more conventional navigator approaches. Therefore, the utility of modern acceleration schemes [Prue 01, Gris 02, Lust 07] aimed at improving temporal resolution remain to be studied. Streaking artifacts due to radial undersampling are mainly caused by bright unsuppressed fat signal outside the FOV. An improved fat saturation strategy for radial sampling is therefore desirable. However, for radial approaches, fat saturation is more challenging as each signal-readout goes through the origin of k-space. Alternatively, spectral spatial pulses [Born 14] remain to be studied, but a prolonged TR may be expected. Finally, our study was conducted at 1.5T and without the administration of isosorbide dinitrate [Hu 10] or Îš-blockers.

The diagnostic accuracy of coronary MRA for the detection of CAD has been investigated in several single-center studies in recent years [Saku 06, Kim 01a, Dani 04, Jahn 05, Yang 09, Naga 11], resulting in sensitivity ranging from 73% to 97% and specificity ranging from 68% to 96%. In particular, the most recent multicenter trial [Kato 10] reported a per-vessel sensitivity and specificity of 83% and 90%, respectively. The current assessment of the performance of the self-navigated coronary MRA acquisition demonstrated a per-vessel specificity close to those previously reported, while the sensitivity is still suboptimal. However, in the majority of the above-mentioned studies, only patients who were scheduled to undergo or who had undergone an X-ray coronary angiogram for diagnostic purposes were selected for MRI. This leads to a certain selection bias that was not present in our study, since all 78 patients that were referred to cardiac MRI underwent a double blinded analysis of the MRA datasets for detection of CAD. A certain bias is intrinsically unavoidable on the subset of subjects used for the computation of sensitivity and specificity (as X-ray is performed only in cases of suspected or confirmed CAD). Nevertheless, only after unblinding it was possible to learn about the specific cardiac MR indications of each of the MRA patients and which of them did or did not have an X-ray coronary angiogram available for comparison. While both scanning time and spatial resolution are still inferior for coronary MRA with respect to CT angiography (CTA) [Hamd 11, Sche 10], the ease-of-use of the former has also been limited because of the need for meticulous scout scanning, navigator placement and uncertain scanning times. Respiratory self-navigation removes these barriers. Simultaneously, and as demonstrated, it can easily be integrated into a comprehensive cardiac exam that provides complementary information that may not as easily be obtained with contemporary CTA.

The high isotropic resolution of the datasets, in general, supports multi-planar offline reformatting in any plane orientation, which is particularly useful in CHD patients with complex anatomy. Image quality in young subjects was generally better than that in older patients, due to a more regular heart rate and respiratory pattern, and

possibly also to a smaller BMI and reduced fat signal.

The current study has limitations. As patients were not selected a priori for assessment of CAD in comparison with X-ray angiography, only a limited number of datasets, with respect to the total (31/78) could be used for calculation of sensitivity and specificity for detecting coronary artery stenoses. The evaluation of the self-navigated coronary MRA technique on a pre-selected patient cohort has to be considered for future studies. Although image quality measures (e.g. vessel sharpness) were reported, the self-navigated sequence was not directly compared to standard navigator-gated coronary MRA techniques. However, this has been reported in Chapter 4 a small volunteer study. Nevertheless, a direct comparison between these techniques in CAD patients will be of high interest.

5.5 Conclusion

In summary, the results of this study demonstrate for the first time to our knowledge, that respiratory self-navigated whole-heart coronary MR imaging is feasible in a patient setting. It can easily be accommodated after contrast administration and is already useful for the identification of anomalous coronary arteries. Specificity for CAD detection in proximal branches is promising, while sensitivity still needs to be improved.

Chapter 6

Summary

In this work, a new acquisition and motion correction strategy for free-breathing self-navigated whole-heart coronary magnetic resonance angiography was introduced, described, implemented, and tested in volunteers as well as in a first patient study in an advanced clinical setting. This technique implements a practical solution for performing whole-heart coronary MR imaging through a simple and straightforward acquisition procedure and tries to address the main drawbacks of the current state of the art navigator-gated technologies, i.e. anisotropic spatial resolution, compensation of respiratory motion, robustness, time efficiency and ease of use.

The clinical importance of coronary imaging is introduced at the beginning of Chapter 1, supported by statistical data from the literature. All the problems connected to the high resolution needed to characterize the complex anatomy of the coronary tree and to the constant motion that challenges the current technology used for clinical imaging are listed and described. The clinical needs for a radiation-free acquisition and a motion corrected reconstruction for coronary MRA are discussed within this chapter and the motivations for the current thesis work are listed.

Chapter 2 gives an overview on the basics of MRI, starting from the behaviour of a single spin in a magnetic field to the currently implemented solutions for spatial encoding of the MR signal. Different existing acquisition schemes are described and compared, and some of the most common MRI artifacts are theoretically explained and shown with example images. The description moves then to the specific field of coronary MR angiography. In synthesis, as coronary MRA is usually ECG-triggered to avoid image artifacts due to the periodic contraction and relaxation of the heart, image data are typically acquired segmented (or interleaved) over a large number of heartbeats and during a short time window in the cardiac cycle. As the number of heartbeats needed does not allow for single breath-hold acquisitions, the coronary MRA scan is usually performed in free-breathing and respiratory motion needs to be take into account. At the end of Chapter 2, an overview on the current state of the art for respiration management in coronary MRA is given, and the basic differences between respiratory navigator gated approaches and self-navigation are clarified for the first time.

The proposed acquisition method consists of a novel interleaved 3D radial trajectory, mathematically constructed on a spiral phyllotaxis pattern. This pattern intrinsically minimizes the eddy currents artifacts of the interleaved radial bSSFP acquisition, while ensuring a complete and uniform coverage of k-space (Chapter 3). The 3D radial sampling scheme allows for isotropic imaging with high undersampling ratios, without requiring neither a complex planning effort nor particular expertise of the user in the field of coronary MR imaging as e.g. foldover artifacts are automatically avoided. The spiral phyllotaxis pattern, here applied to 3D radial imaging, was tested in comparison with two variants of the more widely used Archimedean spiral pattern, already published in coronary MRA literature. Uniformity of k-space coverage, potential eddy currents, point spread function and final image quality were analysed and compared in phantoms and in vivo. The uniformity of the proposed sampling scheme showed to be comparable to that of the former and most uniform variant of the Archimedean spiral using the measure of the relative standard deviation of the distance between the starting points of all adjacent readouts on the surface of the sphere encompassing the acquired k-space. The average angular distance between successively acquired readouts showed to be highly reduced, similarly to the latter variant, with minimized eddy currents. Finally, the point spread function obtained with the 3D radial trajectory constructed on a phyllotaxis pattern, demonstrated a higher robustness against aliasing energy, and, hence, aliasing artifacts, when the imaged object extends outside the imaged FOV, i.e. in any in vivo situation. All these differences are reflected in the final image quality. Compared with a reference data set, which was acquired with a non-interleaved version of the most uniform variant of the Archimedean spiral pattern, phantom images were degraded by eddy current effects when data acquisition was performed with the same Archimedean pattern, in an interleaved fashion. The image quality was almost completely restored in case of the segmented spiral phyllotaxis pattern, which enables both uniform sampling and minimal eddy current effects. Quantitative endpoints in vivo, such as SNR, CNR and vessel sharpness of the coronary arteries were found to be higher when compared to those obtained with the interleaved Archimedean spiral pattern in conventional navigator-gated acquisitions. In particular, the SNR improved by 52%, using the interleaved spiral phyllotaxis pattern, while CNR improved by 67%, and vessel sharpness by about 16%.

While the robustness to motion of the 3D radial trajectory helps reducing the artifacts due to uncompensated cardiac motion (e.g. imperfect ECG gating), the specific spatial arrangements of the radial readout makes this trajectory ideal for intrinsic correction of the respiratory motion, i.e. self-navigation. The integration of the self-navigation module is obtained with the acquisition of an additional readout, oriented in superior-inferior direction (where the main displacement of the heart due to respiration occurs) at the beginning of each interleave (heartbeat) of the segmented acquisition. This modification can be implemented without any further adaptation of the sampling scheme, while preserving the robustness towards eddy currents that characterizes the proposed sampling scheme. In Chapter 4 a novel technique for respiratory motion detection on the 1D FFT of such SI readouts (also referred to as SI projections) was described. First, the bright signal of the blood pool created by

the bSSFP acquisition is isolated from the surrounding structures using an optimized combination of the output signals from the standard phased-array surface receiver coil, placed on the chest. A novel algorithm for automatic 1D segmentation of the bright pool along the SI projections was proposed and described in detail. Motion detection of the segmented portion of the SI projections is then performed using a cross correlation technique. The final result was proven to outperform the simple motion detection without the proposed coil combination technique and/or without the segmentation of the pool. Respiratory motion detection and correction performed directly on the readouts acquired for imaging eliminate the need of hemidiaphragmatic navigators, improve the accuracy of the correction, and allow for full 100% scan efficiency. In vivo comparison of the proposed self-navigated acquisition with the state of the art navigator-gating was performed in 10 healthy volunteers. Image quality, average vessel length, and vessel sharpness were equivalent or improved using the described technique. In particular vessel sharpness of the RCA, LAD and LCX, respectively was improved by 9%, 7%, and 2%. The increase vessel sharpness in the RCA was found to be statistically significant ($p < 0.05$). Using the proposed self-navigation methodology, the average total scanning time was significantly reduced by more than 60% with respect to the navigator-gated acquisitions ($p < 0.01$).

The proposed self-navigated whole-heart acquisition, not only requires minimal expertise for the planning of the examination, but allows also for a priori knowledge of the duration of the coronary MRI examination. For this reason, the proposed self-navigated coronary MRA acquisition could be integrated, as an optional component, in routine clinical cardiac MRI examinations, for extensive testing in patients. Since the performance of self-navigation hinges on myocardium-blood contrast, and provided that there is often a wait time between perfusion imaging and late gadolinium enhancement imaging in routine clinical protocols, high-resolution self-navigated 3D whole-heart imaging was performed within such wait time as an optional scan to obtain information on both the general cardiac anatomy and the coronary tree. Written informed consent was obtained from all participants and the study was approved by the Institutional Review Board. Self-navigated coronary MRA was performed after administration of contrast agent in 78 patients (mean age, 48.5 ± 20.7 years; 53 male) referred for cardiac MRI for CAD (n=40), cardiomyopathies (n=14), congenital anomalies (n=17), and others (n=7). The actual scan duration was recorded and compared to the predicted duration, calculated prior to the scan, using the heart rates of the patients. Image quality as well as the performance of the novel technique were assessed by experts in the fields of cardiac MR and cardiology. Quality score, vessel sharpness, length and diameter for each segment of the coronary tree were measured. Quantitative values of proximal, mid, and distal segments were compared using ANOVA and t-tests. A double-blinded comparison with x-ray angiography was performed where available and the diagnostic performance of this novel technique for the detection of coronary artery stenoses was evaluated. This technique was also tested for visualization of congenital malformations of the cardiac anatomy as well as of malformations of the coronary arteries in patients with suspected coronary arterial anomalies by assessing the origin, anatomy, and relationship of the proximal coronary arteries with the great vessels. Whole-heart datasets with 1.15 mm isotropic spatial

resolution were acquired in an average of 7.38 ± 1.85 min, with a very high correlation with the predicted scan time. Main and proximal coronary segments could be visualized in 92.3% of the cases, while mid and distal segments in 84.0% and 55.8%, respectively. The subjective score and vessel sharpness were significantly higher in the proximal segments (1.7 ± 1.0) with respect to their mid and distal counterparts (1.4 ± 1.0 and 0.7 ± 0.8, respectively, with $p<0.05$). Anomalous cardiac anatomy, origin and course of anomalous coronary arteries could be very well visualized in all congenital cases. Sensitivity and specificity for stenosis detection per vessel were 64.7% and 85.0% in 31 patients for whom the gold standard X-ray coronary angiography was available. Although this first clinical study was performed in a limited number of patients, the ease-of-use and the a priori knowledge of the scan duration associated to the self-navigated sequence makes it ideally suited for future testing in large patient populations or even multicenter trials.

Chapter 7

Outlook

As the average life span of the world population increases, cardiovascular diseases (CVDs) firmly establish themselves as the most frequent cause of death in many of the most developed countries. Coronary artery disease (Chapter 1) represents alone more than 50% of the total CVDs [Roge 11], and there is a strong need for a non-invasive test that could be adopted reliably for the assessment of CAD without the use of ionizing radiation. Coronary MR angiography has been developed now for almost 20 years, and has a long history of considerable technical advances [Stub 07]. However, despite high initial expectations, such technique is still not considered for clinical assessment of CAD. A document on "appropriate" indications for cardiac CT and MR imaging [Hend 06], describes coronary CT as a recommended imaging method for exclusion of significant CAD in patients with chest pain symptoms and intermediate pretest probability of CAD. In contrast, coronary MR angiography is categorized as an "inappropriate" method for excluding significant CAD in the same subject group. It is stated that coronary CT angiography is still superior to coronary MR angiography in terms of spatial resolution and study success rate. It appears clear how the expertise of the user, as well as the accurate planning of the MR scan and its total duration, have so far played a fundamental role on the final image quality of a navigator-gated coronary MR acquisition [Saku 11] and its applicability in clinical routine. Although the technique presented in this thesis represents a considerable step towards the integration of a whole-heart acquisition with high isotropic resolution for the assessment of the coronary arteries in clinical routine, an extensive amount of work needs still to be done. From a technical point of view improvements towards a more complex and subject dependent respiratory motion correction are highly desirable. Iterative reconstruction methods can be used to advance in this direction. The possibility to perform the coronary MR acquisition at higher field streghts (3T) will enable a higher SNR and, thus, current restrictions on T2 preparation, fat saturation and off-resonance artifacts need to be addressed. In addition, shorter acquisition times will become possible with the integration of the most recent advances in parallel imaging and compressed sensing, which are nowadays advancing at a very high pace. If the acquisition time is not only known a priori, but also minimized, a more comfortable examination for the patient will become an option. However, technical improvements will not be sufficient as long as an extensive validation of the methodology on a multicenter level for the detection of CAD is not

performed. Although the patient study described here was performed in a limited number of patients, the ease-of-use and the a priori knowledge of the scan duration associated to the self-navigated sequence makes it ideally suited for future testing in larger patient populations or even multicenter trials. Finally, the full potential and range of possible applications of the self-navigated technique remain to be explored. The possibility of performing a 3D whole-heart acquisition with real high isotropic resolution in free-breathing and in a fixed amount of time enabled by such technique can be exploited to answer also other important clinical questions. High resolution 3D LGE can be highly appealing to display both the coronary anatomy and the structure and position of the scar tissue in one single dataset e.g. for planning ablation in re-synchronization procedures [Picc 13b]. In combination with an adiabatic T2-preparation pulse [Neza 09], a full 3D quantitative T2-map of the myocardium can be obtained [Hees 13]. If the 3D radial self-navigated sequence is acquired continuously without ECG-triggering, phase-specific cardiac volumes can be reformatted to enhance the sharpness of the coronaries in different cardiac phases and, eventually, a real 3D cine dataset can be obtained [Copp 13a].

List of Figures

List of Tables

Bibliography

[Abra 64] M. Abramowitz and I. A. Stegun. *Handbook of Mathematical Functions: With Formulars, Graphs, and Mathematical Tables*. Vol. 55, DoverPublications. com, USA, Jun 1964.

[Aust 75] W. G. Austen, J. E. Edwards, R. L. Frye, G. G. Gensini, V. L. Gott, L. S. Griffith, D. C. McGoon, M. L. Murphy, and B. B. Roe. "A reporting system on patients evaluated for coronary artery disease. Report of the Ad Hoc Committee for Grading of Coronary Artery Disease, Council on Cardiovascular Surgery, American Heart Association". *Circulation*, Vol. 51, No. 4 Suppl, pp. 5–40, Apr 1975.

[Barg 02] A. V. Barger, W. F. Block, Y. Toropov, T. M. Grist, and C. A. Mistretta. "Time-resolved contrast-enhanced imaging with isotropic resolution and broad coverage using an undersampled 3D projection trajectory". *Magn Reson Med*, Vol. 48, No. 2, pp. 297–305, Aug 2002.

[Bern 04] M. Bernstein, K. King, and X. Zhou. *Handbook of MRI pulse sequences*. Elsevier Academic Press, Burlington, MA, USA, Jun 2004.

[Bhat 11] H. Bhat, L. Ge, S. Nielles-Vallespin, S. Zuehlsdorff, and D. Li. "3D radial sampling and 3D affine transform-based respiratory motion correction technique for free-breathing whole-heart coronary MRA with 100% imaging efficiency". *Magn Reson Med*, Vol. 65, No. 5, pp. 1269–1277, May 2011.

[Bi 05] X. Bi, V. Deshpande, O. Simonetti, G. Laub, and D. Li. "Three-dimensional breathhold SSFP coronary MRA: a comparison between 1.5T and 3.0T". *J Magn Reson Imaging*, Vol. 22, No. 2, pp. 206–212, Aug 2005.

[Bier 05] O. Bieri, M. Markl, and K. Scheffler. "Analysis and compensation of eddy currents in balanced SSFP". *Magn Reson Med*, Vol. 54, No. 1, pp. 129–137, Jul 2005.

[Bloc 46] F. Bloch. "Nuclear induction". *Phys. Rev.*, Vol. 70, No. 7-8, pp. 460–474, Oct 1946.

[Bogr 77] H. G. Bogren, B. M. Lantz, R. R. Miller, and D. T. Mason. "Effect of respiration on cardiac motion determined by cineangiography. Implications concerning three-dimensional heart reconstruction using computer tomography". *Acta Radiol Diagn (Stockh)*, Vol. 18, No. 6, pp. 609–620, Nov 1977.

[Born 14] P. Börnert, P. Koken, K. Nehrke, H. Eggers, and P. Ostendorf. "Water/fat-resolved whole-heart Dixon coronary MRA: An initial comparison". *Magn Reson Med*, Vol. 71, No. 1, pp. 156–163, Jan 2014.

[Born 95] P. Börnert and D. Jensen. "Coronary artery imaging at 0.5 T using segmented 3D echo planar imaging". *Magn Reson Med*, Vol. 34, No. 6, pp. 779–785, Dec 1995.

[Botn 99] R. M. Botnar, M. Stuber, P. G. Danias, K. V. Kissinger, and W. J. Manning. "Improved coronary artery definition with T2-weighted, free-breathing, three-dimensional coronary MRA". *Circulation*, Vol. 99, No. 24, pp. 3139–3148, Jun 1999.

[Brit 95] J. H. Brittain, B. S. Hu, G. A. Wright, C. H. Meyer, A. Macovski, and D. G. Nishimura. "Coronary angiography with magnetization-prepared T2 contrast". *Magn Reson Med*, Vol. 33, No. 5, pp. 689–696, May 1995.

[Bush 11] J. T. Bushberg and J. M. Boone. *The essential physics of medical imaging*. Lippincott Williams & Wilkins, Philadelphia, PA, USA, Oct 2011.

[Chan 09] R. W. Chan, E. A. Ramsay, C. H. Cunningham, and D. B. Plewes. "Temporal stability of adaptive 3D radial MRI using multidimensional golden means". *Magn Reson Med*, Vol. 61, No. 2, pp. 354–363, Feb 2009.

[Clin 99] H. Cline and T. Anthony. "Uniform k-space sampling with an interleaved Fibonacci spiral acquisition". In: *Proceedings of the 7th Annual Meeting of ISMRM*, p. 1657, Philadelphia, PA, USA, May 1999.

[Cool 65] J. W. Cooley and J. W. Tukey. "An algorithm for the machine calculation of complex Fourier series". *Mathematics of computation*, Vol. 19, No. 90, pp. 297–301, Apr 1965.

[Copp 13a] S. Coppo, D. Piccini, J. Chaptinel, G. Bonanno, and M. Stuber. "Non-ECG triggered, slef-navigated 3D whole-heart MRI with golden angle for multiphase coronary imaging". In: *Proceedings of the 21th Annual Meeting of ISMRM*, p. 1417, Salt Lake City, Utah, USA, Apr 2013.

[Copp 13b] S. Coppo, D. Piccini, G. Vincenti, D. Locca, S. J., P. Tozzi, and M. Stuber. "A first report on self-navigated isotropic whole-heart MRI for the visualization of coronary artey bypass grafts". In: *Proceedings of the 21th Annual Meeting of ISMRM*, p. 1315, Salt Lake City, Utah, USA, Apr 2013.

[Dama 71] R. Damadian. "Tumor detection by nuclear magnetic resonance". *Science*, Vol. 171, No. 3976, pp. 1151–1153, Mar 1971.

[Dani 04] P. G. Danias, A. Roussakis, and J. P. A. Ioannidis. "Diagnostic performance of coronary magnetic resonance angiography as compared against conventional X-ray angiography: a meta-analysis". *J Am Coll Cardiol*, Vol. 44, No. 9, pp. 1867–1876, Nov 2004.

[Dani 97] P. G. Danias, M. V. McConnell, V. C. Khasgiwala, M. L. Chuang, R. R. Edelman, and W. J. Manning. "Prospective navigator correction of image position for coronary MR angiography". *Radiology*, Vol. 203, No. 3, pp. 733–736, Jun 1997.

[Desa 03] A. S. Desai, D. H. Solomon, P. H. Stone, and J. Avorn. "Economic consequences of routine coronary angiography in low- and intermediate-risk patients with unstable angina pectoris". *Am. J. Cardiol.*, Vol. 92, No. 4, pp. 363–367, Aug 2003.

[Desh 03] V. S. Deshpande, S. M. Shea, and D. Li. "Artifact reduction in true-FISP imaging of the coronary arteries by adjusting imaging frequency". *Magn Reson Med*, Vol. 49, No. 5, pp. 803–809, May 2003.

[Desh 06] V. S. Deshpande, M. S. krishnam, S. G. Ruehm, J. P. Finn, and G. A. Laub. "Non-contrast MR angiography of the heart and great vvessel using SSFP with non-selective excitation". In: *Proceedings of the 14th Annual Meeting of ISMRM*, p. 383, Seattle, Washington, USA, May 2006.

[Dira 47] P. A. M. Dirac. *The principles of quantum mechanics.* Vol. 1, Oxford at the Clarendon Press, 1947.

[Diss 02] W. Dissmann and M. de Ridder. "The soft science of German cardiology". *Lancet*, Vol. 359, No. 9322, pp. 2027–2029, Jun 2002.

[Dodg 92] J. Dodge, B. G. Brown, E. L. Bolson, and H. T. Dodge. "Lumen diameter of normal human coronary arteries. Influence of age, sex, anatomic variation, and left ventricular hypertrophy or dilation". *Circulation*, Vol. 86, No. 1, pp. 232–246, Jan 1992.

[Done 08] M. Doneva, H. Eggers, J. Rahmer, P. Börnert, and A. Mertins. "Highly undersampled 3D golden ratio radial imaging with iterative reconstruction". In: *Proceedings of the 16th Annual Meeting of ISMRM*, p. 336, Toronto, Canada, May 2008.

[Doua 96] S. Douady and Y. Couder. "Phyllotaxis as a dynamical self organizing process part I: the spiral modes resulting from time-periodic iterations". *Journal of theoretical biology*, Vol. 178, No. 3, pp. 255–273, Feb 1996.

[Duer 98] J. L. Duerk, J. S. Lewin, M. Wendt, and C. Petersilge. "Remember true FISP? A high SNR, near 1-second imaging method for T2-like contrast in interventional MRI at .2 T". *J Magn Reson Imaging*, Vol. 8, No. 1, pp. 203–208, Jan 1998.

[Ehma 89] R. L. Ehman and J. P. Felmlee. "Adaptive technique for high-definition MR imaging of moving structures". *Radiology*, Vol. 173, No. 1, pp. 255–263, Oct 1989.

[Erns 66] R. Ernst and W. Anderson. "Application of Fourier transform spectroscopy to magnetic resonance". *Rev. Sci. Instrum.*, Vol. 37, No. 1, pp. 93–102, Jan 1966.

[Etie 02] A. Etienne, R. M. Botnar, A. M. C. Van Muiswinkel, P. Boesiger, W. J. Manning, and M. Stuber. "'Soap-Bubble' visualization and quantitative analysis of 3D coronary magnetic resonance angiograms". *Magn Reson Med*, Vol. 48, No. 4, pp. 658–666, Oct 2002.

[Faya 02] Z. A. Fayad, V. Fuster, K. Nikolaou, and C. Becker. "Computed tomography and magnetic resonance imaging for noninvasive coronary angiography and plaque imaging current and potential future concepts". *Circulation*, Vol. 106, No. 15, pp. 2026–2034, Jan 2002.

[Fowl 92] D. R. Fowler, P. Prusinkiewicz, and J. Battjes. "A collision-based model of spiral phyllotaxis". In: *ACM SIGGRAPH Computer Graphics*, pp. 361–368, ACM, 1992.

[Gray 18] H. Gray. *Anatomy of the human body.* Lea & Febiger, Philadelphia, 1918.

[Gris 02] M. A. Griswold, P. M. Jakob, R. M. Heidemann, M. Nittka, V. Jellus, J. Wang, B. Kiefer, and A. Haase. "Generalized autocalibrating partially parallel acquisitions (GRAPPA)". *Magn Reson Med*, Vol. 47, No. 6, pp. 1202–1210, Jun 2002.

[Haac 86] E. M. Haacke and J. L. Patrick. "Reducing motion artifacts in two-dimensional Fourier transform imaging". *Magn Reson Imaging*, Vol. 4, No. 4, pp. 359–376, May 1986.

[Haac 99] E. M. Haacke, R. W. Brown, M. R. Thompson, and R. Venkatesan. *Magnetic resonance imaging: physical principles and sequence design.* Vol. 1, Wiley-Liss New York, 1999.

[Haas 86] A. Haase, J. Frahm, D. Matthaei, W. Hanicke, and K.-D. Merboldt. "FLASH imaging. Rapid NMR imaging using low flip-angle pulses". *J. Magn. Reson.*, Vol. 67, No. 2, pp. 258–266, Apr 1986.

[Hahn 50] E. L. Hahn. "Spin echoes". *Phys. Rev.*, Vol. 80, No. 4, p. 580, 1950.

[Hamd 11] A. Hamdan, P. Asbach, E. Wellnhofer, C. Klein, R. Gebker, S. Kelle, H. Kilian, A. Huppertz, and E. Fleck. "A prospective study for comparison of MR and CT imaging for detection of coronary artery stenosis". *JACC Cardiovasc Imaging*, Vol. 4, No. 1, pp. 50–61, Jan 2011.

[Haus 08] T. H. Hauser and W. J. Manning. "The promise of whole-heart coronary MRI". *Curr Cardiol Rep*, Vol. 10, No. 1, pp. 46–50, Feb 2008.

[Hees 13] R. B. van Heeswijk, D. Piccini, H. Feliciano, S. J., and M. Stuber. "Self-navigated three-dimensional cardiac T2 mapping at 3T". In: *Proceedings of the 21th Annual Meeting of ISMRM*, p. 4565, Salt Lake City, Utah, USA, Apr 2013.

[Hend 06] R. C. Hendel, M. R. Patel, C. M. Kramer, M. Poon, R. C. Hendel, J. C. Carr, N. A. Gerstad, L. D. Gillam, J. M. Hodgson, R. J. Kim, C. M. Kramer, J. R. Lesser, E. T. Martin, J. V. Messer, R. F. Redberg, G. D. Rubin, J. S. Rumsfeld, A. J. Taylor, W. G. Weigold, P. K. Woodard, R. G. Brindis, R. C. Hendel, P. S. Douglas, E. D. Peterson, M. J. Wolk, J. M. Allen, M. R. Patel, A. C. of Cardiology Foundation Quality Strategic Directions Committee Appropriateness Criteria Working Group, A. C. of Radiology, S. of Cardiovascular Computed Tomography, S. for Cardiovascular Magnetic Resonance, A. S. of Nuclear Cardiology, N. A. S. for Cardiac Imaging, S. for Cardiovascular Angiography, Interventions, and S. of Interventional Radiology. "ACCF/ACR/SCCT/SCMR/ASNC/NASCI/SCAI/SIR 2006 appropriateness criteria for cardiac computed tomography and cardiac magnetic resonance imaging: a report of the American College of Cardiology Foundation Quality Strategic Directions Committee Appropriateness Criteria Working Group, American College of Radiology, Society of Cardiovascular Computed Tomography, Society for Cardiovascular Magnetic Resonance, American Society of Nuclear Cardiology, North American Society for Cardiac Imaging, Society for Cardiovascular Angiography and Interventions, and Society of Interventional Radiology.". *J Am Coll Cardiol*, Vol. 48, No. 7, pp. 1475–1497, Oct 2006.

[Hoff 05] M. H. K. Hoffmann, H. Shi, B. L. Schmitz, F. T. Schmid, M. Lieberknecht, R. Schulze, B. Ludwig, U. Kroschel, N. Jahnke, W. Haerer, H.-J. Brambs, and A. J. Aschoff. "Noninvasive coronary angiography with multislice

computed tomography". *JAMA*, Vol. 293, No. 20, pp. 2471–2478, May 2005.

[Hofm 99] M. B. Hofman, R. E. Henson, S. J. Kovacs, S. E. Fischer, R. B. Lauffer, K. Adzamli, J. De Becker, S. A. Wickline, and C. H. Lorenz. "Blood pool agent strongly improves 3D magnetic resonance coronary angiography using an inversion pre-pulse". *Magn Reson Med*, Vol. 41, No. 2, pp. 360–367, Feb 1999.

[Hoge 97] R. D. Hoge, R. K. Kwan, and G. B. Pike. "Density compensation functions for spiral MRI". *Magn Reson Med*, Vol. 38, No. 1, pp. 117–128, Jul 1997.

[Hu 10] P. Hu, M. L. Chuang, L. H. Ngo, C. T. Stoeck, D. C. Peters, K. V. Kissinger, B. Goddu, L. A. Goepfert, W. J. Manning, and R. Nezafat. "Coronary MR imaging: effect of timing and dose of isosorbide dinitrate administration". *Radiology*, Vol. 254, No. 2, pp. 401–409, Feb 2010.

[Hube 03] M. E. Huber, I. Paetsch, B. Schnackenburg, A. Bornstedt, E. Nagel, E. Fleck, P. Boesiger, F. Maggioni, F. M. Cavagna, and M. Stuber. "Performance of a new gadolinium-based intravascular contrast agent in free-breathing inversion-recovery 3D coronary MRA". *Magn Reson Med*, Vol. 49, No. 1, pp. 115–121, Jan 2003.

[Jack 91] J. I. Jackson, C. H. Meyer, D. G. Nishimura, and A. Macovski. "Selection of a convolution function for Fourier inversion using gridding [computerised tomography application]". *IEEE Transactions on Medical Imaging*, Vol. 10, No. 3, pp. 473–478, Sep 1991.

[Jahn 05] C. Jahnke, I. Paetsch, K. Nehrke, B. Schnackenburg, R. Gebker, E. Fleck, and E. Nagel. "Rapid and complete coronary arterial tree visualization with magnetic resonance imaging: feasibility and diagnostic performance". *Eur Heart J*, Vol. 26, No. 21, pp. 2313–2319, Nov 2005.

[Jahn 07] C. Jahnke, K. Nehrke, I. Paetsch, B. Schnackenburg, R. Gebker, E. Fleck, and E. Nagel. "Improved bulk myocardial motion suppression for navigator-gated coronary magnetic resonance imaging". *J Magn Reson Imaging*, Vol. 26, No. 3, pp. 780–786, Sep 2007.

[Jhoo 10] P. Jhooti, J. Keegan, and D. N. Firmin. "A fully automatic and highly efficient navigator gating technique for high-resolution free-breathing acquisitions: Continuously adaptive windowing strategy". *Magn Reson Med*, Vol. 64, No. 4, pp. 1015–1026, Oct 2010.

[Kato 10] S. Kato, K. Kitagawa, N. Ishida, M. Ishida, M. Nagata, Y. Ichikawa, K. Katahira, Y. Matsumoto, K. Seo, R. Ochiai, Y. Kobayashi, and H. Sakuma. "Assessment of coronary artery disease using magnetic resonance coronary angiography: a national multicenter trial". *J Am Coll Cardiol*, Vol. 56, No. 12, pp. 983–991, Sep 2010.

[Kats 06] U. Katscher and P. Börnert. "Parallel RF transmission in MRI". *NMR Biomed*, Vol. 19, No. 3, pp. 393–400, May 2006.

[Kell 08] S. Kelle, R. G. Weiss, and M. Stuber. "Coronary magnetic resonance imaging". *Curr Pharm Des*, Vol. 14, No. 18, pp. 1778–1786, Jun 2008.

[Kim 01a] W. Y. Kim, P. G. Danias, M. Stuber, S. D. Flamm, S. Plein, E. Nagel, S. E. Langerak, O. M. Weber, E. M. Pedersen, M. Schmidt, R. M. Botnar, and W. J. Manning. "Coronary magnetic resonance angiography for the

detection of coronary stenoses". *N Engl J Med*, Vol. 345, No. 26, pp. 1863–1869, Dec 2001.

[Kim 01b] W. Y. Kim, M. Stuber, K. V. Kissinger, N. T. Andersen, W. J. Manning, and R. M. Botnar. "Impact of bulk cardiac motion on right coronary MR angiography and vessel wall imaging". *J Magn Reson Imaging*, Vol. 14, No. 4, pp. 383–390, Oct 2001.

[Klei 06] R. A. Kleinerman. "Cancer risks following diagnostic and therapeutic radiation exposure in children". *Pediatr Radiol*, Vol. 36 Suppl 2, pp. 121–125, Sep 2006.

[Lai 08] P. Lai, A. C. Larson, X. Bi, R. Jerecic, and D. Li. "A dual-projection respiratory self-gating technique for whole-heart coronary MRA". *J Magn Reson Imaging*, Vol. 28, No. 3, pp. 612–620, Sep 2008.

[Lai 09] P. Lai, X. Bi, R. Jerecic, and D. Li. "A respiratory self-gating technique with 3D-translation compensation for free-breathing whole-heart coronary MRA". *Magn Reson Med*, Vol. 62, No. 3, pp. 731–738, Sep 2009.

[Laut 73] P. C. Lauterbur. "Image formation by induced local interactions: examples employing nuclear magnetic resonance". *Nature*, Vol. 242, No. 5394, pp. 190–191, Mar 1973.

[Lauz 93] M. L. Lauzon and B. K. Rutt. "Generalized K-space analysis and correction of motion effects in MR imaging". *Magn Reson Med*, Vol. 30, No. 4, pp. 438–446, Oct 1993.

[Lauz 96] M. L. Lauzon and B. K. Rutt. "Effects of polar sampling in k-space". *Magn Reson Med*, Vol. 36, No. 6, pp. 940–949, Dec 1996.

[Lauz 98] M. L. Lauzon and B. K. Rutt. "Polar sampling in k-space: reconstruction effects". *Magn Reson Med*, Vol. 40, No. 5, pp. 769–782, Nov 1998.

[Lee 88] J. Lee Rodgers and W. A. Nicewander. "Thirteen ways to look at the correlation coefficient". *The American Statistician*, Vol. 42, No. 1, pp. 59–66, Feb 1988.

[Li 01] D. Li, J. C. Carr, S. M. Shea, J. Zheng, V. S. Deshpande, P. A. Wielopolski, and J. P. Finn. "Coronary arteries: magnetization-prepared contrast-enhanced three-dimensional volume-targeted breath-hold MR angiography". *Radiology*, Vol. 219, No. 1, pp. 270–277, Apr 2001.

[Li 09] C.-R. Li, A.-L. Ji, L. Gao, and Z.-X. Cao. "Stressed triangular tessellations and fibonacci parastichous spirals on Ag core/SiO2 shell microstructures". *Advanced Materials*, Vol. 21, No. 45, pp. 4652–4657, Dec 2009.

[Li 93] D. Li, C. B. Paschal, E. M. Haacke, and L. P. Adler. "Coronary arteries: three-dimensional MR imaging with fat saturation and magnetization transfer contrast". *Radiology*, Vol. 187, No. 2, pp. 401–406, May 1993.

[Li 98] D. Li, R. P. Dolan, R. C. Walovitch, and R. B. Lauffer. "Three-dimensional MRI of coronary arteries using an intravascular contrast agent". *Magn Reson Med*, Vol. 39, No. 6, pp. 1014–1018, Jun 1998.

[Lieb 84] J. M. Lieberman, R. E. Botti, and A. D. Nelson. "Magnetic resonance imaging of the heart". *Radiol Clin North Am*, Vol. 22, No. 4, pp. 847–858, Dec 1984.

[Lu 08] W. Lu and B. A. Hargreaves. "Multiresolution field map estimation using golden section search for water-fat separation". *Magn Reson Med*, Vol. 60, No. 1, pp. 236–244, Jul 2008.

[Lust 07] M. Lustig, D. Donoho, and J. M. Pauly. "Sparse MRI: The application of compressed sensing for rapid MR imaging". *Magn Reson Med*, Vol. 58, No. 6, pp. 1182–1195, Dec 2007.

[Mank 02] D. Manke, K. Nehrke, P. Börnert, P. Rösch, and O. Dössel. "Respiratory motion in coronary magnetic resonance angiography: a comparison of different motion models". *J Magn Reson Imaging*, Vol. 15, No. 6, pp. 661–671, Jun 2002.

[Mank 03] D. Manke, K. Nehrke, and P. Börnert. "Novel prospective respiratory motion correction approach for free-breathing coronary MR angiography using a patient-adapted affine motion model". *Magn Reson Med*, Vol. 50, No. 1, pp. 122–131, Jul 2003.

[Mann 07] W. J. Manning, R. Nezafat, E. Appelbaum, P. G. Danias, T. H. Hauser, and S. B. Yeon. "Coronary magnetic resonance imaging". *Magn Reson Imaging Clin N Am*, Vol. 15, No. 4, pp. 609–37, vii, Nov 2007.

[Mans 73] P. Mansfield and P. K. Grannell. "NMR 'diffraction' in solids?". *Journal of Physics C: solid state physics*, Vol. 6, No. 22, p. L422, Nov 1973.

[Math 74] A. Mathai and T. A. Davis. "Constructing the sunflower head". *Mathematical Biosciences*, Vol. 20, No. 1, pp. 117–133, Jun 1974.

[McCo 97] M. V. McConnell, V. C. Khasgiwala, B. J. Savord, M. H. Chen, M. L. Chuang, R. R. Edelman, and W. J. Manning. "Comparison of respiratory suppression methods and navigator locations for MR coronary angiography". *AJR Am J Roentgenol*, Vol. 168, No. 5, pp. 1369–1375, May 1997.

[McLe 02] K. McLeish, D. L. G. Hill, D. Atkinson, J. M. Blackall, and R. Razavi. "A study of the motion and deformation of the heart due to respiration". *IEEE Transactions on Medical Imaging*, Vol. 21, No. 9, pp. 1142–1150, Sep 2002.

[Medi 03] L. S. Medina and D. Zurakowski. "Measurement variability and confidence intervals in medicine: why should radiologists care?". *Radiology*, Vol. 226, No. 2, pp. 297–301, Feb 2003.

[Mist 06] C. A. Mistretta, O. Wieben, J. Velikina, W. Block, J. Perry, Y. Wu, K. Johnson, and Y. Wu. "Highly constrained backprojection for time-resolved MRI". *Magn Reson Med*, Vol. 55, No. 1, pp. 30–40, Jan 2006.

[Mogh 12] M. H. Moghari, P. Hu, K. V. Kissinger, B. Goddu, L. Goepfert, L. Ngo, W. J. Manning, and R. Nezafat. "Subject-specific estimation of respiratory navigator tracking factor for free-breathing cardiovascular MR". *Magn Reson Med*, Vol. 67, No. 6, pp. 1665–1672, Jun 2012.

[Monn 13] P. Monney, D. Piccini, G. Vincenti, A. Littmann, M. O. Zenge, S. C. Koestner, M. Stuber, and J. Schwitter. "Self-navigated free-breathing isotropic 3D whole heart MRI for the characterization of complex cardiac anatomy in patients with congenital heart malformations". *Journal of Cardiovascular Magnetic Resonance*, Vol. 15, No. Suppl 1, p. P12, Jan 2013.

[Naga 11] M. Nagata, S. Kato, K. Kitagawa, N. Ishida, H. Nakajima, S. Nakamori, M. Ishida, M. Miyahara, M. Ito, and H. Sakuma. "Diagnostic accuracy of 1.5-T unenhanced whole-heart coronary MR angiography performed with 32-channel cardiac coils: initial single-center experience". *Radiology*, Vol. 259, No. 2, pp. 384–392, May 2011.

[Nehr 01] K. Nehrke, P. Börnert, D. Manke, and J. C. Böck. "Free-breathing cardiac MR imaging: study of implications of respiratory motion–initial results". *Radiology*, Vol. 220, No. 3, pp. 810–815, Sep 2001.

[Neza 09] R. Nezafat, R. Ouwerkerk, A. J. Derbyshire, M. Stuber, and E. R. McVeigh. "Spectrally selective B1-insensitive T2 magnetization preparation sequence". *Magn Reson Med*, Vol. 61, No. 6, pp. 1326–1335, Jun 2009.

[Nguy 09] T. D. Nguyen, P. Spincemaille, M. D. Cham, J. W. Weinsaft, M. R. Prince, and Y. Wang. "Free-breathing 3-dimensional steady-state free precession coronary magnetic resonance angiography: comparison of four navigator gating techniques". *Magn Reson Imaging*, Vol. 27, No. 6, pp. 807–814, Jul 2009.

[Niel 04] S. Nielles-Vallespin. *Development and optimisation of radial techniques for sodium magnetic resonance imaging.* PhD thesis, Ruperto-Carola University of Heidelberg, Germany, Dec 2004.

[Niel 06] S. Nielles-Vallespin, P. Speier, X. Bi, D. Li, and E. Mueller. "Navigator-gated whole-heart coronarry MRI: comparison of 3D TrueFisp Cartesian and radial acquisitions". In: *Proceedings of the 14th Annual Meeting of ISMRM*, p. 366, Seattle, Washington, USA, May 2006.

[Niel 07] S. Nielles-Vallespin, M.-A. Weber, M. Bock, A. Bongers, P. Speier, S. E. Combs, J. Wöhrle, F. Lehmann-Horn, M. Essig, and L. R. Schad. "3D radial projection technique with ultrashort echo times for sodium MRI: clinical applications in human brain and skeletal muscle". *Magn Reson Med*, Vol. 57, No. 1, pp. 74–81, Jan 2007.

[Oppe 86] A. Oppelt. "FISP-a new fast MRI sequence". *Electromedica*, Vol. 54, pp. 15–18, 1986.

[Osul 85] J. O'sullivan. "A fast sinc function gridding algorithm for Fourier inversion in computer tomography". *IEEE Transactions on Medical Imaging*, Vol. 4, No. 4, pp. 200–207, Dec 1985.

[Paul 87] S. Paulin, G. K. von Schulthess, E. Fossel, and H. P. Krayenbuehl. "MR imaging of the aortic root and proximal coronary arteries". *AJR Am J Roentgenol*, Vol. 148, No. 4, pp. 665–670, Apr 1987.

[Picc 11] D. Piccini, A. Littmann, S. Nielles-Vallespin, and M. O. Zenge. "Spiral phyllotaxis: the natural way to construct a 3D radial trajectory in MRI". *Magn Reson Med*, Vol. 66, No. 4, pp. 1049–1056, Oct 2011.

[Picc 12] D. Piccini, A. Littmann, S. Nielles-Vallespin, and M. O. Zenge. "Respiratory self-navigation for whole-heart bright-blood coronary MRI: methods for robust isolation and automatic segmentation of the blood pool". *Magn Reson Med*, Vol. 68, No. 2, pp. 571–579, Aug 2012.

[Picc 13a] D. Piccini, G. Bonanno, G. Ginami, A. Littmann, M. O. Zenge, and M. Stuber. "Optimized respiratory reference position for 3D self-navigated whole heart coronary MRA". In: *Proceedings of the 21th Annual Meeting of ISMRM*, p. 1316, Salt Lake City, Utah, USA, Apr 2013.

[Picc 13b] D. Piccini, T. Rutz, S. Coppo, G. Ginami, S. J., and M. Stuber. "Self-Navigated 3D whole heart imaging for combined coronary MRA and delayed hyperenhancement imaging". In: *Proceedings of the 25th Annual Meeting of Angio Club*, New York City, New York, USA, Aug 2013.

[Picc 14] D. Piccini, P. Monney, C. Sierro, S. Coppo, G. Bonanno, R. B. van Heeswijk, J. Chaptinel, G. Vincenti, J. de Blois, S. C. Koestner, T. Rutz, A. Littmann, M. O. Zenge, J. Schwitter, and M. Stuber. "Respiratory Self-navigated Postcontrast Whole-Heart Coronary MR Angiography: Initial Experience in Patients". *Radiology*, Vol. 270, No. 2, pp. 378–386, Feb 2014.

[Pipe 99] J. G. Pipe and P. Menon. "Sampling density compensation in MRI: rationale and an iterative numerical solution". *Magn Reson Med*, Vol. 41, No. 1, pp. 179–186, Jan 1999.

[Prue 01] K. P. Pruessmann, M. Weiger, P. Börnert, and P. Boesiger. "Advances in sensitivity encoding with arbitrary k-space trajectories". *Magn Reson Med*, Vol. 46, No. 4, pp. 638–651, Oct 2001.

[Purc 46] E. Purcell. "Spontaneous emission probabilities at radio frequencies". *Phys. Rev.*, Vol. 69, p. 681, Jun 1946.

[Rasc 99] V. Rasche, R. Proksa, R. Sinkus, P. Börnert, and H. Eggers. "Resampling of data between arbitrary grids using convolution interpolation". *IEEE Transactions on Medical Imaging*, Vol. 18, No. 5, pp. 385–392, May 1999.

[Reyk 04] A. Reykowski and M. Blasche. "Mode matrix: a generalized signal combiner for parallel imaging arrays". In: *Proceedings of the 12th Annual Meeting of ISMRM*, p. 1587, Kyoto, Japan, May 2004.

[Rldl 82] J. Rldley. "Computer simulation of contact pressure in capitula". *Journal of theoretical biology*, Vol. 95, No. 1, pp. 1–11, Mar 1982.

[Roge 11] V. L. Roger, A. S. Go, D. M. Lloyd-Jones, R. J. Adams, J. D. Berry, T. M. Brown, M. R. Carnethon, S. Dai, G. de Simone, E. S. Ford, C. S. Fox, H. J. Fullerton, C. Gillespie, K. J. Greenlund, S. M. Hailpern, J. A. Heit, P. M. Ho, V. J. Howard, B. M. Kissela, S. J. Kittner, D. T. Lackland, J. H. Lichtman, L. D. Lisabeth, D. M. Makuc, G. M. Marcus, A. Marelli, D. B. Matchar, M. M. McDermott, J. B. Meigs, C. S. Moy, D. Mozaffarian, M. E. Mussolino, G. Nichol, N. P. Paynter, W. D. Rosamond, P. D. Sorlie, R. S. Stafford, T. N. Turan, M. B. Turner, N. D. Wong, J. Wylie-Rosett, A. H. A. S. C. , and S. S. Subcommittee. "Heart disease and stroke statistics–2011 update: a report from the American Heart Association". *Circulation*, Vol. 123, No. 4, pp. e18–e209, Feb 2011.

[Rohk 10] C. Rohkohl, G. Lauritsch, L. Biller, M. Prümmer, J. Boese, and J. Hornegger. "Interventional 4D motion estimation and reconstruction of cardiac vasculature without motion periodicity assumption". *Med. Image Anal.*, Vol. 14, No. 5, pp. 687–694, Oct 2010.

[Rose 84] B. R. Rosen, V. J. Wedeen, and T. J. Brady. "Selective saturation NMR imaging". *J Comput Assist Tomogr*, Vol. 8, No. 5, pp. 813–818, Oct 1984.

[Saff 97] E. B. Saff and A. B. Kuijlaars. "Distributing many points on a sphere". *The Mathematical Intelligencer*, Vol. 19, No. 1, pp. 5–11, 1997.

[Saku 05] H. Sakuma, Y. Ichikawa, N. Suzawa, T. Hirano, K. Makino, N. Koyama, M. Van Cauteren, and K. Takeda. "Assessment of coronary arteries with total study time of less than 30 minutes by using whole-heart coronary MR angiography". *Radiology*, Vol. 237, No. 1, pp. 316–321, Oct 2005.

[Saku 06] H. Sakuma, Y. Ichikawa, S. Chino, T. Hirano, K. Makino, and K. Takeda. "Detection of coronary artery stenosis with whole-heart coronary magnetic resonance angiography". *J Am Coll Cardiol*, Vol. 48, No. 10, pp. 1946–1950, Nov 2006.

[Saku 11] H. Sakuma. "Coronary CT versus MR angiography: the role of MR angiography". *Radiology*, Vol. 258, No. 2, pp. 340–349, Feb 2011.

[Scan 99] P. J. Scanlon, D. P. Faxon, A. M. Audet, B. Carabello, G. J. Dehmer, K. A. Eagle, R. D. Legako, D. F. Leon, J. A. Murray, S. E. Nissen, C. J. Pepine, R. M. Watson, J. L. Ritchie, R. J. Gibbons, M. D. Cheitlin, T. J. Gardner, A. Garson, Jr, R. Russell, Jr, T. J. Ryan, and S. Smith, Jr. "ACC/AHA guidelines for coronary angiography: executive summary and recommendations. A report of the American College of Cardiology/American Heart Association Task Force on Practice Guidelines (Committee on Coronary Angiography) developed in collaboration with the Society for Cardiac Angiography and Interventions". *Circulation*, Vol. 99, No. 17, pp. 2345–2357, May 1999.

[Sche 10] H. Scheffel, P. Stolzmann, H. Alkadhi, N. Azemaj, A. Plass, S. Baumueller, L. Desbiolles, S. Leschka, S. Kozerke, V. Falk, P. Boesiger, C. Wyss, B. Marincek, and O. F. Donati. "Low-dose CT and cardiac MR for the diagnosis of coronary artery disease: accuracy of single and combined approaches". *Int J Cardiovasc Imaging*, Vol. 26, No. 5, pp. 579–590, Jun 2010.

[Scho 95] H. Schomberg and J. Timmer. "The gridding method for image reconstruction by Fourier transformation". *IEEE Transactions on Medical Imaging*, Vol. 14, No. 3, pp. 596–607, Sep 1995.

[Seib 07] N. Seiberlich, F. A. Breuer, M. Blaimer, K. Barkauskas, P. M. Jakob, and M. A. Griswold. "Non-Cartesian data reconstruction using GRAPPA operator gridding (GROG)". *Magn Reson Med*, Vol. 58, No. 6, pp. 1257–1265, Dec 2007.

[Shah 09] S. Shah, P. Kellmann, A. Greiser, P. J. Weale, S. Zuehlsdorff, and R. Jerecic. "Rapid fiefield estimation for cardiac shimming". In: *Proceedings of the 17th Annual Meeting of ISMRM*, p. 566, Honolulu, Hawaii, USA, May 2009.

[Shec 04a] G. Shechter. *Respiratory motion of the heart: implications for magnetic resonance coronary angiography*. PhD thesis, Johns Hopkins University, Baltimore, Mariland, USA, 2004.

[Shec 04b] G. Shechter, C. Ozturk, J. R. Resar, and E. R. McVeigh. "Respiratory motion of the heart from free breathing coronary angiograms". *IEEE Transactions on Medical Imaging*, Vol. 23, No. 8, pp. 1046–1056, Aug 2004.

[Shep 74] L. A. Shepp and B. F. Logan. "The Fourier reconstruction of a head section". *IEEE Transactions on Nuclear Science*, Vol. 21, No. 3, pp. 21–43, Jun 1974.

[Shu 06] Y. Shu, S. J. Riederer, and M. A. Bernstein. "Three-dimensional MRI with an undersampled spherical shells trajectory". *Magn Reson Med*, Vol. 56, No. 3, pp. 553–562, Sep 2006.

[Spue 02] E. Spuentrup, W. J. Manning, R. M. Botnar, K. V. Kissinger, and M. Stuber. "Impact of navigator timing on free-breathing submillimeter 3D coronary magnetic resonance angiography". *Magn Reson Med*, Vol. 47, No. 1, pp. 196–201, Jan 2002.

[Steh 04] C. Stehning, P. Börnert, K. Nehrke, H. Eggers, and O. Dössel. "Fast isotropic volumetric coronary MR angiography using free-breathing 3D radial balanced FFE acquisition". *Magn Reson Med*, Vol. 52, No. 1, pp. 197–203, Jul 2004.

[Steh 05a] C. Stehning. *Motion correction and volumetric acquisition techniques for coronary magnetic resonance acorrection*. PhD thesis, University Friedriciana Karlsruhe, Germany, Jul 2005.

[Steh 05b] C. Stehning, P. Börnert, K. Nehrke, H. Eggers, and M. Stuber. "Free-breathing whole-heart coronary MRA with 3D radial SSFP and self-navigated image reconstruction". *Magn Reson Med*, Vol. 54, No. 2, pp. 476–480, Aug 2005.

[Stei 08] P. D. Stein, A. Y. Yaekoub, F. Matta, and H. D. Sostman. "64-slice CT for diagnosis of coronary artery disease: a systematic review". *Am. J. Med.*, Vol. 121, No. 8, pp. 715–725, Aug 2008.

[Stro 09] N. Strobel, O. Meissner, J. Boese, T. Brunner, B. Heigl, M. Hoheisel, G. Lauritsch, M. Nagel, M. Pfister, E.-P. Rührnschopf, B. Scholz, B. Schreiber, M. Spahn, M. Zellerhoff, and K. Klingenbeck-Regn. "3D imaging with flat-detector C-arm systems". In: *Multislice CT*, pp. 33–51, Springer Berlin Heidelberg, 2009.

[Stub 01] M. Stuber, R. M. Botnar, K. V. Kissinger, and W. J. Manning. "Free-breathing black-blood coronary MR angiography: initial results". *Radiology*, Vol. 219, No. 1, pp. 278–283, Apr 2001.

[Stub 07] M. Stuber and R. G. Weiss. "Coronary magnetic resonance angiography". *J Magn Reson Imaging*, Vol. 26, No. 2, pp. 219–234, Aug 2007.

[Stub 99a] M. Stuber, R. M. Botnar, P. G. Danias, K. V. Kissinger, and W. J. Manning. "Submillimeter three-dimensional coronary MR angiography with real-time navigator correction: comparison of navigator locations". *Radiology*, Vol. 212, No. 2, pp. 579–587, Aug 1999.

[Stub 99b] M. Stuber, R. M. Botnar, P. G. Danias, D. K. Sodickson, K. V. Kissinger, M. Van Cauteren, J. De Becker, and W. J. Manning. "Double-oblique free-breathing high resolution three-dimensional coronary magnetic resonance angiography". *J Am Coll Cardiol*, Vol. 34, No. 2, pp. 524–531, Aug 1999.

[Tang 11] T. Tangcharoen, A. Bell, S. Hegde, T. Hussain, P. Beerbaum, T. Schaeffter, R. Razavi, R. M. Botnar, and G. F. Greil. "Detection of coronary artery anomalies in infants and young children with congenital heart disease by using MR imaging". *Radiology*, Vol. 259, No. 1, pp. 240–247, Apr 2011.

[Tayl 99] A. M. Taylor, P. Jhooti, D. N. Firmin, and D. J. Pennell. "Automated monitoring of diaphragm end-expiratory position for real-time navigator echo MR coronary angiography". *J Magn Reson Imaging*, Vol. 9, No. 3, pp. 395–401, Mar 1999.

[Tell 03] R. Tello and P. E. Crewson. "Hypothesis testing II: means". *Radiology*, Vol. 227, No. 1, pp. 1–4, Apr 2003.

[Voge 79] H. Vogel. "A better way to construct the sunflower head". *Mathematical biosciences*, Vol. 44, No. 3, pp. 179–189, Jun 1979.

[Wang 95] Y. Wang, S. J. Riederer, and R. L. Ehman. "Respiratory motion of the heart: kinematics and the implications for the spatial resolution in coronary imaging". *Magn Reson Med*, Vol. 33, No. 5, pp. 713–719, May 1995.

[Wang 99] Y. Wang, E. Vidan, and G. W. Bergman. "Cardiac motion of coronary arteries: variability in the rest period and implications for coronary MR angiography". *Radiology*, Vol. 213, No. 3, pp. 751–758, Dec 1999.

[Wieb 01] O. Wieben, A. V. Barger, W. F. Block, and C. A. Mistretta. "Correcting for translational motion in 3D projection reconstruction". In: *Proceedings of the 9th Annual Meeting of ISMRM*, p. 737, Glasgow, Scotland, May 2001.

[Wink 07] S. Winkelmann, T. Schaeffter, T. Koehler, H. Eggers, and O. Doessel. "An optimal radial profile order based on the Golden Ratio for time-resolved MRI". *IEEE Transactions on Medical Imaging*, Vol. 26, No. 1, pp. 68–76, Jan 2007.

[Wong 94] S. T. Wong and M. S. Roos. "A strategy for sampling on a sphere applied to 3D selective RF pulse design". *Magn Reson Med*, Vol. 32, No. 6, pp. 778–784, Dec 1994.

[Wood 85] M. L. Wood and R. M. Henkelman. "MR image artifacts from periodic motion". *Medical physics*, Vol. 12, No. 2, p. 143, Mar 1985.

[Wrig 91] G. A. Wright, D. G. Nishimura, and A. Macovski. "Flow-independent magnetic resonance projection angiography". *Magn Reson Med*, Vol. 17, No. 1, pp. 126–140, Jan 1991.

[Xian 93] Q. S. Xiang and R. M. Henkelman. "K-space description for MR imaging of dynamic objects". *Magn Reson Med*, Vol. 29, No. 3, pp. 422–428, Mar 1993.

[Xie 10] J. Xie, P. Lai, H. Bhat, and D. Li. "Whole-heart coronary magnetic resonance angiography at 3.0T using short-TR steady-state free precession, vastly undersampled isotropic projection reconstruction". *J Magn Reson Imaging*, Vol. 31, No. 5, pp. 1230–1235, May 2010.

[Yang 09] Q. Yang, K. Li, X. Liu, X. Bi, Z. Liu, J. An, A. Zhang, R. Jerecic, and D. Li. "Contrast-enhanced whole-heart coronary magnetic resonance angiography at 3.0-T: a comparative study with X-ray angiography in a single center". *J Am Coll Cardiol*, Vol. 54, No. 1, pp. 69–76, Jun 2009.